Identification of a novel mechanism driving NAFLD progression and therapeutic strategies

DISSERTATION

ZUR ERLANGUNG DES AKADEMISCHEN GRADES DES DOKTORS
DER NATURWISSENSCHAFTEN (DR. RER. NAT.)
FAKULTÄT FÜR CHEMIE UND CHEMISCHE BIOLOGIE DER TECHNISCHEN
UNIVERSITÄT DORTMUND

VORGELEGT VON

MAIJU KAROLIINA MYLLYS, M. SC.

GEBOREN IN LAPPEENRANTA, FINNLAND

DORTMUND 2021

1. GUTACHTER: PROF. DR. JAN G. HENGSTLER
2. GUTACHTER: PROF. DR. CARSTEN WATZL

TAG DER DISPUTATION: 16.03.2021

Eidesstattliche Versicherung (Affidavit)

____
Name, Vorname
(Surname, first name)

____
Matrikel-Nr.
(Enrolment number)

Belehrung:

Wer vorsätzlich gegen eine die Täuschung über Prüfungsleistungen betreffende Regelung einer Hochschulprüfungsordnung verstößt, handelt ordnungswidrig. Die Ordnungswidrigkeit kann mit einer Geldbuße von bis zu 50.000,00 € geahndet werden. Zuständige Verwaltungsbehörde für die Verfolgung und Ahndung von Ordnungswidrigkeiten ist der Kanzler/die Kanzlerin der Technischen Universität Dortmund. Im Falle eines mehrfachen oder sonstigen schwerwiegenden Täuschungsversuches kann der Prüfling zudem exmatrikuliert werden, § 63 Abs. 5 Hochschulgesetz NRW.

Die Abgabe einer falschen Versicherung an Eides statt ist strafbar.

Wer vorsätzlich eine falsche Versicherung an Eides statt abgibt, kann mit einer Freiheitsstrafe bis zu drei Jahren oder mit Geldstrafe bestraft werden, § 156 StGB. Die fahrlässige Abgabe einer falschen Versicherung an Eides statt kann mit einer Freiheitsstrafe bis zu einem Jahr oder Geldstrafe bestraft werden, § 161 StGB.

Die oben stehende Belehrung habe ich zur Kenntnis genommen:

Official notification:

Any person who intentionally breaches any regulation of university examination regulations relating to deception in examination performance is acting improperly. This offence can be punished with a fine of up to EUR 50,000.00. The competent administrative authority for the pursuit and prosecution of offences of this type is the chancellor of the TU Dortmund University. In the case of multiple or other serious attempts at deception, the candidate can also be unenrolled, Section 63, paragraph 5 of the Universities Act of North Rhine-Westphalia.

The submission of a false affidavit is punishable.

Any person who intentionally submits a false affidavit can be punished with a prison sentence of up to three years or a fine, Section 156 of the Criminal Code. The negligent submission of a false affidavit can be punished with a prison sentence of up to one year or a fine, Section 161 of the Criminal Code.

I have taken note of the above official notification.

____
Ort, Datum
(Place, date)

____
Unterschrift
(Signature)

Titel der Dissertation:
(Title of the thesis):

____

____

____

Ich versichere hiermit an Eides statt, dass ich die vorliegende Dissertation mit dem Titel selbstständig und ohne unzulässige fremde Hilfe angefertigt habe. Ich habe keine anderen als die angegebenen Quellen und Hilfsmittel benutzt sowie wörtliche und sinngemäße Zitate kenntlich gemacht.
Die Arbeit hat in gegenwärtiger oder in einer anderen Fassung weder der TU Dortmund noch einer anderen Hochschule im Zusammenhang mit einer staatlichen oder akademischen Prüfung vorgelegen.

I hereby swear that I have completed the present dissertation independently and without inadmissible external support. I have not used any sources or tools other than those indicated and have identified literal and analogous quotations.

The thesis in its current version or another version has not been presented to the TU Dortmund University or another university in connection with a state or academic examination.*

*Please be aware that solely the German version of the affidavit ("Eidesstattliche Versicherung") for the PhD thesis is the official and legally binding version.

____
Ort, Datum
(Place, date)

____
Unterschrift
(Signature)

TABLE OF CONTENTS

SUMMARY

Non-alcoholic fatty liver disease (NAFLD) is the most common chronic liver disease in Western countries with an increasing prevalence of approximately 25 %. NAFLD comprises several stages, starting as benign steatosis and progressing to non-alcoholic steatohepatitis (NASH), and in some cases to liver cirrhosis and hepatocellular carcinoma (HCC). Although several emerging therapies are currently in clinical trials, so far there are no approved drugs for treatment of NASH. This is mainly because the driving mechanisms behind NAFLD progression are rather poorly understood. Consequently, NAFLD represents the second most common cause for liver transplantation. The overarching goal of this thesis was to investigate the mechanisms of NAFLD stage transitions, and to establish preventive measures for the progression from benign steatosis to NASH. For this purpose, a mouse model of NAFLD progression was first established by long-term feeding of male C57Bl/6N mice with western-style diet (WD) up to 54 weeks. The disease progression was evaluated time-dependently by biochemical, histopathological, and immunohistochemical analyses as well as by intravital two-photon-based imaging. This comprehensive analyses revealed six stages in NAFLD progression: (1) benign steatosis, (2) macrophage crown-like structure formation, (3) macropinocytosis of bile, (4) ductular reaction, (5) dedifferentiation and functional shutdown, and (6) tumor nodule formation. Particularly, the novel finding of this thesis was the identification of stage 3, macropinocytosis of bile, where a retrograde vesicular uptake of bile from bile canaliculi to hepatocytes led to toxic accumulation of bile acids in the liver tissue, providing a link between NAFLD and cholestasis. The phenomenon was further identified as macropinocytosis by treating the mice with a macropinocytosis-specific inhibitor imipramine. As a result, a single application of imipramine efficiently blocked macropinocytosis in WD-fed mice. Interestingly, a long-term application of imipramine for 8 weeks decreased the bile acid concentrations in the liver tissue and led to significant NAFLD amelioration. To study whether these findings are also relevant for human NAFLD, liver biopsies from patients at different stages of NAFLD were also analysed. Interestingly, bile macropinocytosis was also relevant in the NAFLD patients as detected by the presence of fragments of bile canaliculi within steatotic hepatocytes. In conclusion, an NAFLD mouse model recapitulating the different stages of human NAFLD progression to NASH and eventually to HCC was successfully established. Moreover, a novel mechanism possibly driving NALFD progression was identified as macropinocytosis of bile from bile canaliculi back to hepatocytes. Inhibition of macropinocytosis may represent an attractive therapeutic target to prevent NAFLD progression in human patients.

ZUSAMMENFASSUNG

Die nicht-alkoholische Fettlebererkrankung (NAFLD) ist die häufigste chronische Lebererkrankung in den westlichen Ländern mit einer steigenden Prävalenz von etwa 25 %. NAFLD umfasst mehrere Stadien, beginnend als gutartige Steatose, die im weiteren Verlauf zur nicht-alkoholischen Steatohepatitis (NASH) fortschreitet. In einigen Fällen kann es sich zur Leberzirrhose und zum hepatozellulären Karzinom (HCC) weiterentwickeln. Obwohl sich mehrere neue Therapien derzeit in der klinischen Erprobung befinden, gibt es bisher keine zugelassenen Medikamente zur Behandlung von NASH. Einer der Gründe, warum es noch keine effektive Behandlung gibt, liegt an dem mangelnden Verständnis der treibenden Mechanismen hinter der NAFLD-Progression. Infolgedessen stellt die NAFLD die zweithäufigste Ursache für eine Lebertransplantation dar. Für ein besseres Verständnis von NAFLD war das übergeordnete Ziel dieser Arbeit die Mechanismen der NAFLD-Stadienübergänge zu untersuchen und präventive Maßnahmen für die Progression von der benignen Steatose zu NASH zu etablieren. Dazu wurde zunächst ein Mausmodell der NAFLD-Progression durch Langzeitfütterung von männlichen C57Bl/6N-Mäusen mit westlicher Ernährung (WD) bis zu 54 Wochen etabliert. Die Krankheitsprogression wurde zeitabhängig durch biochemische, histopathologische und immunhistochemische Analysen, sowie durch intravitale Zwei-Photonen-basierte Bildgebung evaluiert. Diese umfassenden Analysen ergaben sechs Stadien der NAFLD-Progression: (1) benigne Steatose, (2) Makrophagenkronen-ähnliche Strukturbildung, (3) Makropinozytose der Galle, (4) duktuläre Reaktion, (5) Dedifferenzierung und Funktionsstillstand und (6) Tumorknotenbildung. Die neuartige Erkenntnis dieser Arbeit war insbesondere die Identifizierung des Stadiums 3, der Makropinozytose der Galle. Bei diesem Stadium führt eine retrograde, vesikuläre Aufnahme von Galle aus den Gallenkanälchen in die Hepatozyten zu einer toxischen Akkumulation von Gallensäure im Lebergewebe, was eine Verbindung zwischen NAFLD und Cholestase darstellt. Das Phänomen wurde weiter als Makropinozytose identifiziert, indem die Mäuse mit einem Makropinozytose-spezifischen Inhibitor Imipramin behandelt wurden. Nach einer einmaligen Anwendung von Imipramin konnte die Makropinozytose in WD-gefütterten Mäusen effizient blockiert werden. Interessanterweise verringerte eine Langzeitapplikation von Imipramin über 8 Wochen die Gallensäurekonzentrationen im Lebergewebe und führte zu einer signifikanten Besserung der NAFLD. Zur Überprüfung der Relevanz dieser Ergebnisse für NAFLD Patienten, wurden auch Leberbiopsien von Patienten in verschiedenen Stadien der NAFLD analysiert. Auch bei den NAFLD-Patienten war die Makropinozytose der Galle relevant, was durch das Vorhandensein von Fragmenten der Gallenkanälchen innerhalb der steatotischen

Hepatozyten nachgewiesen werden konnte. Zusammenfassend lässt sich sagen, dass ein NAFLD-Mausmodell, das die verschiedenen Stadien der menschlichen NAFLD-Progression zu NASH und schließlich zu HCC rekapituliert, erfolgreich etabliert wurde. Darüber hinaus wurde ein neuer Mechanismus identifiziert, der möglicherweise die Progression der NALFD vorantreibt: die Makropinozytose von Galle aus den Gallenkanälchen zurück in die Hepatozyten. Somit könnte die Hemmung der Makropinozytose ein attraktives therapeutisches Ziel darstellen, um die Progression der NAFLD bei Patienten zu verhindern.

ABBREVIATIONS

%	Percent
°C	Celsius degree
Ab	Antibody
Abcb	ATP Binding Cassette Subfamily B
Abcc	ATP Binding Cassette Subfamily C
Acyl-CoA	Acyl-coenzyme A
ALT	Alanine transaminase
ALP	Alkaline phosphatase
AST	Aspartate transaminase
ATP	Adenosine triphosphate
BSA	Bovine Albumin Fraction V
BSEP	Bile Salt Export Pump
CA	Cholic acid
Ca	Calcium
CC1	Cell conditioning 1
CDCA	Chenodeoxycholic acid
CK	Cytokeratin
CLF	Cholyl-L-lysyl-fluorescein
Ct	Ct value
CV	Central vein
Cyp2e1	Cytochrome P450 enzyme 2e1
Cyp7a1	Cytochrome P450 enzyme cholesterol 7α-hydroxylase
Cyp7b1	Cytochrome P450 7b1
Cyp8b1	Cytochrome P450 enzyme 8B1
Cyp27A1	Cytochrome P450 family 27 subfamily A member 1
DAB	3,3’-Diaminobenzidine
DAPI	4′,6-diamidino-2-phenylindole
dd	Double-distilled
DEPC	Diethylpyrocarbonate
DNA	Deoxyribonucleic acid
ECL	Enhanced chemiluminescence
ECM	Extracellular matrix

EDTA	Ethylenediaminetetraacetic acid
EtOH	Ethanol
FA	Fatty acid
FFPE	formalin-fixed, paraffin embedded
FGF15/19	Fibroblast growth factor 15/19
FXR	Farnesoid X receptor
g	Standard gravity
g	Gram
GAPDH	Glyceraldehyde 3-phosphate dehydrogenase
GDH	Glutamate dehydrogenase
h	Hour(s)
H&E	Hematoxylin and eosin
H_2O	Water
H_2O_2	Hydrogen peroxide
HCC	Hepatocellular carcinoma
HCl	Hydrochloric acid
HGF	Hepatocyte growth factor
HMGB1	High mobility group box 1
HPC	Hepatic progenitor cell
HRP	Horseradish peroxidase
HSC	Hepatic stellate cell
HSP	Heat shock protein
IC	Inhibitory concentration
IF	Immunofluorescence
IHC	Immunohistochemistry
IL	Interleukin
KC	Kupffer cell
kcal	kilocalorie
KCl	Potassium Chloride
kg	Kilogram
KH_2PO_4	Potassium dihydrogen phosphate
l	Liter
LC-ESI-MS/MS	liquid chromatography–negative electrospray ionization–tandem mass spectrometry

LCS	Liquid coverslip
LD	Lipid droplet
LDH	Lactate dehydrogenase
loxP	Locus of X-over P1
LSEC	Liver sinusoidal endothelial cell
LSM	Laser Scanning Microscope
mA	Milliamper
MALDI-MSI	Matrix-assisted laser desorption/ionization mass spectrometric imaging
mg	Milligram
min	Minute(s)
ml	Milliliter
MLKL	Mixed lineage kinase domain like pseudokinase
mm	Millimeter
MMP	Matrix metalloproteinase
mRNA	Messenger RNA
MRP	Multidrug resistance-associated protein
Na^+	Sodium cation
NAFLD	Non-alcoholic fatty liver disease
NaOH	Sodium hydroxide
NASH	Non-alcoholic steatohepatitis
NF-κB	Nuclear factor-kappa B
ng	Nanogram
NK	Natural killer
nor-UDCA	Nor-Ursodeoxycholic acid
NPC	Non parenchymal cell
NTCP	Na+-taurocholate co-transporting polypeptide
OATP	Organic anion-transporter
OCA	Obeticholic acid
OST	Organic solute transporter
PAGE	Polyacrylamide gel electrophoresis
PBS	Phosphate-buffered saline solution
PBS-T	Phosphate-buffered saline solution with Tween20
PC	Pericentral

PCR	Polymerase chain reaction
PFA	Paraformaldehyde
PP	Periportal
PPAR	Peroxisome proliferator-activated receptor
PV	Portal vein
PVDF	Polyvinylidene fluoride
qRT-PCR	Quantitative real time PCR
RIP	receptor-interacting protein
RNA	Ribonucleic acid
RUO	Research use only
RXR	Retinoid X receptor
SD	Standard diet
SDS	Sodium dodecyl sulfate
SE	Standard error
SHP	Small heterodimeric partner
Slc10a1	Solute carrier family 10 member 1
Slco1b2	Solute carrier organic anion transporter family member 1b2
SSC	Saline-sodium citrate
TBS	Tris-buffered saline
TBS-T	Tris-buffered saline with Tween20
TCA	Taurocholic acid
td	Tandem trimer
TdT	Terminal Deoxynucleotidyl Transferase
TG	Triglyceride
TGF-β	Transforming growth factor beta
TLR	Toll-like receptor
TMRE	Tetramethylrhodamine ethyl ester
TNF-α	Tumor necrosis factor α
Tris	Tris(hydroxymethyl)aminomethane
TUNEL	Terminal deoxynucleotidyl transferase dUTP nick end labeling
VLDL	Very low-density lipoprotein
WB	Western blotting
WD	Western diet
Wnt2	Wnt Family Member 2

x	Fold
α-SMA	Alpha-smooth muscle actin
μg	Microgram
μl	Microliter
μM	Micromolar
μm	Micrometer

LIST OF FIGURES

LIST OF TABLES

1 INTRODUCTION

The liver is the largest internal organ of the body responsible for several complex vital functions including metabolism, protein synthesis, bile formation and excretion as well as detoxification of xenobiotics.

1.1 Liver structure

The human liver is located in the upper right-hand side of the abdominal cavity, below to the diaphragm. It forms approximately 2 % of the total bodyweight (Kalra & Tuma, 2018). Grossly, the liver is divided into two main lobes; the left and the right lobe. The right lobe is further subdivided at the visceral surface into two segments; the caudate and the quadrate lobes. The liver has a unique dual blood supply: approximately 75 % of the blood flow is nutrient-rich, oxygen-poor blood derived from the gastrointestinal tract, spleen, and pancreas via portal vein. The remaining 25 % is nutrient-poor, oxygen rich blood delivered to the liver via hepatic artery. Both the hepatic portal vein and the hepatic artery enter the liver at its visceral surface through the hilus. In the opposite direction to the blood, bile leaves the liver and reaches the intestine via the extrahepatic bile duct (Fig. 1.1) (Kalra & Tuma, 2018; Vernon & Kasi, 2019). In mice, anatomy of the liver is different in comparison to the liver of human. The main features are listed in Table 1.1.

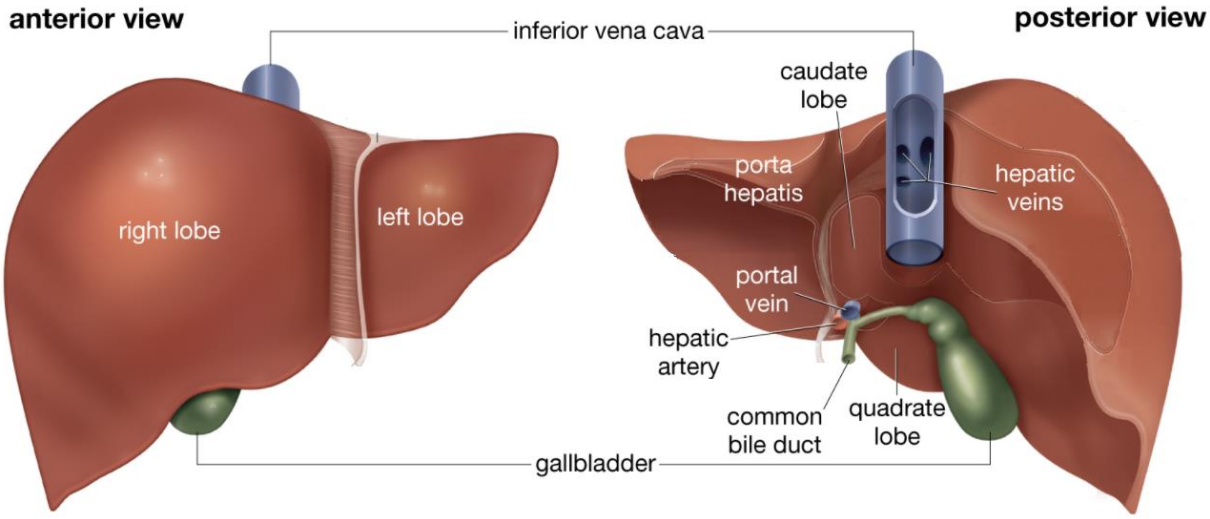

Figure 1.1. Anatomy of human liver. Figure modified from www.britannica.com/science/liver.

Table 1.1. Comparison of the gross anatomy of human and mouse livers. Table adapted from Brackhagen, 2020.

Feature	Human liver	Mouse liver
Location	Upper right quadrant of the abdominal cavity	Fills the entire cranial part of the abdominal cavity
Liver/bodyweight ratio	2 %	5 %
Gallbladder	Under the right lobe	Protruding from between the two segments of median lobe
Main lobes	Right and left	Median, right, left, caudate and quadrate
Largest lobe	Right	Left
Ligaments	Prominent	Not prominent

From the histological point of view, the liver of both humans and mice is formed of repetitive functional units called lobules. The classical lobules are hexagonally-shaped, having so called portal triads consisting of a bile duct, a hepatic artery, and a portal vein at the periphery of the lobule. In the center of the lobule is a central vein, and parenchymal liver cells, hepatocytes, are radially arranged as cords from the portal triad towards the central vein (Fig. 1.2). Between the plates of hepatocytes, small blood vessels called liver sinusoids are carrying blood from portal vein and hepatic artery towards the central vein. In contrast, the bile flows to the opposite direction towards the portal triad (Kalra & Tuma, 2018). The blood flow from the portal triad to the central vein creates a spatial separation of variety of metabolic pathways in hepatocytes, i.e. liver zonation. According to this separation, hepatic lobule can be divided into three distinct zones: periportal (zone 1), midzonal (zone 2), and pericentral zone (zone 3), where the zonated hepatocytes express their characteristic enzymes and conducting separate metabolic actions (Katz et al., 1977; Rappaport et al., 1954; Vernon & Kasi, 2019).

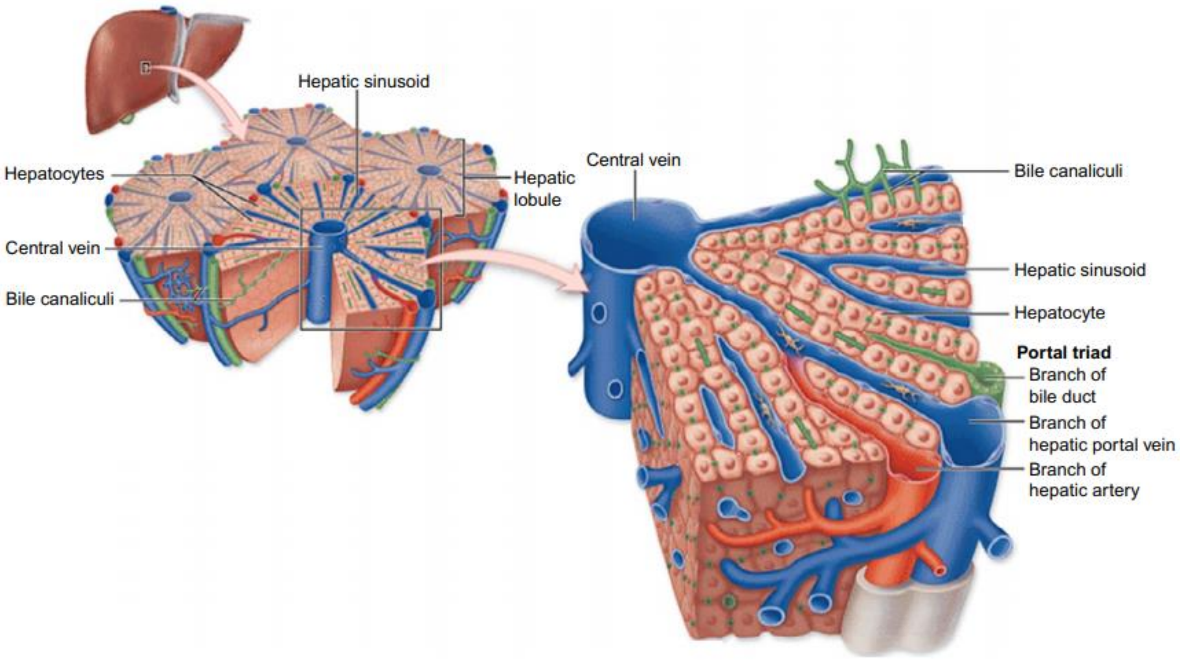

Figure 1.2. Structure of liver lobules. The liver consists of lobules where blood flows from portal triad towards the central vein in sinusoids, In contrast, bile flux occurs to the opposite direction and leaves the lobule at the portal triad where it drains into bile ducts. Hepatocytes are arranged as cords radiating towards the portal vein. Figure modified from Ortega-Ribera et al., 2018.

1.1.1 Liver cell types

The liver lobule contains both parenchymal and non-parenchymal cell types. The parenchymal cells, hepatocytes, comprise up to 80 % of all the liver mass. The remaining 20 % of the liver mass is composed of the non-parenchymal cells (NPCs), a heterogeneous group of liver sinusoidal endothelial cells (LSECs), hepatic stellate cells (HSCs), Kupffer cells (KCs), cholangiocytes, hepatic progenitor cells, and lymphocytes, all performing their specific tasks in the liver (Fig. 1.2) (Gordillo et al., 2015; Malik et al., 2002).

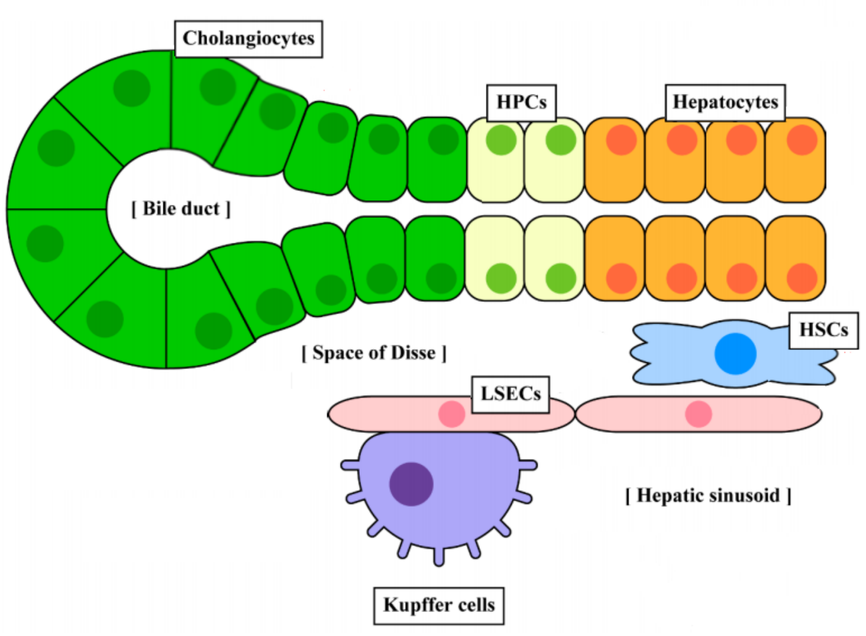

Figure 1.3. Liver cell types. The main liver cell types are hepatocytes, liver sinusoidal endothelial cells (LSECs), hepatic stellate cells (HSCs), Kupffer cell, hepatic progenitor cells (HPCs) and cholangiocytes Figure modified from Sato et al., 2019.

1.1.1.1 Hepatocytes

The main type of the liver cells, hepatocytes, are polarized epithelial cells with basolateral and apical domains. The basolateral membrane faces towards the liver sinusoids, participating in the substance exchange between the hepatocytes and blood. On the apical membrane, adjacent hepatocytes line the bile canaliculi to participate in the bile excretion (Gordillo et al., 2015; Treyer & Müsch, 2013). Moreover, hepatocytes perform heterogeneous tasks depending on their location in the lobule zones, such as gluconeogenesis in the periportal hepatocytes and glycolysis in the pericentral area (Katz et al., 1977).

1.1.1.2 Non-parenchymal cells (NPCs)

First of the NPC populations, *liver sinusoidal endothelial cells (LSECs)*, are fenestrated sieve-plate forming cells. They line the hepatic sinusoids, forming a barrier between blood and hepatocytes, and participate in exchange of nutrients, excretion of waste products and regulation of plasma lipoprotein concentration (Potter, 2019). Moreover, they have a role in hepatic immunity by acting as antigen-representing cells (Ebrahimkhani et al., 2011) and secreting cytokines (Neumann et al., 2015).

In the space of Disse between the LSECs and hepatocytes is located another NPC population, *hepatic stellate cells (HSCs).* In their quiescent state, HSCs are vitamin A-storing cells. Nevertheless, an activation by cytokines or chemokines leads to their trans-differentiation into myofibroblasts that start to produce of laminin and different types of collagen, contributing to a fibrosis progression after chronic liver injury (Potter, 2019).

A population of various granular sinusoidal cells, *liver-specific lymphocytes or pit cells*. They are considered as a subpopulation of natural killer (NK) cells. They contribute to the innate immune system against pathogens by possessing cytotoxicity against tumor cells (Parker & Picut, 2012; Potter, 2019). Importantly, the pit cells are working in synergy with other liver NPC type, *Kupffer cells (KCs)*. KCs are a resident macrophage population located inside the hepatic sinusoids. They are the major phagocytic cell type in the liver and known to respond to endogenous substances and foreign material, by detoxifying and removing them (Cattley & Popp, 2002). In addition, KCs act in primary immune response against toxic materials. After their activation, KCs begin to produce numerous proinflammatory cytokines and chemokines such as TNFα, IL-6, and CCL2, promoting activation of an acute phase reaction and recruiting other cell types (Petrasek et al., 2013; Schwabe et al., 2014). Moreover, KCs stimulate fibrogenesis by production of matrix metalloproteinases, reactive oxygen species, transforming growth factor beta 1 (TGF-β1), and platelet-derived growth factor. During liver regeneration, KCs start to produce anti-inflammatory cytokine, e.g. interleukin-10, and downregulate the proinflammatory cytokine production, leading to inflammation resolution (Petrasek et al., 2013). The KCs are distributed along the liver lobule, nevertheless, the highest number is found in the periportal and midzonal compartment of the liver lobule (Bouwens et al., 1986).

Another NPC population, *cholangiocytes*, is a group of polar epithelial cells with basolateral and luminal domains, forming the bile-draining bile ducts. Cholangiocytes have an important role in bile formation and secretion as well as in reabsorption of secondary solutes from bile (Potter, 2019). Moreover, cholangiocytes act as immune response regulators by producing cytokines, chemokines and several other inflammatory factors in response to liver injury (X. M. Chen et al., 2008).

In case of a liver injury, a NPC group called *hepatic progenitor cells* or hepatic stem cells plays an important role. The hepatic progenitor cells are a heterogeneous population capable of differentiating both into hepatocytes and into cholangiocytes as a response to a severe liver injury. They are residing mainly in the canals of Herring, in the peripheral branches of the biliary tree (Kordes & Häussinger, 2013).

1.1.2 Liver extracellular matrix

In addition to the liver cells, a small amount (< 3 %) of the liver is composed of extracellular matrix (ECM), which a non-cellular component facilitating an exchange of macromolecules between hepatocytes and plasma. In a healthy liver, ECM is mainly located in the Glisson's capsule, a connective tissue that surrounds the liver. In addition, ECM is found in portal tracts, sinusoid walls, and central veins. ECM in the liver is mainly composed of fibronectin and different collagen types depending on the location (Bedossa & Paradis, 2003). Collagen types I and III are prominent in Glisson's capsule and in portal tracts, whereas type V is found mainly in the central veins and in the portal area. Type IV is primarily present in the sinusoid walls (Bedossa & Paradis, 2003; Martinez-Hernandez, 1984). In a healthy liver, ECM synthesis and degradation is tightly balanced, nevertheless, liver injuries may disrupt this harmony and lead to severe consequences (Wei Chen et al., 2014).

1.1.3 The biliary tree

The newly synthesized bile is drained from hepatic parenchyma into the intestine via the biliary tree (Fig. 1.4), which is divided into intrahepatic and extrahepatic parts (Masyuk et al., 2012). In the intrahepatic part, the bile secreted from hepatocytes first enters into the bile canaliculi, the smallest compartment of the biliary tree with a diameter around 1 µm. At the periphery of the liver lobule, the small bile canaliculi further merge into interlobular ducts with an increasing diameter of 10-100 µm (Jansen et al., 2017). Downstream in the biliary tree, the interlobular ducts form large bile ducts of >1 mm in diameter, and finally the large ducts merge into the extrahepatic common bile duct which drains the bile into duodenum or via cystic duct into the gallbladder where the bile is stored (Boyer, 2013; Jansen et al., 2017; Masyuk et al., 2012).

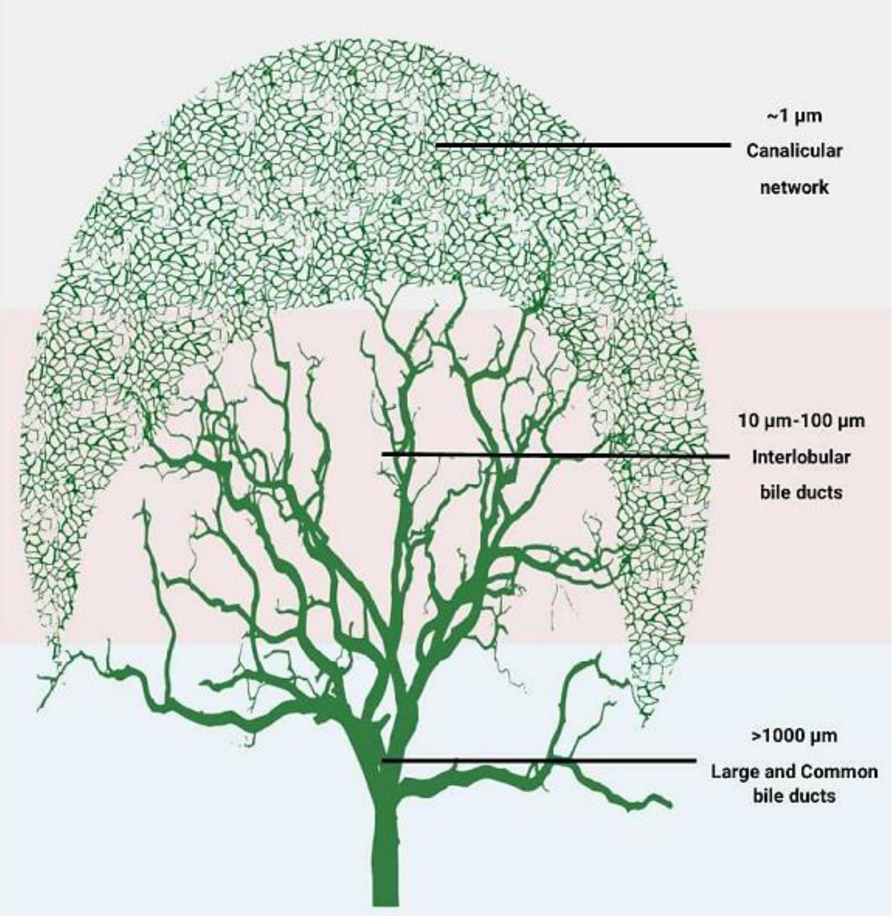

Figure 1.4. The biliary tree. The biliary tree drains the bile from hepatocytes into the duodenum and it is composed of bile canaliculi, interlobular bile ducts, large bile ducts, and common bile duct. Figure modified from Jansen et al., 2017.

1.2 Bile acids

Bile acids are small amphipathic molecules synthesized in the liver and excreted to the intestine where they facilitate lipid digestion and absorption. They act as fat emulsifiers, promoting lipid catabolism and absorption, but also as signaling molecules. Moreover, they have an important role in glucose and cholesterol metabolism, and they are responsible for approximately half of the cholesterol turnover in the body (McGlone & Bloom, 2019; Staels & Fonseca, 2009). Normally, bile acid synthesis and transport is tightly controlled. However, in chronic liver diseases such as NAFLD, the bile acid regulation mechanisms have been shown to become disturbed, leading to several complications (Ferslew et al., 2015; N. Jiao et al., 2018).

1.2.1 Bile acid synthesis and enterohepatic circulation

Bile acid synthesis involves at least 16 different enzymes and can take place via two main pathways that are regulated by feedback mechanisms. First, in the classic bile acid synthesis pathway, the synthesis primarily occurs in the microsomes of the pericentral hepatocytes (Pandak & Kakiyama, 2019; Twisk et al., 1995). Initially, cholesterol is hydroxylated into 7α-hydroxycholesterol by the rate-limiting cytochrome P450 enzyme cholesterol 7α-hydroxylase (Cyp7a1), which is regulated by bile acids. This step is followed by further modifications of the steroid rings of the cholesterol, leading to formation of 7α-hydroxy-4-cholesten-3-one. Ultimately, 7α-hydroxy-4-cholesten-3-one is converted into either cholic acid (CA) by cytochrome P450 8B1 (CYP8B1) or into chenodeoxycholic acid (CDCA) by cytochrome P450 27A1 (CYP27A1) (Fig 1.5) (Kiriyama & Nochi, 2019).

Alternatively to the classical pathway, approximately 10 % of total bile acid synthesis is initiated by the alternate or acidic pathway. In this pathway, the synthesis of CA and CDCA acid is initially catalyzed by Cyp27a1. Cyp27a1 converts cholesterol into (25R)-26-hydroxycholesterol, which is further catalyzed into CDCA by Cytochrome P450 7B1 (CYP7B1) (Fig. 1.5) (McGlone & Bloom, 2019; Pandak & Kakiyama, 2019). Although the acidic pathway is responsible for only a minor part of bile acid synthesis, its role seems to become more important in chronic liver diseases (Crosignani et al., 2007; Kiriyama & Nochi, 2019; Pandak & Kakiyama, 2019).

After the synthesis of CA and CDCA in the liver, they can become conjugated with either taurine or glycine to enhance their hydrophilicity (Fig. 1.5). Both unconjugated and conjugated bile acids are secreted into the bile in bile canaliculi and further to the gallbladder for storage as mixed micelles. Upon a meal ingestion, the micellar bile acids become released from the gallbladder into the lumen of small intestine in order to promote the digestion and absorption of lipids and lipid-soluble vitamins. In the intestine, unconjugated bile acids interact with intestinal bacteria, forming secondary bile acids (Grant & Demorrow, 2020; Staels & Fonseca, 2009). Approximately 95 % of the bile acids are reabsorbed from the ileum and transported back to the hepatocytes via the portal circulation, a process called enterohepatic circulation. The remaining 5 % of the bile acids are deconjugated in the large bowel by microbial actions, followed by either a passive absorption into the portal circulation or excretion via feces. (Meier & Stieger, 2002; Ridlon et al., 2006).

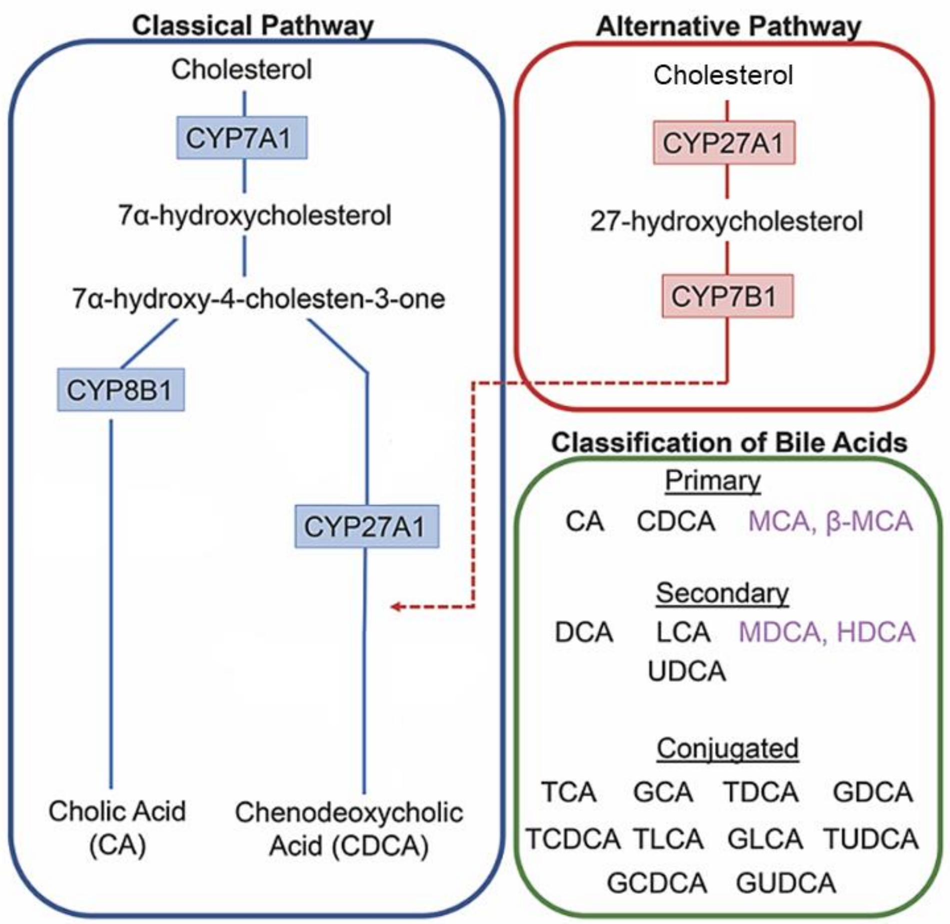

Figure 1.5. Pathways of bile acid synthesis. Bile acids can be primarily synthesized via classical pathway, where CYP7a1 catalyzes hydroxylation of cholesterol into 7α-hydroxycholesterol and 7α-hydroxy-4-cholesten-3-one, which is further converted into cholic acid (CA) or chenodeoxycholic acid (CDCA) by Cyp8B1 and Cyp27A1. In the alternate pathway, cholesterol is metabolized into (25R)-26-hydroxycholesterol by Cyp27A1 and further to CDCA by Cyp7B1. In the intestine, bacterial interactions can convert primary bile acids into secondary bile acids. Both primary and secondary bile acids can further become conjugated with taurine or glycine. Primary and secondary acids specific for rodents are indicated in purple. Figure modified from Grant & Demorrow, 2020.

The degree of bile acid synthesis is precisely regulated by the liver. Accumulation of cholesterol activates Cyp7a1 resulting in increased bile acid synthesis, whereas accumulation of bile acids leads to a negative feedback mechanism, which inhibits the activation of Cyp7a1 (Russell, 2003). A key receptor in the regulation process is nuclear farnesoid X receptor (FXR), which is expressed in several organs such as the liver and the intestine. FXR becomes activated by physiological bile acid concentrations and binds to responsive elements in the target gene promoter area either as monomer or as heterodimer with retinoid X receptor (RXR). This results in activation of the small heterodimeric partner (SHP) in the liver and fibroblast growth factor 15/19 (FGF15/19) in the intestine. Expression of SHP and FGF15/19 eventually leads to repression of Cyp7a1 transcription, resulting in decrease in bile acid production (Fig. 1.6). In addition, SHP and FGF15/19 can repress Cyp8b1, which regulates the CA/CDCA ratio in the bile acid pool (Fang, 2017; Kong et al., 2012; Russell, 2003; Sinal et al., 2000). Furthermore, FXR activation by bile acids has several physiological consequences, such as changes in triglyceride and glucose metabolism (Y. Jiao et al., 2015).

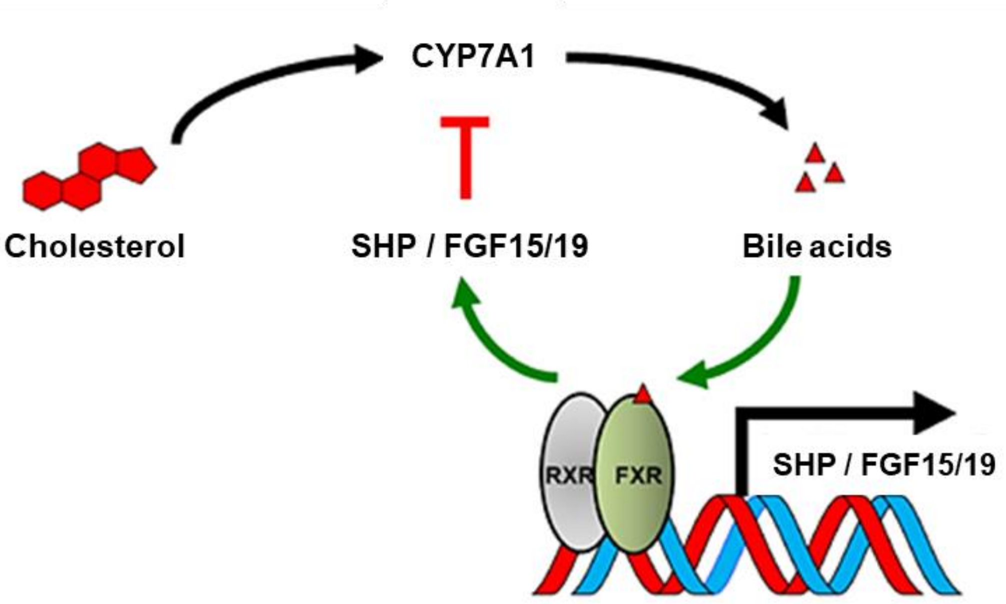

Figure 1.6. Bile acid synthesis regulation. Cholesterol is converted into bile acids by the rate-limiting enzyme Cyp7a1. The synthetized bile acids bind to FXR, leading to heterodimerization of FXR with RXR, expression of SHP and FGF15/19 and eventually to suppression of Cyp7a1. Figure modified from Fang, 2017.

1.2.2 Bile acid transporters in liver

In the liver, bile acid transport from blood to hepatocytes and further to bile canaliculi is covered by polarized expression of different bile acid transporters in the hepatocytes. First, the bile acids are taken up from the liver sinusoids into the hepatocytes by sinusoidal uptake transporters. They are expressed in the basolateral membrane of hepatocytes, where they can extract bile acids from albumin. This extraction mainly occurs in the periportal hepatocytes, creating a bile acid gradient across the zonated liver. The uptake of bile acids is carried out by Na+-taurocholate co-transporting polypeptide (NTCP) and Organic anion-transporter (OATP) family of transporters (Dawson et al., 2009; Meier & Stieger, 2002). After the sinusoidal uptake of bile acids, they are transported across the hepatocytes for secretion into the bile canaliculi. This transcellular transport is rapid in order to avoid a toxic bile acid accumulation inside the hepatocytes. The bile acids are actively transported into the bile canaliculi by the apical transporter BSEP and other ABC-family transporters, such as MRP2, which are expressed in the apical membrane of the hepatocytes (Dawson et al., 2009). In addition, bile acids can be transported from the hepatocytes to the systemic circulation by sinusoidal export transporters MRP3, MRP4 and OSTα-OSTβ (Fig. 1.7). They are located on the hepatocyte sinusoidal membrane and become expressed mainly as a hepatoprotective mechanism during cholestatic conditions in order to reduce the bile acid accumulation inside hepatocytes (Boyer et al., 2006; Zollner et al., 2007; Jansen et al. 2017).

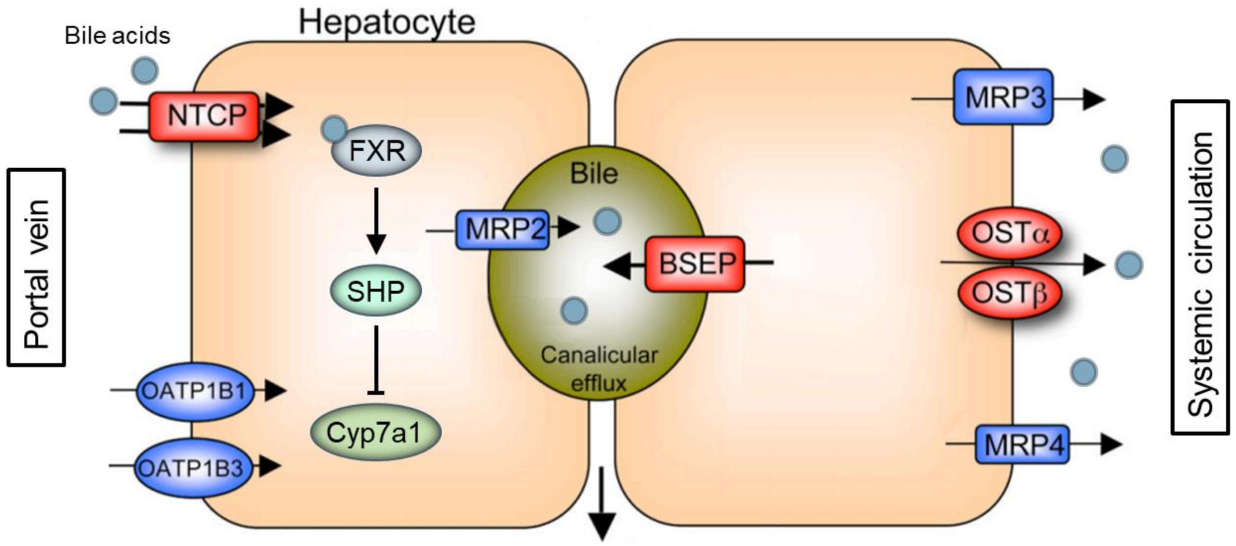

Figure 1.7. Bile acid transport in liver. Bile acids are transported from portal vein to hepatocytes via sinusoidal uptake transporters such as NTCP and OATPs. In the cell, physiological bile acid concentration activates FXR, which leads to suppression of Cyp7a1 via SHP activation. The bile acids are further transported to the bile canaliculi via BSEP and MRP2, and in some cases to systemic circulation via MRP3, MRP4, and OSTα-OSTβ. Figure modified from Dawson et al., 2009.

1.3 Liver injury

The liver can become injured due to multiple different reasons, such as drug or alcohol abuse, viral infection, autoimmune or metabolic diseases, or long-term lipid accumulation. According to the duration of liver injury, it can be arbitrarily divided into two main classes: (1) acute liver injury and (2) chronic liver injury (Malhi & Gores, 2008).

1.3.1 Acute liver injury

In acute liver injury, the liver is facing a harmful compound for a short period of time. As an acute response, different cell types work synergistically in order to eliminate the destructive agent and restores the lost liver mass. Thus, acute liver injury is often followed by a rapid resolution in order to maintain normal liver structure and function (Malhi & Gores, 2008). The exact fashion of the acute response in the liver is depending on the source of injury. Nevertheless, a characteristic acute liver injury first leads to a massive death of hepatocytes by the toxic agent, followed by an innate immune response and eventually liver tissue recovery (Iorga et al., 2017; Rock & Kono, 2008; Hoehme et al. 2010; Schliess et al. 2014; Ghallab et al. 2016).

1.3.1.1 Cell death

There are two classically accepted cell death mechanisms in acute liver injury: apoptosis, a programmed cell death, or necrosis, accidental cell death (Malhi & Gores, 2008). Moreover, in recent years, a cell death form that has adopted characteristics from both apoptosis and necrosis, necroptosis, has been revealed in many organ injuries such as in liver injury (Krumschnabel et al., 2010; Roychowdhury et al., 2012; Vucur et al., 2013).

In apoptosis, proteases called caspases become activated by an intrinsic or extrinsic trigger, such as hypoxia or proinflammatory cytokines. The activation triggers several signal cascades and eventually leads to degradation of cellular organelles and fragmentation of DNA. The cell remains of the apoptotic process are afterwards quickly removed by membrane blebbing, protrusions, or phagocytosis. As a result of this controlled cell death manner, apoptosis is a low-inflammatory process and does not trigger further liver damage (Luedde et al., 2014; Malhi & Gores, 2008).

In contrast to apoptosis, necrosis occurs in an unregulated manner as a result of physical or chemical stress. In necrosis, mitochondria become impaired, leading to a depletion of adenosine triphosphate (ATP) and failure of ATP-dependent ion pumps. As a result, the cell and its organelles rapidly swell and the cell eventually becomes ruptured, spreading the intracellular parts in the extracellular environment. This further triggers an activation of several immune cell populations, resulting in strong inflammatory response and possible further tissue damage (Iorga et al., 2017; Luedde et al., 2014).

The third form of cell death, necroptosis, is a rapid controlled cell death process in response to cell death triggers such as proinflammatory cytokines. However, in contrast to apoptosis, it is caspase-independent and it has adopted the morphological features of necrosis, such as cell and organelle swelling (Cho et al., 2009; Rosenbaum et al., 2009). Necroptosis is regulated by activation of receptor-interacting proteins (RIPs) and similarly as necrosis, it is known to activate inflammatory responses (Cho et al., 2009; Luedde et al., 2014).

In addition to the three main forms of cell death, pyroptosis and ferroptosis might take place in liver diseases. However, so far only a little is known about their contribution to the liver injury and they seem to have only a minor influence in liver damage development (Iorga et al., 2017).

Death of liver cells leads to a leakage of several liver enzymes from hepatocytes into circulation. Among these enzymes are alanine aminotransferase (ALT), aspartate aminotransferase (AST). Since the level of these enzymes in blood is in normal conditions kept relatively constant, an increase in their concentration is generally considered as a reliable biomarker of liver injury (Sookoian & Pirola, 2015). In addition, several other liver enzymes can be measured in order to evaluate the degree of liver damage and function. Both glutamate dehydrogenase (GDH) and lactate dehydrogenase (LDH) have been shown to increase in response to liver injury (Cassidy & Reynolds, 1994; Van Waes & Lieber, 1977). Moreover, alkaline phosphatase (ALP) levels are known to increase in response to liver injury especially in cholestasis, where the production of alkaline phosphatase increases as a consequence of bile acid retention within hepatocytes (Poupon, 2015; Schlaeger et al., 1982).

1.3.1.2 Activation of innate immune response

After the cell death resulting from acute liver injury, the dying cells release proinflammatory signal molecules that trigger an inflammatory response in the innate immune system of the liver. These cells include mainly Kupffer cells, dendritic cells, NK cells, and NK-T cells (Malhi & Gores, 2008). The list of possible signal molecules is long, nevertheless, the most prominent ones include heat shock proteins (HSPs), nucleosomes, a nuclear protein HMGB1, ureic acid, and released DNA content from the dying cells. The proinflammatory signals are captured in the recipient cell mainly by toll-like receptors (TLRs), which activates several proinflammatory pathways such as NF-κB pathway. The activation of these pathways leads to production of different proinflammatory cytokines, chemokines, vasoactive amines, and phospholipid metabolites (Rock & Kono, 2008; Szabo et al., 2007). That results in a recruitment and activation of further immune cells and other cell types inside and outside the liver, such as neutrophils, LSECs, and circulating macrophages as well as HSCs. Upon activation, HSCs are transdifferentiating from quiescent state into fibrogenic myofibroblasts, resulting in increased collagen type I expression in order to produce extracellular matrix (ECM) to retain the structure of the injured liver tissue (Canbay et al., 2003; Rock & Kono, 2008).

1.3.1.3 Liver regeneration

Death of the liver cells leads to their phagocytosis and removal from the liver by activated KCs. Moreover, activated LSECs and myofibroblasts start to secrete cytokines such as hepatocyte growth factor (HGF) and Wnt2, which initiate the hepatocyte proliferation in order to replace the dead hepatocytes (Malhi & Gores, 2008). As the injury-causing agent and the dead cells are removed, less proinflammatory signals are produced. In contrast, the pro-inflammatory milieu becomes shifted towards pro-restorative one, where pro-inflammatory macrophage phenotype changes into pro-resolution phenotype and they start to produce anti-inflammatory cytokine interleukin-10 (IL-10) and matrix metalloproteinases (MMPs). As a result, the number and activation of pro-inflammatory monocytes and NK-T cells in the damaged area decreases, whereas dendritic cells and NK cells become more prominent, inducing apoptosis of ECM-producing myofibroblasts. Lastly, the increased production of MMPs leads to a degradation of excessive ECM, restoring the structure and function of the liver tissue (Malhi & Gores, 2008; Ramachandran et al., 2012; Tacke & Trautwein, 2015).

1.3.2 Chronic liver injury

Although the liver injury is aimed to keep transient and a rapid recovery normally follows the acute insult, in some cases the injury is sustained for long periods of time, termed as chronic liver injury. There are several underlying causes for chronic liver injury development, such as viral infection, repeated exposure to toxins, or obesity and metabolic diseases (Asrani et al., 2019). In that case, continuous cell death is present, and immune cells and myofibroblasts remain active, leading to a chronic inflammation and substitution of liver parenchyma by ECM, i.e. fibrosis (Hernandez-Gea & Friedman, 2011).

Even though production of ECM by myofibroblasts is a crucial step in liver injury healing process, when the production exceeds degradation, ECM accumulates in the liver tissue. The fibrosis pattern can diverge from pericentral to periportal or midzonal according to the origin of the injury and the liver cells involved. In a characteristic manner, fibrotic bridges start to form between the fibrotic lesions. If the chronic injury persists, fibrosis further progresses and invades most parts of the liver tissue (Hernandez-Gea & Friedman, 2011). In addition to the increase in ECM accumulation, the structure of ECM in chronic liver injury changes as well. Although fibrosis increases the total amount of all collagen types, their expression in different chronic liver injury stages varies (Wei Chen et al., 2014; Olaso et al., 2001). Collagen type V is shown to increase in the early stages of fibrosis, whereas types III and IV become more prominent in the later stages of chronic liver injury (Chen et al., 2014). These changes in ECM accumulation and quality result in functional deterioration in the hepatic blood flow between sinusoids and hepatocytes, leading eventually to impairment in the liver function. Even though fibrosis itself is reversible, it can lead to irreversible liver cirrhosis (Hernandez-Gea & Friedman, 2011).

Activation of the innate immune system is crucial in protection against acute insult and in liver injury restoration. However, in chronic liver injury the immune system enhances the fibrosis progression. As the injury-causing agent in the liver is not removed, the accumulation and activation of immune cells becomes permanent. As a result, activated immune cells keep producing not only proinflammatory cytokines but also fibrogenic mediators such as TGF-β, promoting liver fibrosis (Hernandez-Gea & Friedman, 2011; Szabo et al., 2007).

1.4 NAFLD

The prevalence of chronic liver diseases is continuously expanding worldwide, leading to an increasing burden on the global health care. One of the main types of chronic liver diseases is nonalcoholic fatty liver disease (NAFLD) with emerging global prevalence of around 25 % (Younossi et al., 2016). The underlying causes of NAFLD are mainly associated with metabolic changes, such as obesity, dyslipidemia, and diabetes mellitus, nevertheless always excluding alcohol abuse (Chalasani et al., 2018). NAFLD comprises a range of different stages from simple liver steatosis to non-alcoholic steatohepatitis (NASH), liver cirrhosis, and hepatocellular carcinoma (HCC).

1.4.1 Hepatic lipid metabolism

Lipids are a heterogeneous group of hydrophobic amphipathic molecules required for cell structure maintenance, as an energy source, and in cell signaling (Huang & Freter, 2015).The liver has a key role in lipid metabolism by regulating fatty acid biosynthesis, release, and storage during both feeding and fasting (Nguyen et al., 2008).

There are three major sources of hepatic fatty acids: dietary lipids, *de novo* synthesis, and adipose tissue-derived fatty acids. In the first case, food-derived fatty acids are emulsified by bile acids, transformed into triglycerides, and transported as chylomicrons into plasma and eventually to their target tissues, mainly muscles or adipose tissue. In contrast to dietary lipid metabolism, *de novo* synthesis takes place in carbohydrate excess, as the liver converts glucose or fructose into fatty acids (Nguyen et al., 2008). In a healthy liver, this pathway contributes only approximately 5 % to the total lipid content, nevertheless, increased *de novo* lipogenesis has been connected to NAFLD (Knebel et al., 2012). Moreover, upon fasting, triglycerides from the adipose tissue can be released to be used as an energy source (Barrows & Parks, 2006). In this process called lipolysis, triglycerides from the adipose tissue are converted back to fatty acids and released into plasma for the hepatic fatty acid uptake (Fig.1.8) (Alves-Bezerra & Cohen, 2018).

In order to be metabolized, fatty acids are transformed into acyl-coenzyme A molecules, which can be secreted into plasma as triglyceride-enriched very low-density lipoprotein (VLDL-TG) particles or become further processed by the liver in a process called β-oxidation or fatty acid oxidation, which results in energy production in the form of adenosine triphosphate (ATP). In addition, a small part of the acyl-CoA pool undergoes TG synthesis and are packed into VLDL to be transported into other organs. In a healthy liver, the hepatic triglyceride accumulation is balanced with β-oxidation and VLDL-TG secretion. (Alves-Bezerra & Cohen, 2018; Kawano & Cohen, 2013). However, if the balance becomes disrupted for example due to increasing intake of dietary lipids, β-oxidation and VLDL-TG release are not sufficient to counteract the triglyceride uptake. As a result, triglycerides start to accumulate inside the hepatocytes as cytoplasmic lipid droplets, leading to a development NAFLD (Fig. 1.8) (Alves-Bezerra & Cohen, 2018; Kawano & Cohen, 2013; Nguyen et al., 2008)

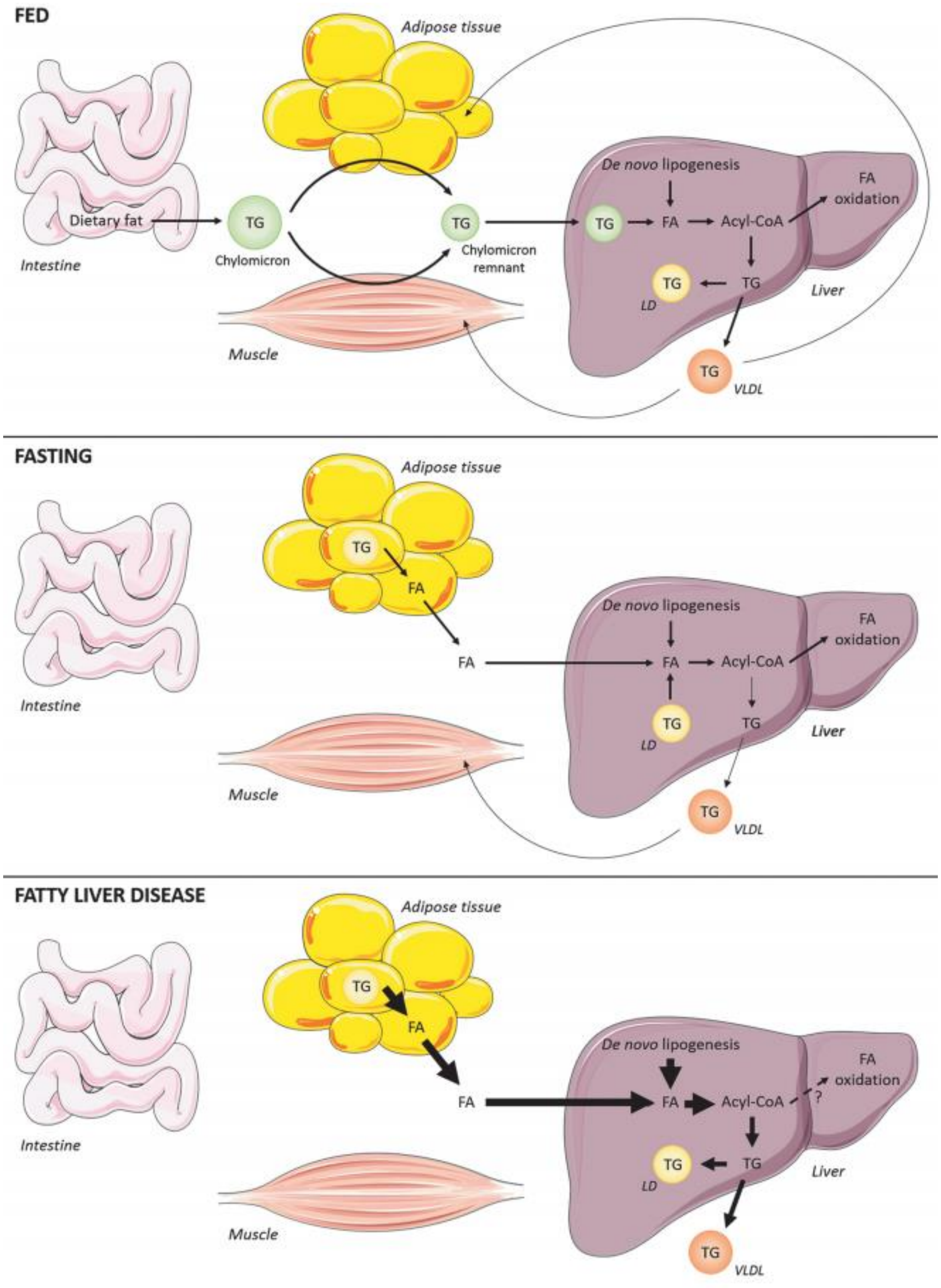

Figure 1.8. Fatty acid metabolism. Fatty acids can be derived from dietary lipids, by de novo lipogenesis, and from adipose-tissue derived fatty acids. In a fed state, triglycerides (TGs) are transported from the small intestine into target tissues as chylomicrons. In the liver, they are processed, resulting in fatty acid (FA) release within hepatocytes. FAs can be stored in the liver as lipid droplets (LDs) or FAs can be activated into Acyl-CoA molecules, further oxidized to produce energy or synthesized into TGs and transported into target organs as VLDL-TGs. During fasting, adipocyte and hepatocyte TG stores can be mobilized to plasma and target organs. In fatty liver disease, FA supply overcomes oxidation, resulting in increased lipid storage in the liver and VLDL-TG overproduction. Figure from Alves-Bezerra & Cohen, 2018.

1.4.2 NAFLD progression

NAFLD is characterized primarily by accumulation of lipid content inside the hepatocytes. As an onset of NAFLD, the homeostatic mechanism regulating lipid synthesis and degradation is disturbed, and at the first stage of NAFLD (benign steatosis), more than 5 % of hepatocytes become steatotic (Mitra et al., 2020; Perry et al., 2014). Nevertheless, no additional signs of liver damage are present, and the risk of patients with benign steatosis to develop liver cirrhosis is still considered as minimal (Chalasani et al., 2018). However, in approximately 20-30 % of cases the disease progresses further to an inflammatory type of NAFLD, non-alcoholic steatohepatitis (NASH) (Fig. 1.9) (Sheka et al., 2020; Wong et al., 2010). In NASH, signs of liver injury and inflammation become prevalent. The majority of NASH patients are asymptomatic or have non-specific symptoms, and currently the only approved diagnostic tool for distinguishing NASH from simple steatosis is liver biopsy. In NASH, liver histology shows hepatocyte steatosis and ballooning as well as liver inflammation, indicated as activation and infiltration of immune cells such as macrophages. The activation of immune cells leads to a production of proinflammatory cytokines, causing liver inflammation. Moreover, liver transaminases such as ALT and AST are often elevated as markers of liver injury (Chalasani et al., 2018; Lopez Amador et al., 2017; Sheka et al., 2020). As a result of liver injury, an increased cell death and fibrosis is observed in NASH (Fig. 1.9) (Kanda et al., 2018). In addition, new bile ducts are reported to form during NASH in response to liver injury (Gadd et al., 2014). In contrast to simple steatosis where the probability of developing liver cirrhosis is notably low, more than 20 % of NASH patients eventually develop cirrhosis (Sheka et al., 2020).

The transition from NASH to liver cirrhosis involves degradation of healthy liver tissue, accumulation of fibrosis, sinusoidal remodeling, and eventually hepatic endothelial dysfunction, portal hypertension, and compromised hepatic circulation (Tsochatzis et al., 2014). The deterioration of hepatic circulation leads not only to a decompensation of liver functions but also to several extrahepatic consequences such as renal failure (Bittencourt et al., 2015). Unlike simple steatosis and NASH, cirrhosis is generally not reversible and liver transplantation is the only available intervention. Furthermore, liver cirrhosis is the main underlying cause of HCC, where the 5-year survival rate is less than 10 % (Manghisi et al., 1998; Sarveazad et al., 2019).

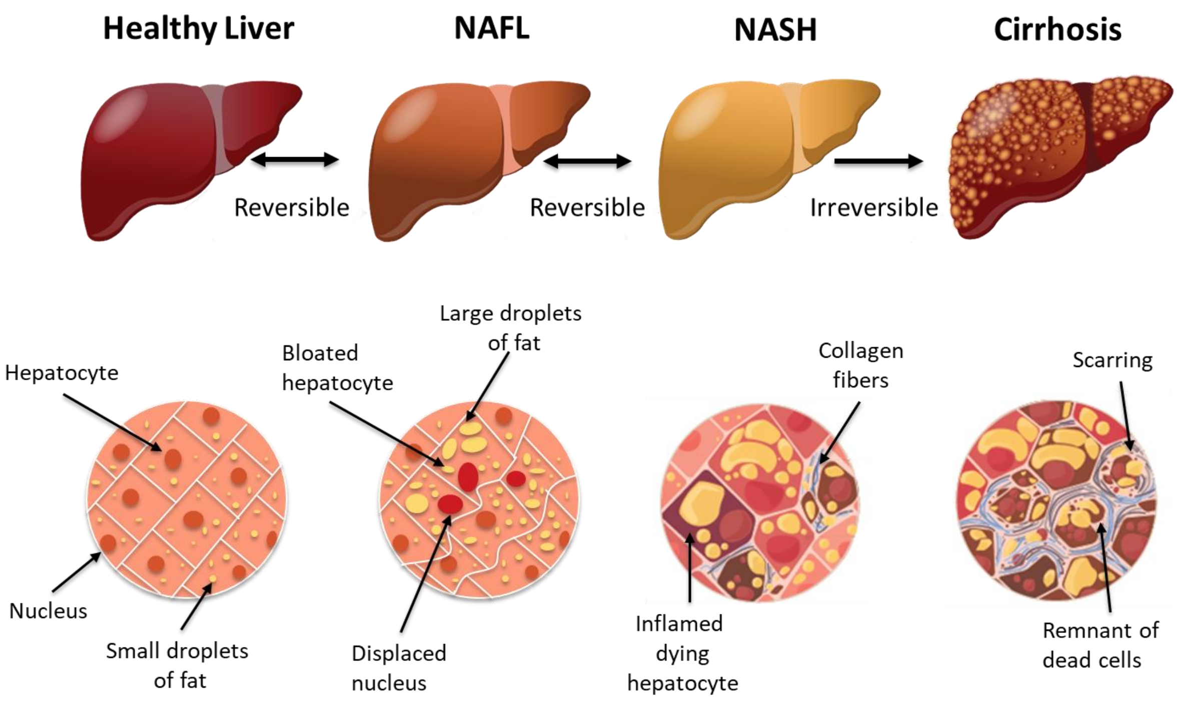

Figure 1.9. NAFLD progression. NALFD develops as lipid droplets start to accumulate inside the hepatocytes, leading to progression of the liver into NAFL or benign steatosis. NAFL can further progress into NASH, where liver injury is present. In some cases, the liver further develops cirrhosis, an irreversible stage of NAFLD with heavy liver damage and deterioration of liver function. Figure modified from http://www.hcv-trials.com/nash/NAFLD-NASH.asp.

1.4.3 Lipid zonation in NAFLD

Zonation of lipid metabolism influences the pathogenesis of NAFLD. Although the pattern of lipid accumulation can vary, several clinical studies have shown that in the majority of human NAFLD patients, lipids are mainly accumulated in the pericentral compartment of the liver lobule (Chalasani et al., 2008; Kleiner & Makhlouf, 2016; Zhuang et al., 2020). This pattern has been considered as a consequence of metabolic zonation (Fig.1.10), where the pericentral hepatocytes are involved in glycolysis and lipogenesis, whereas the periportal hepatocytes have a higher rate of β-oxidation and thus less lipid accumulation (Guzman & Castro, 1989; Kietzmann, 2017). Moreover, in human NAFLD patients macrovesicular steatosis is more prominent compared to microvesicular steatosis, meaning that the hepatocytes are rather filled with one big lipid droplet than several small ones (Brunt et al., 1999; Kleiner & Makhlouf, 2016).

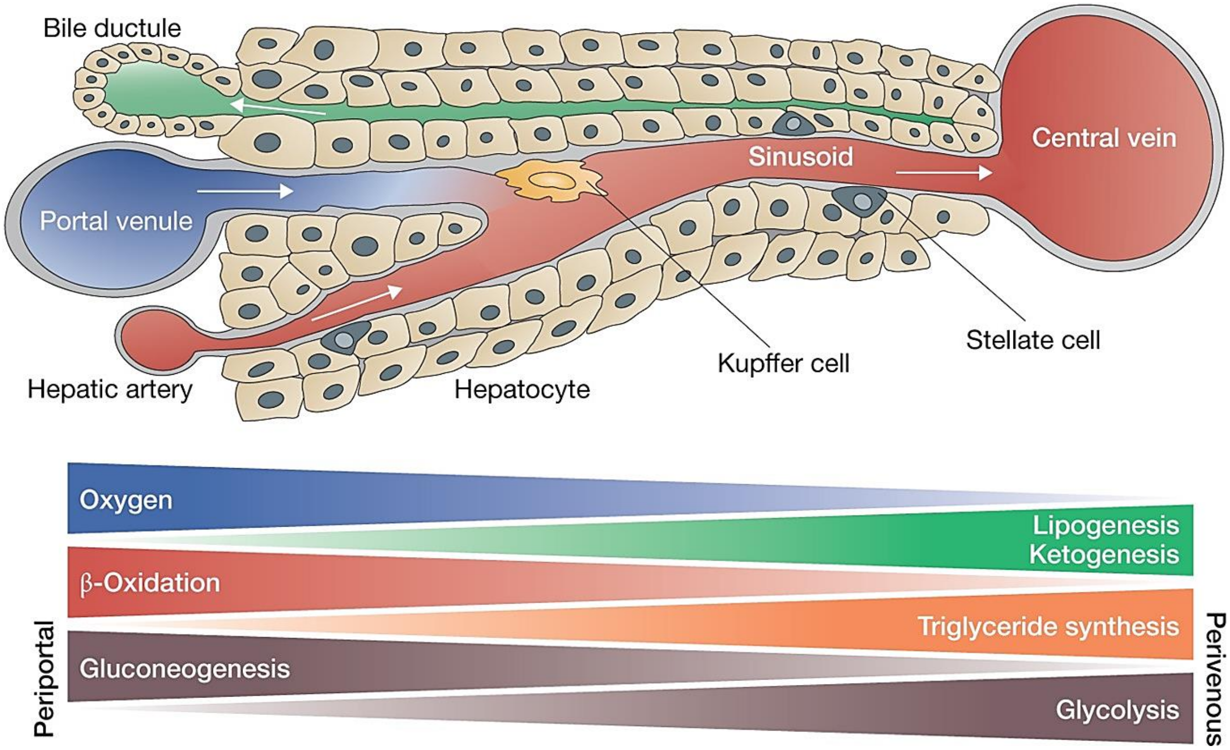

Figure 1.10. Zonation of lipid metabolism along the porto-central axis of the liver lobule. Fatty acid metabolism shows a gradient type of zonation in the liver lobule. β-oxidation occurs mainly in the periportal hepatocytes, whereas lipogenesis takes place mainly in the pericentral hepatocytes. Figure modified from Birchmeier, 2016.

1.4.4 NAFLD treatment

Until now, there are no approved drugs for treatment of NASH (Friedman, Neuschwander-Tetri, et al., 2018; Rinella et al., 2019). Currently, the most efficient method for restricting NAFLD progression is modifications of diet and lifestyle. NAFLD patients are advised to reduce their calorie intake and increase their physical activity in order to decrease the lipid accumulation in the liver tissue. Clinical studies have shown that weight loss can improve the stage of NAFLD by reducing fibrosis, lobular inflammation, and steatosis (Dixon et al., 2004; Promrat et al., 2010). It has been shown that even 7-10 % loss of bodyweight can improve the liver histology of NAFLD patient (Vilar-Gomez et al., 2015). Unfortunately, many patients fail to follow the dietary and physical activity approaches (Centis et al., 2010). Thus, in addition to lifestyle modification, pharmacological therapies are aimed to develop in order to prevent NAFLD progression. Several pharmacological compounds with different acting mechanisms are being tested in clinical trials but not yet approved. For example, drugs Elafibranor and Pioglitazone are activators of peroxisome proliferator-activated receptors (PPARs) that enhance fatty acid and glucose metabolism. Moreover, a drug Cenicriviroc is a dual antagonist of C–C chemokine receptors, whereas vitamin E treatment seems to have an anti-inflammatory and anti-apoptotic effect in NAFLD (Friedman, Ratziu, et al., 2018; Perumpail et al., 2018; Pydyn et al., 2020). Interestingly, a semi-synthetic bile acid analogue obeticholic acid (OCA) has been shown to be efficient in treatment of NAFLD and NASH (Abenavoli et al., 2018). OCA acts as an FXR agonist, inhibiting bile acid synthesis. At the moment, OCA is registered as primary sclerosing cholangitis treatment, however, several clinical trials have shown OCA to decease liver steatosis, fibrosis, and lobular inflammation in NAFLD (Abenavoli et al., 2018; Mudaliar et al., 2013; Neuschwander-Tetri et al., 2015). Interestingly, the exact mechanism of OCA in NAFLD is still unclear.

1.5 Aim of the work

NAFLD is one of the main underlying causes of chronic liver diseases worldwide with a yearly increasing prevalence. However, in spite of the NAFLD importance in our society, there is currently no approved medical treatment for it. In addition, even though the characteristics of different NAFLD stages are well known and widely observed in the patients, the driving force behind the transition of simple steatosis to NASH and further to liver cirrhosis is still largely unknown. The overarching goal of this work was to investigate the mechanisms of NAFLD stage transitions and to establish preventive measures for the progression from benign steatosis to NASH. To accomplish this goal, the work program was structured into the following tasks:

1. Establish a NAFLD mouse model that recapitulates all the stages from simple steatosis to liver cirrhosis and HCC.
2. Identify the molecular mechanisms responsible for NAFLD stage transitions.
3. Investigate the alteration in bile acid transport during NAFLD progression, and its role in stage transitions.
4. Target the identified mechanisms of stage transitions and design therapeutic interventions to intervene the NAFLD progression.

2 MATERIALS AND METHODS

2.1 Materials

2.1.1 Chemicals

Table 2.1. Chemicals

Chemical	**Company**
2-Methylbutane	Merck, Darmstadt, Germany
β-Mercaptoethanol	
Acetic acid (100 %, p.a.)	Carl Roth, Karlsruhe, Germany
Acrylamid	Sigma-Aldrich, St. Louis, USA
AEC+ high sensitivity substrate chromogen	DakoCytomation A/S, Glostrup, Denmark
Amersham™ ECL™ Prime Western Blotting Detection Kit	Cytiva, Chicago, USA
Ammonium persulfate (APS)	Sigma-Aldrich, St. Louis, USA
Aquatex mountig agent	Merck, Darmstadt, Germany
Bio-Rad Protein Assay Dye Reagent Concentrate	Bio-Rad, Hercules, USA
Bovine Albumin Fraction V (BSA)	Carl Roth, Karlsruhe, Germany
Citric acid monohydrate	Carl Roth, Karlsruhe, Germany
Clodronate Liposomes	Clodronate Liposomes, Amsterdam, Netherlands
cOmplete™ Mini Protease Inhibitor Cocktail	Roche, Mannheim, Germany
DAB Substrate Kit with Nickel, (3,3'-diaminobenzidine)	Vector Laboratories, Burlingame, USA
DNAZap™ PCR DNA Degradation Solutions	Invitrogen, Carlsbad, USA
EnVision+HRP (mouse/AEC) kit	DakoCytomation A/S, Glostrup, Denmark
DeadEnd colorimetric TUNEL kit	Promega, Mannheim, Germany
DeadEnd fluorometric TUNEL kit	Promega, Mannheim, Germany
Diamidino-2-phenylindole (DAPI)	Invitrogen, Karlsruhe, Germany

di-Sodium hydrogen phosphate, anhydrous	AppliChem, Darmstadt, Germany
DTT	Roche, Mannheim, Germany
Entellan	Merck, Darmstadt, Germany
Eosin Y disodium salt	Sigma-Aldrich, St. Louis, USA
Ethanol denatured (≥ 99.8 %)	Carl Roth, Karlsruhe, Germany
Ethylenediaminetetraacetic acid (EDTA) disodium salt	Sigma-Aldrich, St. Louis, U.S.
FluorSave^{TM} Reagent	Merck, Darmstadt, Germany
High-Capacity cDNA Reverse Transcription Kit	Applied Biosystems, Foster City, USA
Hydrochloric acid	Carl Roth, Karlsruhe, Germany
Hydrogen peroxide (30 %)	Carl Roth, Karlsruhe, Germany
Imipramine hydrochloride	Sigma-Aldrich, St. Louis, USA
Immobilon®-P PVDF membrane	Sigma-Aldrich, St. Louis, USA
Ketamine (10 %)	Medistar Arzneimittelvertrieb GmbH, Ascheberg, Germany
Laemmli-Sample Buffer 2x	Bio-Rad, Hercules, USA
Magic Mark XP Western Protein Standard	Invitrogen, Darmstadt, Germany
Mayer's Hemalum solution	Merck, Darmstadt, Germany
Methanol	Carl Roth, Karlsruhe, Germany
Methanol-free formaldehyde	Carl Roth, Karlsruhe, Germany
Methyl cellulose	Sigma-Aldrich, St. Louis, USA
Mouse on Mouse Polymer IHC Kit	Abcam, Cambridge, U.K.
Nile Red	Invitrogen, Carlsbad, USA
Normal donkey serum	Sigma-Aldrich, St. Louis, USA
NP-40 Surfact-Amps™ Detergent Solution	Thermo Fisher Scientific, Waltham, USA
NuPAGE™ Transfer Buffer	Thermo Fisher Scientific, Waltham, USA
Obeticholic acid	Ambeed, Arlington Heights, USA

Pefabloc® SC	Roche, Mannheim, Germany
PhosSTOP™	Roche, Mannheim, Germany
Picrosirius Red Stain Kit	Polysciences Inc., Warrington, USA
Ponceau S	Sigma-Aldrich, St. Louis, USA
Potassium chloride (≥ 99.5 %, p.a.)	Carl Roth, Karlsruhe, Germany
Prequillan (acepromazine)	Fatro, Ozzano dell'Emilia, Italy
QIAzol Lysis Reagent	Qiagen, Hilden, Germany
Richard-Allan Scientific™ NEG-50	Thermo Fisher Scientific, Waltham, USA
Rompun 2 % (xylazine 2 %)	Bayer Health Care, Leverkusen, Germany
Roti-Histofix 4%	Carl Roth, Karlsruhe, Germany
Roti-Histol	Carl Roth, Karlsruhe, Germany
Sodium chloride (≥ 99.5 %, p.a.)	Carl Roth, Karlsruhe, Germany
Sodium dodecyl sulfate (SDS)	Sigma-Aldrich, St. Louis, USA
Sodium hydroxide	Merck, Darmstadt, Germany
Sucrose	Merck, Darmstadt, Germany
Surgipath-paraplast	Leica Biosystems, Wetzlar, Germany
TaqMan® Universal Master Mix II with UNG	Thermo Fisher Scientific, Waltham, USA
Tetramethylethylenediamine (TEMED)	Sigma-Aldrich, St. Louis, USA
TRIS PUFFERAN (≥ 99.9 %, p.a.)	Carl Roth, Karlsruhe, Germany
TritonTM X-100	Sigma-Aldrich, St. Louis, USA
UltraPure™ DEPC-Treated Water	Invitrogen, Carlsbad, USA
TWEEN® 20	Sigma-Aldrich, St. Louis, USA
Xylene	VWR international, Darmstadt, Germany

Table 2.2. Antibodies and fluorescent dyes

Primary antibody	Catalog no.	Company
Goat anti-liver Arginase	NB100-59740	Novus Biologicals, Littleton, USA
Mouse anti-β-Catenin	610154	BD Biosciences, Heidelberg, Germany
Mouse anti-GAPDH	MCA4739	AbD Serotec, Hercules, USA
Mouse anti-human α-SMA	M085129-2	DakoCytomation A/S, Glostrup, Denmark
Rabbit anti-Cleaved Caspase-3	9661	Cell Signaling Technology, Danvers, USA
Rabbit anti-human BSEP	LS-C490094	LSBio, Seattle, USA
Rabbit anti-MLKL	orb32399	Biorbyt Ltd, Cambridge, U.K.
Rabbit anti-mouse CD13	ab108310	Abcam, Cambridge, U.K.
Rabbit anti-mouse CK19	ab5265	Abcam, Cambridge, U.K.
Rabbit anti-mouse CYP2E1	HPA009128	Sigma-Aldrich, St. Louis, USA
Rabbit anti-mouse Desmin	RB-9014-P0	Thermo Fisher Scientific, Waltham, USA
Rabbit anti-mouse Ki67	12202S	Cell Signaling Technology, Danvers, USA
Rabbit anti-mouse NTCP	PA5-80001	Thermo Fisher Scientific, Waltham, USA
Rat anti-mouse CD13	MCA2183	Bio-Rad, Hercules, USA
Rat anti-mouse CD45	550539	BD Bioscience, Heidelberg, Germany
Rat anti-mouse F4/80	MCA497G	Bio-Rad, Hercules, USA

Rat anti-mouse Ly6G	551459	BD Bioscience, Heidelberg, Germany

Secondary antibody	**Catalog no.**	**Company**
Cy™2 AffiniPure Donkey Anti-Mouse IgG (H+L)	715-225-150	Jackson ImmunoResearch Laboratories, West Grove, USA
Cy™5 AffiniPure Donkey Anti-Goat IgG (H+L)	705-175-147	Jackson ImmunoResearch Laboratories, West Grove, USA
Cy™5 AffiniPure Donkey Anti-Rat IgG (H+L)	712-175-153	Jackson ImmunoResearch Laboratories, West Grove, USA
HRP-linked anti-mouse immunoglobulin G	NA931	Cytiva, Chicago, USA
HRP-linked anti-rabbit immunoglobulin G	NA934	Cytiva, Chicago, USA
Polyclonal Swine Anti-Rabbit Immunoglobulins/HRP	P0217	Dako, Glostrop, Denmark

Fluorescent dye	**Catalog no.**	**Company**
Bodipy™ 493/503	D3922	Life Technologies, Eugene, USA
Cholyl-lysyl-fluorescein (CLF)	451041	BD Biosciences, Heidelberg, Germany
Hoechst 33258	H1398	Thermo Fisher Scientific, Waltham, USA
Tetramethylrhodamine ethyl ester (TMRE)	T669	Thermo Fisher Scientific, Waltham, USA

Table 2.3. Reagents for Discovery Ultra Automated Slide Preparation System

Reagent	**Company**
Bluing Reagent	Roche, Mannheim, Germany
Discovery Ab Diluent (Casein)	Roche, Mannheim, Germany

Discovery CC1	Roche, Mannheim, Germany
Discovery ChromoMap DAB Kit	Roche, Mannheim, Germany
Discovery Inhibitor	Roche, Mannheim, Germany
Discovery Purple Kit (RUO)	Roche, Mannheim, Germany
Discovery UltraMap anti-Rt HRP	Roche, Mannheim, Germany
Discovery UltraMap anti-Rb AP	Roche, Mannheim, Germany
Discovery UltraMap anti-Rb HRP	Roche, Mannheim, Germany
Discovery Wash (RUO)	Roche, Mannheim, Germany
Discovery Yellow Kit (RUO)	Roche, Mannheim, Germany
EZ Prep	Roche, Mannheim, Germany
Hematoxylin II	Roche, Mannheim, Germany
Reaction Buffer	Roche, Mannheim, Germany
SSC	Roche, Mannheim, Germany
Ultra LCS	Roche, Mannheim, Germany

2.1.2 Consumables

Table 2.4. Consumables

Consumable	Company
100 Sterican needles (26 G)	B. Braun, Melsungen, Germany
BD Microlance 3 TM needles (30 G)	Becton Dickinson, Heidelberg, Germany
Cover Slips (0.17 mm)	Logitech, Glasgow, UK
Cover Slips (22 x 32 mm #1.5)	Thermo Fisher Scientific, Waltham, USA
DAKO Pen	Dako, Glostrop, Denmark
DWK Life Sciences Wheaton™ Glass 20mL Scintillation Vials	Thermo Fisher Scientific, Waltham, USA
Falcon tubes (50 ml, 15 ml)	Sarstedt AG & Co. KG, Numbrecht, Germany

Filter Paper	Marchery-Nagel, Düren, Germany
Fisherbrand™ 20mL HDPE Scintillation Vials with Polypropylene Cap	Thermo Fisher Scientific, Waltham, USA
Injekt®-F syringes	B.Braun, Melsungen, Germany
Microscope Slides Superfrost ® Plus	Thermo Fisher Scientific, Waltham, USA
Microtome Blade A35	Feather, Osaka, Japan
Microtome Blade N35 HR	Feather, Osaka, Japan
Omnican® 100 syringes	B. Braun, Melsungen, Germany
Parafilm® M	Sigma-Aldrich, St. Louis, USA
Piccolo® General Chemistry 13 Panel	Abaxis, Union City, USA
Pipette tips	Sarstedt AG & Co. KG, Numbrecht, Germany
PCR SingleCap 8er-SoftStrips 0.2 ml	Biozym, Hessisch Oldendorf, Germany
RNase-Free tubes 1.5 ml	Ambion GmbH, Kaufungen, Germany
SafeSeal tubes 0.5 ml	Sarstedt AG & Co. KG, Numbrecht, Germany
Standard Cryomold® cassettes	VWR international, Darmstadt, Germany
TC Plate 24 Well Standard	Sarstedt AG & Co. KG, Numbrecht,
TGRADIENT Biometra thermocycler	Analytik Jena, Jena, Germany
Tissue-Loc® Biopsy Cassettes	Thermo Fisher Scientific, Waltham, USA
Transfer pipettes	Sarstedt AG & Co. KG, Nümbrecht, Germany
Whatman® filter paper	Sigma-Aldrich, St. Louis, USA

2.1.3 Technical equipment

Table 2.5. Technical equipment and software

Instrument	Company
7500 Real-Time PCR System	Applied Biosystems, Foster City, USA
ALS/ALJ Analytical Balance Scale	KERN & SOHN GmbH, Balingen, Germany
Axio Scan.Z1	Zeiss, Jena, Germany
BX41microscope	Olympus Europa SE & Co.KG, Hamburg, Germany
Confocal Laser Scanning Microscope FLUOVIEW FV1000	Olympus Europa SE & Co.KG, Hamburg, Germany
Cryostat Leica CM3050 S	Leica Biosystems, Wetzlar, Germany
DISCOVERY ULTRA Automated Slide Preparation System	Roche, Mannheim, Germany
Dual-Action Shaker KL 2	Edmund Buhler GmbH, Bodelshausen, Germany
E-Bar II Label printer	Roche, Mannheim, Germany
EC 350 – modular tissue embedding center	Microm, Walldorf, Germany
FS5100 Steam cooker	Braun, Kronberg im Taunus, Germany
Heraeus Fresco 21 Centrifuge, Refrigerated	Thermo Fisher Scientific, Waltham, USA
HM 450 Sliding Microtome	Microm, Walldorf, Germany
Incubator	Binder, Tuttlingen, Germany
LSM MP7	Zeiss, Jena, Germany
Magnetic stirrer IKAMAG RCT	IKA, Staufen, Germany
Microwave	Robert Bosch GmbH, Gerlingen, Germany
Mini-Star centrifuge	VWR international, Darmstadt, Germany

Nanodrop 2000 spectrometer	Thermo Fisher Scientific, Waltham, Germany
Olympus U-RFL-T	Olympus Europa SE & Co.KG, Hamburg, Germany
PB602 Precision Balance	Mettler Toledo, Columbus, USA
pH Meter lab 850	SI analytics GmbH, Mainz, Germany
Piccolo Xpress® chemistry analyzer	Abaxis, Union City, USA
Pipettes	Eppendorf, Hamburg, Germany
PrintMate™ AS Cassette Printer	Thermo Fisher Scientific, Waltham, USA
SlideMateTM AS Slide Printer	Thermo Fisher Scientific, Waltham, USA
SONOPLUS Ultrasonic Homogenizer	BANDELIN electronic GmbH, Berlin, Germany
STP 120 Spin Tissue Processor	Thermo Fisher Scientific, Waltham,
TDO Sahara Tissue Drying Oven	Medite, Burgdorf, Germany
Vilber Fusion Fx7	Vilber Lourmat, Collégien, France
Vortex	neoLab, Heidelberg, Germany

Software	**Company**
LabWriter	Thermo Fisher Scientific, Waltham, USA
ImarisFileConverter 9.5.1	Bitplane, Zurich, Schweiz
Imaris x64 9.5.1	Bitplane, Zurich, Schweiz
Prism, version 8.4.3	GraphPad Software, San Diego, USA
ZEN 3.1 (blue edition)	Zeiss, Jena, Germany
FV10-ASW 4.1 Viewer	Olympus Europa SE & Co.KG, Hamburg, Germany

2.1.4 Buffers and solutions

Table 2.6. Buffers and solutions

10 x PBS	10 g KCl 10 g KH2PO4 400 g NaCl 46 g Na2HPO4 pH 7.4 Filled up to 5 liter with distilled water
Bodipy	1.3 mg Bodipy Dissolve in 1 ml DMSO Store at -20° C
10 x TBS	80 g NaCl 2 g KCl 30 g Tris pH 7.4 Filled up to 1 liter with distilled water
Anesthesia	128 µl ketamine 72 µl xylazine 340 µl acepromazine 460 µl 1 x PBS
EDTA solution (anti-coagulant)	32 mg EDTA Dissolved in 1 ml distilled H_2O
Eosin (1 %)	2 g Eosin 200 ml distilled water 2 drops of glacial acetic acid Filtered before usage
EtOH 95 % + acetic acid (2:1)	330 ml EtOH (95 %) 170 ml acetic acid (100 %)
H_2O_2 (10 %)	20 ml H_2O_2 180 ml methanol
Hematoxylin	40 ml Mayer’s Hemalum 160 ml distilled water Filtered before usage

Laemmli-Sample buffer + β-mercaptoethanol	950 µl Laemmli-Sample buffer 2x 50 µl β-mercaptoethanol
Methanol-free formaldehyde (3 %)	50 ml 30 % methanol-free formaldehyde 350 ml 1x PBS
Methyl cellulose (0.5 %)	2.5 g methyl cellulose Dissolved in 500 ml distilled H_2O
NP-40 lysis buffer	25 ml 1M Tris-HCl 15 ml 5M NaCl 2.5 ml Surfact-Amps™ Detergent 425.5 ml distilled H_2O add 1 cOmplete™ Mini Protease Inhibitor Cocktail Tablet
NP-40 lysis solution	1 cOmplete™ Mini Protease Inhibitor Cocktail tablet in 1 ml distilled H_2O 9 ml NP-40 lysis buffer 1 PhosSTOP™ tablet 10 µl 1M DTT 100 µl 0.1M PEFA Block
Paraformaldehyde (PFA) 3 %	150 ml 4 % paraformaldehyde 50 ml 1x PBS
PBS + 1 % BSA + 0.5 % Tween20	10 g BSA 20.3 g NaCl 5 ml Tween20 Dissolved in 1 liter 1 x PBS
PBS-T	1x PBS 0.5 % Triton-X-100
PBS-T + 0.5% BSA + 5 % donkey serum	2.5 g BSA 25 ml donkey serum Diluted in 500 ml PBS-T
PBS-T + 1 % BSA + 10 % donkey serum	5 g BSA 50 ml donkey serum Diluted in 500 ml PBS-T

Sucrose (30 %)	60 g sucrose Dissolved in 200 ml 1 x PBS
TBS-T	1 x TBS 0.5 % Tween 20
Tris/HCl (0.1 M)	3.925 g Tris 250 ml distilled H_2O pH 7.6
Tris/HCl (1 M)	39.25 g Tris 250 ml distilled H_2O
Tris-EDTA	1.21 g Tris 0.29 g EDTA pH 9.0 Filled up to 1 liter with distilled water

2.2 Methods

2.2.1 Animal models

Male mice from two different strains were used in the experiments: (1) C57Bl/6N and (2) td-Tomato reporter mice. The mice were housed in temperature controlled room of 23° C with 12 hours light, 12 hours dark cycles and fed *ad libitum* either with Ssniff R/M-H, 10mm standard diet (Ssniff, Soest, Germany) or with western-style diet (WD) containing 40 % kcal fat, 20 % kcal fructose, and 2 % cholesterol (D09100301, Research Diets, New Brunswick, USA) up to 54 weeks. A detailed description of the WD ingredients is given in table 2.7. All the experiments were approved by the State Office for Nature, Environment and Consumer Affairs (LANUV) of North-Rhine Westphalia.

Table 2.7. Ingredients of the used Western-style diet

	grams %	**kcal %**
Protein	22	20
Carbohydrate	45	40
Fat	20	40
	grams	**kcal**
Casein, 80 mesh	200	800

L-cystine	3	12
Maltodextrin 10	100	400
Fructose	200	800
Sucrose	96	384
Cellulose (BW200)	50	0
Soybean oil	25	225
Primex shortening	135	1215
Lard	20	180
Mineral Mix S10026	10	0
Dicalcium phosphate	13	0
Calcium carbonate	5.5	0
Potassium citrate	16.5	0
Vitamin Mix (V10001)	10	40
Choline bitartrate	2	0
Cholesterol	18	0
FD&C Yellow dye	0.05	0
Total	**904.05**	**4056**

2.2.1.1 Mouse model for NAFLD progression

Eight-week-old male C57Bl/6N mice (Janvier Labs, France) were fed ad libitum with either standard or WD up to 54 weeks. After 3, 6, 12, 18, 24, 30, 36, and 54 weeks, blood and liver tissue samples of 5-7 mice per group were collected for further analysis. In addition, mice were imaged using intravital imaging technique after 3 weeks of standard diet feeding and after 3, 24, and 30 weeks of western-style diet feeding.

2.2.1.2 Td-Tomato mouse model

Eight-week-old Td-tomato mice were fed with WD for 20 weeks and studied using intravital imaging technique. This transgenic mouse line expresses floxed membrane-targeted td-Tomato (*mT*) and membrane-targeted EGFP (*mG*), resulting in red fluorescent signal on all cell membranes prior to Cre-mediated recombination and in green fluorescent signal after the Cre-mediated recombination. The mice were generated by inserting the *mT/mG* tandem dimer construct with CMV enhancer-containing chicken β-actin core promoter (pCA) into the Gt(ROSA)26Sor locus (Fig. 2.1) as reported in detail in Muzumdar et al. (2007). The mouse line can be used as a cell-type specific reporter when bred with a Cre-recombinase carrying mouse line, nevertheless, in this study the red-fluorescent *mT/mG* mouse line without the Cre-mediated recombination was used.

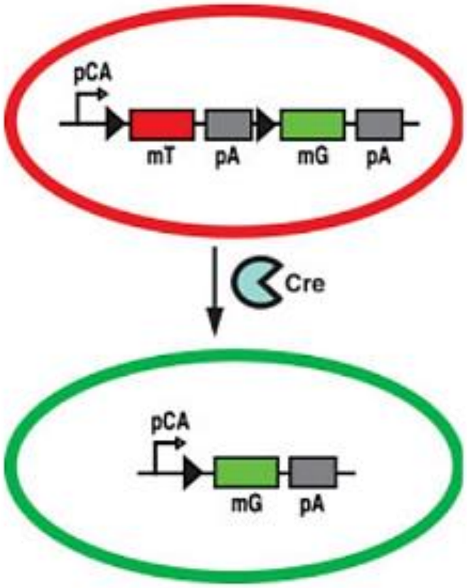

Figure 2.1. mT/mG construct of the Td-Tomato mouse model before and after Cre-mediated recombination. In prior to Cre-mediated recombination, the floxed membrane-targeted td-Tomato (*mT*) and membrane-targeted EGFP (*mG*) are expressed under CMV enhancer-containing chicken β-actin core promoter (pCA), resulting in red fluorescent signal in all cell membranes. After the Cre-mediated recombination of *loxP* alleles, the *mT* sequence is excised. The excision leads to pCA-driven expression of *mG*, which is visualized as green fluorescent signal. Figure from Muzumdar et al., 2007.

2.2.1.3 NAFLD therapeutic intervention

Eight-week-old male C57Bl/6N fed for 18 weeks with *ad libitum* WD were divided into four different treatment groups, n=9-11: (1) vehicle (0.5 % methyl cellulose), given by oral gavage every 12 hours; (2) imipramine 50 mg/kg dissolved in vehicle, given by oral gavage every 12 hours; (3) obeticholic acid (OCA) 30 mg/kg dissolved in vehicle, given by oral gavage every 24 hours; (4) WD was switched to *ad libitum* standard diet. Blood samples were collected from the facial vein before starting the interventions, and the final blood and tissue samples were collected after 8 consequent weeks of interventions.

2.2.2 Sample collection and processing

At the indicated time points, mice were anesthetized by an intraperitoneal injection of ketamine (64 mg/kg), xylazine (7.2 mg/kg) and acepromazine (1.7 mg/kg). After a loss of all reflexes, the skin was dissected and a midline incision was made in the abdominal wall and the liver was exposed. Firstly, bile was collected by cannulating the gallbladder with a tip of a needle of Omnican 100 syringe. The samples were stored at -80 °C for later use. Secondly, blood samples were collected from three positions in mice according to Ghallab et al. (2016): 1) the portal vein representing 75% of the liver inflow, 2) the liver vein representing the liver outflow, and 3) the right heart chamber representing the mixed venous blood. For exposure of the liver vein, the median liver lobe was reflected cranially, whereas the left liver lobe was pushed caudally. The tip of a 30 gauge needle was inserted in the vein and approximately 200 µl of blood was collected. In order to expose the portal vein, the abdominal viscera was gently pulled outside the abdominal cavity while the left and median liver lobes were reflected cranially. The tip of a 30 gauge needle was directed against the direction of the blood flow and approximately 200 µl of blood was collected. In order to collect the heart blood, a 26 gauge needle was passed through the diaphragm and the tip was inserted in the right heart chamber. All blood samples were collected in a syringe pre-coated with disodium EDTA (100 µl/ml blood) to prevent blood coagulation. Subsequently, the blood was centrifuged at 4 °C for 10 min at 16100 x g, after which the plasma was carefully separated and stored at -80 °C until analysis. After the blood collection, the mice were perfused transcardinally with 1x PBS in order to wash out all the excessive blood in the liver. Next, the liver was excised and four different liver samples were collected from defined anatomical position (Fig. 2.2) as following: (1) 1–2 cm^2 specimen from the left liver lobe for paraffin embedding was fixed in 4 % paraformaldehyde (PFA) for 48 hours, after which the sample was processed using the STP 120 Spin Tissue Processor (Thermo Fisher Scientific) as described in table 2.8. Finally, the paraffin blocks were prepared using the EC 350 modular tissue embedding center (Microm), and 4 µm-thick tissue sections were cut using a sliding microtome (Microm); (2) 1-2 cm^2 specimen from the left liver lobe for cryo sample preparation was first fixed in 4 % paraformaldehyde (PFA) for 48 hours, and then dehydrated in 30 % sucrose for 48 hours. Afterwards, the tissue was embedded in NEG-50 media, frozen in 2-methylbutane, and stored at -80 °C until further use; (3) 1-2 cm^2 specimen from the median lobe was snap-frozen in liquid nitrogen for the examination with matrix-assisted laser desorption/ionization mass spectrometry imaging (MALDI-MSI); (4) the remaining liver tissue was flattened with a cooled clamp, crushed with a pestle in liquid nitrogen, and stored at -80 °C until analysis.

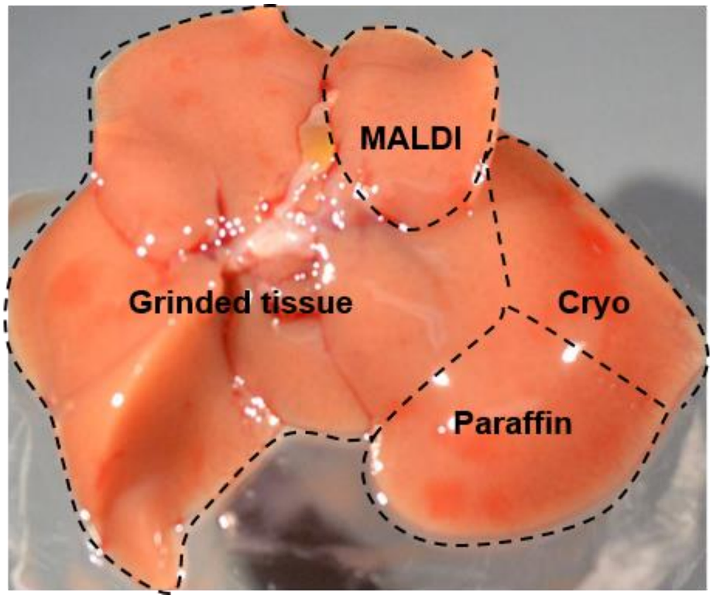

Figure 2.2. Sample collection from defined anatomical position in the mouse liver. The left liver lobe was divided into two pieces for preparation of cryo and paraffin samples. A piece from the median lobe was collected and snap-frozen for future MALDI-MSI imaging. The rest of the liver was shock-frozen by freeze-clamping and milling in liquid nitrogen.

Table 2.8. Paraffin embedding program of the liver tissue

Solution	Time (min)
70 % Ethanol	30
70 % Ethanol	60
90 % Ethanol	30
90 % Ethanol	30
99 % Ethanol	30
99 % Ethanol	35
99 % Ethanol	60
Xylene	30
Xylene	35
Xylene	60
Paraffin	80
Paraffin	105

2.2.3 Macrophage depletion

Macrophage depletion was performed by intravenous injection of clodronate-containing liposomes (Clodronate Liposomes) into mice fed for 24 weeks with WD, which leads to clodronate phagocytosis by macrophages, and hence to macrophage depletion (Wang et al., 2009). Two days after clodronate administration, mice were imaged with intravital imaging technique to reveal the CLF transport as described later (section 2.2.7).

2.2.4 Human NAFLD tissue samples

Human paraffin-embedded NAFLD liver tissue samples were acquired from Medical University of Vienna. The samples were divided into four groups according to the patient fibrosis stage: fibrosis stage 0 (F0; N=7), fibrosis stage 1 (F1; N=11), fibrosis stage 2 (F2; N=7), fibrosis stage 3 (F3; N=9), fibrosis stage 4 (F4; N=6).

2.2.5 Histopathology

2.2.5.1 Hematoxylin & Eosin staining

Hematoxylin & eosin (H&E) staining was performed for basic histopathological examination. Four µm-thick formalin-fixed, paraffin embedded (FFPE) liver tissue sections were stained using standard protocol. First, the samples were deparaffinized in Roti-Histol and rehydrated in descending ethanol series (100 %, 90 %, 80 %, 70 %, 50 %, 30 %, distilled H_2O). Next, the samples were incubated for 5 minutes in Mayer’s hematoxylin for nuclei staining, and then placed under a running tap water for 15 minutes. Subsequently, the samples were incubated for 3 minutes in 1 % eosin to stain the cytoplasm, after which the section were rehydrated in an ascending ethanol series (70 %, 80 %, 90 % and 100 %). Lastly, the samples were incubated 3 minutes in Roti-Histol and mounted with Entellan for preservation.

2.2.5.2 Sirius Red staining

In order to evaluate the collagen accumulation in the liver tissue, Picosirius Red staining was performed using a commercially available kit according to the manufacturer instructions (Polyscience Europe GmbH). Briefly, four µm-thick FFPE samples were first deparaffinized in Roti-Histol and rehydrated in descending ethanol series (100 %, 90 %, 80 %, 70 %, 50 %, 30 %, distilled H_2O). Subsequently, the samples were incubated for 2 minutes in phosphomolybdic acid, followed by 90 second rinsing in distilled H_2O. Next, the samples were stained in Picosirius Red solution for 60 minutes and afterwards rinsed in distilled H_2O for 2 minutes. Subsequently, the samples were incubated in 0.01 % HCl for 2 minutes and immediately dehydrated in ascending ethanol gradient (70 %, 80 %, 90 % and 100 %). Finally, the samples were incubated in Roti-Histol for 3 minutes and mounted with Entellan for preservation.

2.2.6 Immunohistochemistry

2.2.6.1 Immunoperoxidase staining

Immunoperoxidase staining was performed on 4 µm-thick FFPE sections either manually or automatically using Discovery Ultra Automated Slide Preparation System (Roche). Antibodies, antibody dilutions, and chosen staining techniques are listed in table 2.8. All stained slides were scanned with Axio Scan.Z1 (Zeiss).

2.2.6.1.1 Automatic staining procedure

For automatic single-antibody staining procedure, the steps were conducted with Discovery Ultra Automated Slide Preparation System (Roche). In principal, EZ prep solution was used for deparaffinization of the slides and the antigen retrieval was performed in CC1 buffer (pH 7.4). Depending on the performed staining, either ChromoMap DAB Kit, Yellow Kit or Purple Kit was used and 100 µl of appropriately diluted primary antibody (Table 2.8) was manually added on each slide. The secondary antibodies were automatically added by the system. For counter-staining of the nuclei in blue, Hematoxylin II and Bluing Reagent were used. After the counter-staining step, the samples were manually washed in pre-warmed tap water with a drop of detergent. Subsequently, the samples were rehydrated in ascending ethanol series (30 %, 50 %, 70 %, 80 %, 90 % and 100 %), followed by incubation in Roti-Histol for 6 minutes. Lastly, the samples were mounted with Entellan.

2.2.6.1.2 α-SMA staining

Alpha-smooth muscle actin (α-SMA) staining was conducted manually on liver paraffin sections. First, the samples were first deparaffinized in Roti-Histol and rehydrated in descending ethanol series (100 %, 90 %, 80 %, 70 %, 50 %, 30 %, distilled H_2O). Subsequently, the samples were boiled in Tris-EDTA buffer (pH 9.0) in a microwave for 14 minutes for antigen retrieval, followed by 30 minutes of cooling down back to room temperature and 5 minutes washing in 1x TBS. In order to prevent an interference with antigen detection, endogenous peroxidases were blocked by incubating the samples in Peroxidase Block (DakoCytomation) for 6 minutes. Afterwards, the sections were first washed in TBS, followed by a blocking of unspecific binding with Rodent Block solution (Mouse on mouse Polymer IHC kit, Abcam) for 30 minutes. Next, appropriately diluted primary antibody (Table 2.8) was added for 30 minutes. After the primary antibody incubation, the slides were washed with TBS-T and subsequently incubated in Mouse on Mouse HRP Polymer (Mouse on mouse Polymer IHC kit, Abcam) for 30 minutes in dark. Afterwards, the slides were washed with TBS-T and TBS, subsequently. Finally, the antibody binding was visualized by incubation in DAB staining solution (Vector Laboratories). The color development was controlled by eye and stopped by washing the samples in TBS. In order to see the nuclei, a counter-staining with Mayer's hematoxylin was performed for 90 seconds, followed by 10 minute rinsing under running tap water. Lastly, the samples were rehydrated in ascending ethanol series (30 %, 50 %, 70 %, 80 %, 90 % and 100 %), followed by incubation in Roti-Histol for 6 minutes and mounting with with Entellan.

2.2.6.1.3 F4/80 and Cyp2e1 automated co-staining

For co-staining of F4/80 andCyp2e1 co-staining, the liver paraffin sections were first deparaffinized in Discovery Ultra Automated Slide Preparation System as explained above. Primary F4/80 antibody was added manually without prior antigen retrieval step, followed by automatic application of an appropriate secondary antibody (Table 2.8). Next, the slides were warmed up to 95 °C for Cyp2e1 antigen retrieval in CC1 buffer. Cyp2e1 antibody was manually added, followed by automatic incubation with an appropriate secondary antibody (Table 2.9), and counterstaining with Hematoxylin II and Bluing Reagent. Lastly, the samples were rehydrated in ascending ethanol series (30 %, 50 %, 70 %, 80 %, 90 % and 100 %), followed by incubation in Roti-Histol for 6 minutes and mounting with Entellan.

Table 2.9. Primary and secondary antibodies used in immunoperoxidase staining

Target	Primary antibody		Secondary antibody		Manual/
	Antibody	**Concentration**	**Antibody**	**Concentration**	**automatic**
α-isotype of actin in hepatic stellate cells	Mouse anti-human α-SMA	1:100	Mouse on Mouse Polymer IHC Kit		Manual
Aminopeptidase N in bile canaliculi	Rabbit anti-mouse CD13	1:12000	Discovery UltraMap anti-Rb HRP	Automatic	Automatic

Cell proliferation antigen	Rabbit anti-mouse Ki67	1:100	Discovery UltraMap anti-Rb HRP	Automatic	Automatic
Cytochrome P450 2E1	Rabbit anti-mouse CYP2E1	1:100	Discovery UltraMap anti-Rb AP	Automatic	Automatic
C-terminus of BSEP	Rabbit anti-human BSEP	1:1000	Discovery UltraMap anti-Rb HRP	Automatic	Automatic
C-terminus of NTCP	Rabbit anti-mouse NTCP	1:3000	Discovery UltraMap anti-Rb HRP	Automatic	Automatic
Mature bile ductules	Rabbit anti-mouse CK19	1:500	Discovery UltraMap anti-Rb HRP	Automatic	Automatic
Leukocyte common antigen	Rat anti-mouse CD45	1:400	Discovery UltraMap anti-Rt HRP	Automatic	Automatic
Macrophages	Rat anti-mouse F4/80	1:50	Discovery UltraMap anti-Rt HRP	Automatic	Automatic
Hepatic stellate cells	Rabbit anti-mouse Desmin	1:400	Discovery UltraMap anti-Rb HRP	Automatic	Automatic

2.2.6.2 Immunofluorescence staining and 3D reconstruction

2.2.6.2.1 TUNEL immunofluorescence staining

For TUNEL staining of liver samples, 6 µm-thick cryo sections were cut with LEICA CM3050 S cryostat-microtome (Leica). First, the samples were fixed in 3 % PFA for 5 minutes, followed by washing in 1x PBS and incubation in 95 % EtOH plus acetic acid solution. Subsequently, the slides were washed with 1x PBS and fixed for 10 minutes in 3 % methanol-free PFA. The washing step and PFA fixation was repeated, followed by one more washing in 1x PBS. Next, the staining was continued with Dead End Fluorometric TUNEL kit (Promega) according to the manufacturer's protocol. Briefly, the slides were incubated in equilibrium buffer for 10 minutes, followed by incubation with TdT reaction mix for 60 minutes in 37 °C in a humid chamber. Afterwards, the reaction was stopped by incubation in SSC buffer. Subsequently, the slides were washed first in PBS-T and then in 1x PBS. Lastly, the slides were shortly dipped in ddH_2O to remove the salts and mounted with FluorSave^{TM} mounting medium (Merck). For image acquisition, the slides were scanned with Axio Scan.Z1 (Zeiss).

For 3D reconstructions of stained liver tissue samples, 100 µm-thick cryo samples were sectioned with LEICA CM3050 S cryostat-microtome (Leica) and directly washed with 1x PBS four times for 15 minutes. Next, the samples were permeabilized with 1x PBS-T for 1 h. Subsequently, unspecific binding sites were blocked with PBS-T containing 1% BSA and 10 % donkey serum for 2 hours at 37 °C and then at 4 °C overnight. On the next day, the sections were incubated with the primary antibodies (Table 2.10) appropriately diluted in PBS-T containing 1 % BSA at 4 °C for 2–3 days. Next, the samples were washed in PBS-T and incubated for 2-3 days at 4 °C with appropriate secondary antibodies and diamidino-2-phenylindole (DAPI) (Table 2.10) diluted in PBS-T containing 0.5 % BSA and 5 % donkey serum. Afterwards, the samples were washed with 1x PBS and incubated with Bodipy^{TM} or Nile Red for 2 hours. Lastly, the sections were washed with 1x PBS and mounted with FluorSave^{TM} Reagent. For analysis, z-stacks were acquired using a laser scanning microscope (Olympus). The 3D reconstruction was performed with the Imaris 9.5.1 software (Bitplane).

Table 2.10. Primary and secondary antibodies used in immunofluorescence staining

Target	Primary antibody		Secondary antibody	
	Antibody	**Concentration**	**Antibody**	**Concentration**
Aminopeptidase N in bile canaliculi	Rat anti-mouse CD13	1:100	Cy™5 AffiniPure Donkey Anti-Rat IgG (H+L)	1:200
β-Catenin aa. 571-781	Mouse anti-β-Catenin	1:100	Cy™2 AffiniPure Donkey Anti-Mouse IgG (H+L)	1:200
Macrophages	Rat anti-mouse F4/80	1:25	Cy™5 AffiniPure Donkey Anti-Rat IgG (H+L)	1:200
Midzonal/periportal hepatocytes	Goat anti-liver Arginase	1:100	Cy™5 AffiniPure Donkey Anti-Goat IgG (H+L)	1:200
Lipids	Bodipy™ 495/503	2 µg/ml	—	
Lipids	Nile Red (Cy3-conjugated)	2 µg/ml	—	

2.2.7 Intravital imaging

Intravital imaging of intact mouse livers was performed by using a custom-modified inverted LSM MP7 (Zeiss) equipped with an LD C-Apochromat 40x 1.1. water immersion objective, as previously described by Reif et al. (2017) and Ghallab et al. (2019a). First, the mice were anesthetized by an i.p. injection of ketamine (64 mg/kg), xylazine (7.2 mg/kg) and acepromazine (1.7 mg/kg). After loss of reflexes, the left liver lobe was exposed by making a small opening in the abdominal wall, caudal to the sternum. To minimize the influence of breathing on the liver, the coronary ligament connecting the liver and the diaphragm was cut. The exposed liver lobe was placed on 0.17 mm-thick cover slip (Logitech), and the mouse was placed on a lateral position, and moved onto the microscope stage (Figure 4.2). In order to avoid drying of the exposed liver lobe, it was covered with saline-moistened gauze. The fluorescent dyes (Table 2.11) were injected via tail vein before starting the recording, except cholyl-lysyl-fluorescein (CLF), which was administered via tail vein catheter during the recording process. While recording, the mouse was kept anesthetized via isoflurane administration, and the mouse was kept at ambient temperature of 36 °C.

Table 2.11. Fluorescent marker dyes for intravital imaging

Fluorescent marker dye	Marker for	Dose (mg/kg)	Company
Cholyl-lysyl-fluorescein (CLF)	Bile acid analogue	1 in 1x PBS	BD Biosciences
Hoechst 33258	Nuclei	5 in 1x PBS	Thermo Fisher Scientific
Bodipy™ 493/503	Fatty acids	0.013	Life Technologies
Tetramethylrhodamine ethyl ester (TMRE)	Mitochondrial membrane potential	0.96 in methanol:PBS (1:1)	Thermo Fisher Scientific

2.2.8 Quantitative analysis of the canalicular network

For quantitative analysis of bile canalicular volume and number of bile canalicular segments of CD13-stained 3D samples, five to ten 100 µm-thick z-stacks per mouse were analyzed with IMARIS surface analysis at 1 µm z-step size, at 400x magnification.

2.2.9 RNA isolation and cDNA synthesis

2.2.9.1 RNA isolation

RNA was isolated from milled liver tissue using QIAzol lysis reagent (Qiagen) and phenol/chloroform method. First, 1 ml of QIAzol lysis reagent was added onto liver tissue samples and subsequently sonicated for 30 seconds on ice. Next, 0.2 ml chloroform was added, the samples were vortexed for 10 seconds and centrifuged at 12000 x g for 15 minutes. The centrifugation created three phases: an upper aqueous phase containing the RNA, an interphase, and a lower organic phase. The RNA phase was transferred into new tube and mixed gently with 500 µl isopropanol. Next, the samples were centrifuged at 12000 x g for 10 minutes, after which the supernatant was carefully discarded and the remaining RNA pellet was mixed with 100 % ethanol, followed by centrifugation at 12000 x g for 5 minutes. The ethanol washing steps were repeated with 80 % and 75 % ethanol, and after the removal of final supernatant, the RNA pellet was air-dried and dissolved in DEPC-treated water. RNA concentration and quality were measured using Nanodrop 2000 spectrometer (Thermo Fisher Scientific).

2.2.9.2 cDNA synthesis

Complementary cDNA synthesis was conducted from 2 µg of isolated RNA. The transcription was performed in TGRADIENT Biometra thermocycler (Analytik Jena) using High Capacity cDNA Reverse Transcription kit (Applied Biosystems). The reaction mixture used in the cDNA synthesis is indicated in table 2.12. The qPCR program was set for initial incubation at 25 °C for 10 minutes, followed by reverse transcription phase at 37 °C for 120 minutes, inactivation phase at 85 °C for 5 seconds, and lastly the temperature was decreased to 4 °C. After completion of the synthesis, the cDNA was diluted with DEPC-treated water to 10 ng/µl and stored at -20 °C until further use.

Table 2.12. cDNA reaction mixture composition

Master mix	
10x RT-buffer	2 µl
25x dNTP	0.8 µl
Random primer	2 µl
Reverse transcriptase	1 µl
DEPC H_2O	4.2 µl
Sum volume 1	**10 µl**
RNA	2 µg
H_2O up to	10 µl
Sum volume 2	**10 µl**
Final volume	**20 µl**

2.2.10 Quantitative real-time PCR (qRT-PCR)

In order to determine the mRNA expression levels of the target genes, quantitative real-time PCR was conducted. Used TaqMan primer probes (Applied Biosystems) are listed in table 2.13. For PCR reaction, 25 ng of cDNA sample was mixed with qRT-PCR reaction mix including the primer probes and TaqMan Universal Master Mix with UNG (Applied Biosystems) according to table 2.14 and run on the plate in duplicates. Conditions for the PCR program are listed in table 2.15. The PCR products of each sample were analyzed with 7500 Real-Rime PCR System software and normalized to mouse glyceraldehyde-3-phosphate dehydrogenase (GAPDH) mRNA expression. For calculations of relative gene expression, $2^{-\Delta\Delta Ct}$ method was used as described before in Livak & Schmittgen (2001).

Table 2.13. TaqMan gene expression assays (Applied Biosystems, Foster City, USA)

TaqMan assay	Assay catalog no.
Abcb11	Mm00445168_m1
Abcc2	Mm00496899_m1
Abcc3	Mm00551550_m1
Abcc4	Mm01226381_m1
Cyp7a1	Mm01164862_m1
IL12b	Mm00439620_m1
IL6	Mm01193538_m1
Mouse GAPDH	4352932E
Slc10a1	Mm00441421_m1
Slco1b2	Mm00451510_m1
Tnf	Mm00443260_g1

Table 2.14. qRPT-PCR reaction mixture composition

Kit	µl per cDNA sample
TaqMan Universal Master Mix	10
DEPC H_2O	6.5
TaqMan primer probe	1

Table 2.15. qRT-PCR program setup

Stage	Temperature (°C)	Time	Repetition
1	50	2 min	1
2	95	10 min	1
3	94 60 72	15 s 30 s 35 s	40
4	95 60 95 60	15 s 20 s 15 s 15 s	1

2.2.11 Biochemical analysis

The liver function tests were performed by using Piccolo Xpress chemistry analyzer (Abaxis) and General Chemistry 13 panel discs (Abaxis). The panel contains dry reagents for the determination of 13 different substances, including alanine-aminotransferase (ALT), aspartate-aminotransferase (AST) and alkaline phosphatase (ALP). For analysis, the samples were diluted 1:1 with 1x PBS, and 100 µl of the dilution mix was pipetted into the sample chamber of the disc. As the samples reached the dry reagents, reactions took place and the signals were accordingly detected by the system.

2.2.12 MALDI-MSI

Analysis of taurocholic acid (TCA) in liver tissue with MALDI-MSI was performed as previously described by Ghallab et al. (2019a) and Sezgin et al. (2018). Briefly, two serial liver sections of every sample were prepared: one for MALDI-MSI analysis for TCA and one for arginase immunohistochemical staining. Thus, the MALDI signal was superimposed onto the adjacent arginase-stained tissue section in order to localize the TCA accumulation in the liver tissue.

2.2.13 Bile acid assay

Bile acids in liver tissue, bile and blood were determined according to a method described previously in Ghallab et al. (2019a), based on liquid chromatography–negative electrospray ionization–tandem mass spectrometry (LC-ESI-MS/MS) method.

2.2.14 Western Blot analysis

2.2.14.1 Protein extraction

All the steps of protein extraction for western blot analysis were performed on ice. First, milled liver tissue was incubated with 150 µl of NP-40 lysis solution for 10 minutes. Subsequently, the samples were centrifuged at 13000 x g at 4 °C and the resulting supernatant was collected into a new tube. Next, the protein concentration was determined using a colorimetric assay based on Bradford method as described in Kruger (2009). Based on the measured concentrations, the samples were further diluted into 6 µg/ml in Laemmli-Sample buffer plus β-mercaptoethanol solution. Lastly, the samples were heated for 5 minutes in 95 °C and stored in -80 °C for until further use.

2.2.14.2 Sodium dodecyl sulfate-polyacrylamide gel electrophoresis (SDS-PAGE)

In order to separate the proteins from the liver tissue samples according to their size, sodium dodecyl sulfate-polyacrylamide gel electrophoresis (SDS-PAGE) was performed. Stacking gel and 10 % polyacrylamide separating gel were prepared as indicated in table 2.16. After polymerization of the gels, they were fixed into the gel chambers filled with the running buffer. In prior to the sample loading, the samples were mixed with Laemmli-Sample buffer plus β-mercaptoethanol solution (1:20) and denatured at 95 °C for 5 minutes. Subsequently, the samples and the protein standard (Invitrogen) were carefully loaded into the gel chambers. The samples were run at the current of 120 mA for 2 to 3 hours, leading to a separation of denatured proteins on the gel according to their molecular size.

Table 2.16. Western blot separation and stacking gel composition

	Stacking gel (pH 6.8)	Separation gel (pH 8.8)
H_2O	3.1 ml	4.0 ml
Tris 1.5M	1.25 ml	2.5 ml
Acryl amide	0.5 ml	3.3 ml
SDS 10 %	50 µl	100 µl
APS	25 µl	100 µl
TEMED	7.5 ml	7.5 ml

2.2.14.3 Protein transfer

In order to eventually detect the protein bands, they were transferred from the stacking gel into Immobilon PVDF membrane. First, two Whatman papers (Sigma-Aldrich) were soaked in transfer buffer and the membrane was activated by incubating it first briefly in methanol, then in distilled H_2O and lastly in the transfer buffer for 5 minutes. Next, a soaked Whatman paper was placed into the blotting chamber, followed by an insertion of the membrane on top of it. Furthermore, the construct was covered by the transfer buffer. Next, the stacking gel and another soaked Whatman paper were placed on top of the membrane and the transfer was performed at 80 mA for 1.5 hours, resulting in protein transfer from the stacking gel onto the PVDF membrane. After the transfer, the membrane was stained with Ponceau S solution (Sigma-Aldrich) to later visualize the protein bands, and afterwards washed in TBS-T and blocked in 5 % BSA plus TBS-T solution for 1 hour in order to prevent unspecific antibody binding.

2.2.14.4 Protein detection

For protein detection, the membrane was incubated overnight in the primary antibodies, listed in table 2.17. The next day, the membrane was first washed with TBS-T and then incubated one hour with horseradish peroxidase (HRP)-linked secondary antibody as indicated in table 2.16. Subsequently, the membrane was washed in TBS-T and the chemiluminescence was detected by using the enhanced chemiluminescense (ECL) Chemiluminescence Kit (GE Healthcare) and the Fusion Fx7 imaging system (Vilber Lourmat).

Table 2.17. Antibodies used for Western blotting

Primary antibody	Secondary antibody
anti-Cleaved Caspase-3	HRP-linked anti-rabbit immunoglobulin G
anti-GAPDH	HRP-linked anti-mouse immunoglobulin G
anti-MLKL	HRP-linked anti-rabbit immunoglobulin G

2.2.15 Statistical analysis

Statistical analysis was performed with GraphPad Prism software version 8.4.3. In normally distributed datasets, one-way ANOVA and two-way ANOVA were used with Dunnett's multiple comparison test. In case of unequal distribution, Wilcoxon matched-pairs signed rank test was conducted. $P<0.05$ was considered as statistically significant.

3 RESULTS

3.1 Establishment of a mouse model of NAFLD progression

The goal of this experiment was to establish a mouse model that recapitulates various stages of NAFLD progression, and that can be used in follow-up experiments to study the mechanisms driving the progression of NAFLD to NASH. To accomplish this, male C57BL/6N mice were fed either a standard diet (SD) or a calorie-rich western-style diet (WD) up to 54 weeks. Blood, bile and liver tissue samples were collected time-dependently (Fig. 3.1A). Grossly, the liver tissue appeared paler from three weeks onwards (Fig. 3.1B). Bodyweight of the mice increased time-dependently both in WD- and in SD-fed mice. However, the liver-to-bodyweight ratio increased only in the WD-fed mice, particularly from week 18 onwards (Fig. 3.1C). At week 54, most of the WD-fed mice (>80 %) developed macroscopically visible tumor nodules (Fig. 3.1D).

H&E staining showed time-dependently increasing number and size of lipid droplets (Fig. 3.2A). Co-staining of lipid droplets and arginase, a zonation marker for periportal and midzonal hepatocytes, demonstrated that the formation of large lipid droplets initially occurred in the midzonal and periportal but not in the pericentral zone (Fig. 3.2B). Nevertheless, it should be considered that sample fixation and washing steps during histological staining might lead to an alteration of lipid droplet size and even to a complete lipid droplet washout. To overcome this issue, the size and the zonation of lipid droplets were investigated intravitally using two-photon microscopy. In line with the histological analysis, intravital imaging at 9 weeks of WD feeding showed an accumulation of large lipid droplets in the periportal and midzonal hepatocytes and smaller lipid droplets in the pericentral hepatocytes (Fig. 3.2C).

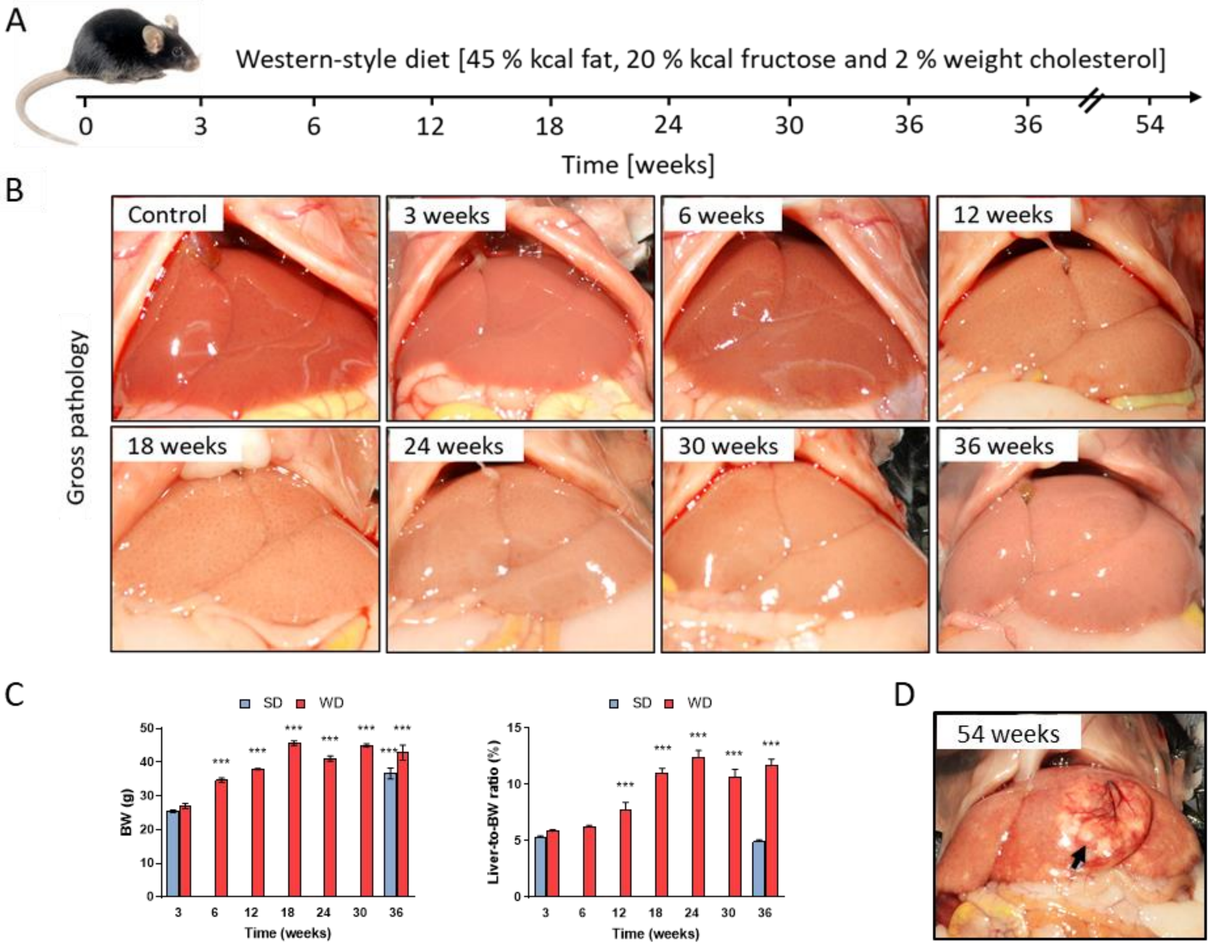

Figure 3.1. Mouse model of NAFLD progression. A. Experimental design. **B.** Gross pathology showing discoloration of the liver after feeding on WD. Control: 3 weeks of SD feeding. **C**. Bodyweight and liver-to-bodyweight ratio increase time-dependently during NAFLD progression. The results are presented as means ± SEM of at least 5 biological replicates. ***P<0.001, compared to 3 weeks of SD feeding. **D**. Macroscopically visible tumor nodule (arrow) after 54 weeks of WD feeding. SD: standard diet; WD: western-style diet; BW: bodyweight.

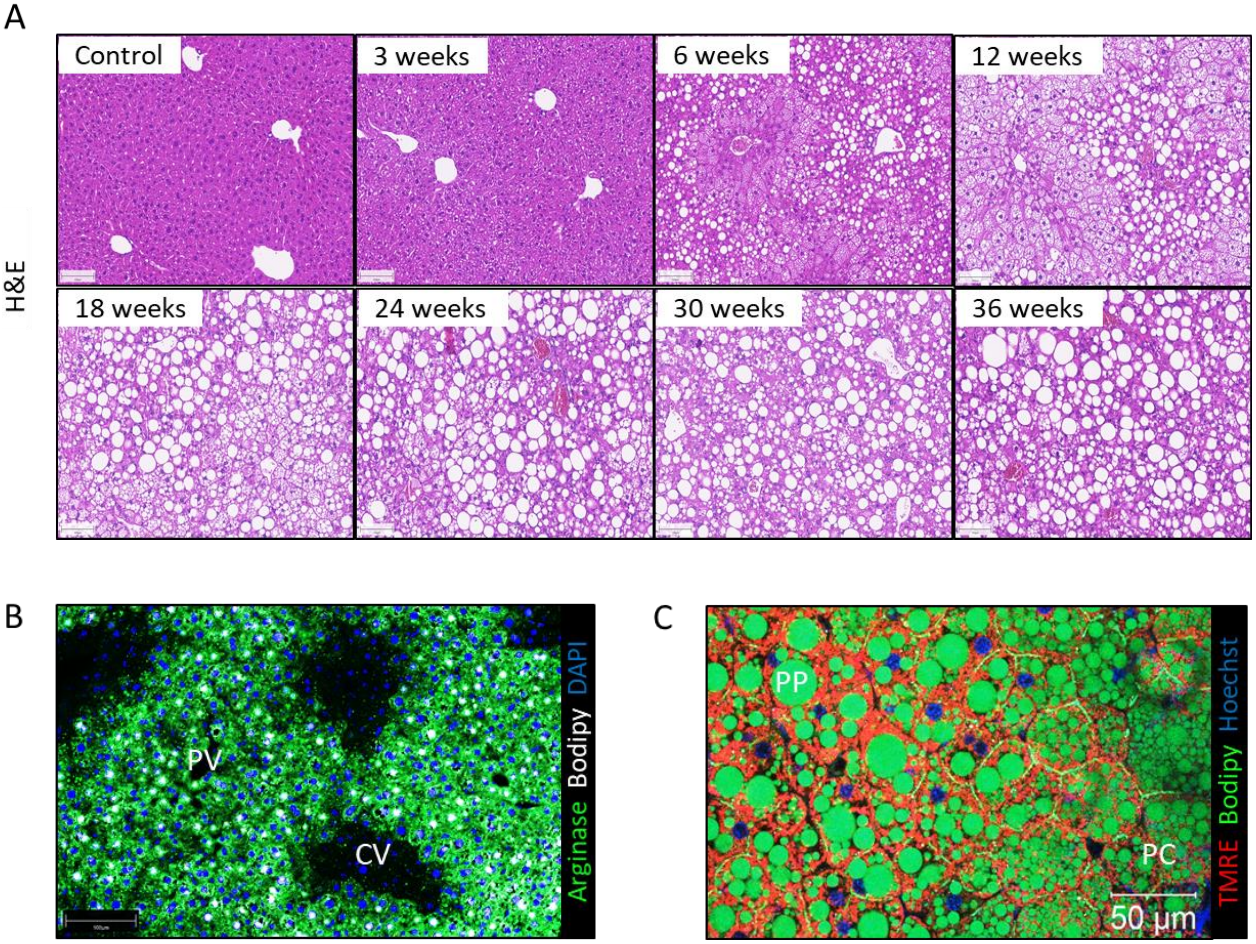

Figure 3.2. Lipid droplet accumulation in the liver of WD-fed mice. A. H&E staining of liver paraffin sections shows a time-dependent growth and accumulation of lipid droplets inside hepatocytes. Scale bars: 100 µm. H&E: hematoxylin and eosin staining; Control: 3 weeks of SD feeding. **B**. Co-staining of arginase and Bodipy after 3 weeks of WD feeding shows that lipid droplets first occur in the midzonal/periportal but not in the pericentral zone of the liver lobule. Scale bars: 100 µm. PV: portal vein; CV: central vein; arginase: periportal/midzonal hepatocyte marker; Bodipy: lipid droplets; DAPI: nuclei. **C**. Two-photon intravital imaging after 9 weeks of WD feeding shows the total number and the real size of lipid droplets inside hepatocytes. TMRE intensity shows the zonation, confirming that the large size lipid droplets occur in the midzonal/periportal zone. Scale bars: 50 µm. PP: midzonal/periportal zone; PC: pericentral zone; TMRE: tetramethylrhodamine ethyl ester; mitochondrial membrane potential; Bodipy: lipid droplets; Hoechst: nuclei.

An important characteristics of NASH is the infiltration of inflammatory cells in the liver. To clarify if the present NAFLD mouse model recapitulates that feature, liver paraffin sections were first immunostained against CD45 that indicates the total number of leukocytes. The staining showed a heavy leukocyte infiltration, starting time-dependently from week 12 of WD feeding onwards (Fig. 3.3A). Interestingly, the leukocytes formed crown-like structures around steatotic hepatocytes from 18 weeks of WD feeding onwards. To further investigate the subtype of the leukocytes that accumulate in the liver, tissue sections were stained against F4/80, a marker of macrophages. Most of the CD45 positive leukocytes, and especially the crown-like structure forming cells, were identified as macrophages (Fig. 3.3B). In addition, the specific location of the macrophages in the liver lobule was studied by co-staining F4/80 with Cyp2e1, a pericentral hepatocyte marker. The staining revealed that the infiltrating and crown-like structure forming macrophages were mainly located in the midzonal and periportal compartment of the liver lobule (Fig. 3.3C).

In order to better understand the proximity of lipid-filled hepatocytes and macrophages, co-staining of macrophages and lipid droplets was performed in liver tissue sections after 30 weeks feeding on WD. Three-dimensional reconstructions showed that macrophages enclose the steatotic hepatocytes (Fig. 3.4A). Interestingly, in some macrophage crowns, no hepatocyte nuclei or cytoplasm were visible, which suggests hepatocyte death. In that case, macrophages exclusively enclose the remaining lipid droplet (Fig. 3.4B). In order to further clarify if the observed lipid and macrophage accumulation leads to an increasing cell death, liver tissue sections were stained with TUNEL, a marker of cell death. In coincidence with inflammatory cell infiltration, the degree of cell death started increasing at week 12 of WD feeding and became very evident from week 18 on (Fig. 3.5A). In order to further investigate the exact mode of cell death, Western blot analysis was performed using antibodies against cleaved Caspase-3 (apoptosis marker) and MLKL (necroptosis marker). Interestingly, the western blots showed that apoptosis was not activated in any tested time periods after WD feeding, indicated as a lacking expression of cleaved Caspase-3 (Fig. 3.5B). In contrast, a time-dependent increase in expression of the necroptosis marker MLKL was detected (Fig. 3.5B). Furthermore, Ki67 staining of liver paraffin sections was performed to investigate if the observed cell death was replaced by cell proliferation. Consequently, from week 12 of WD feeding onwards the cell proliferation increased similarly as the necroptosis rate (Fig. 3.5C).

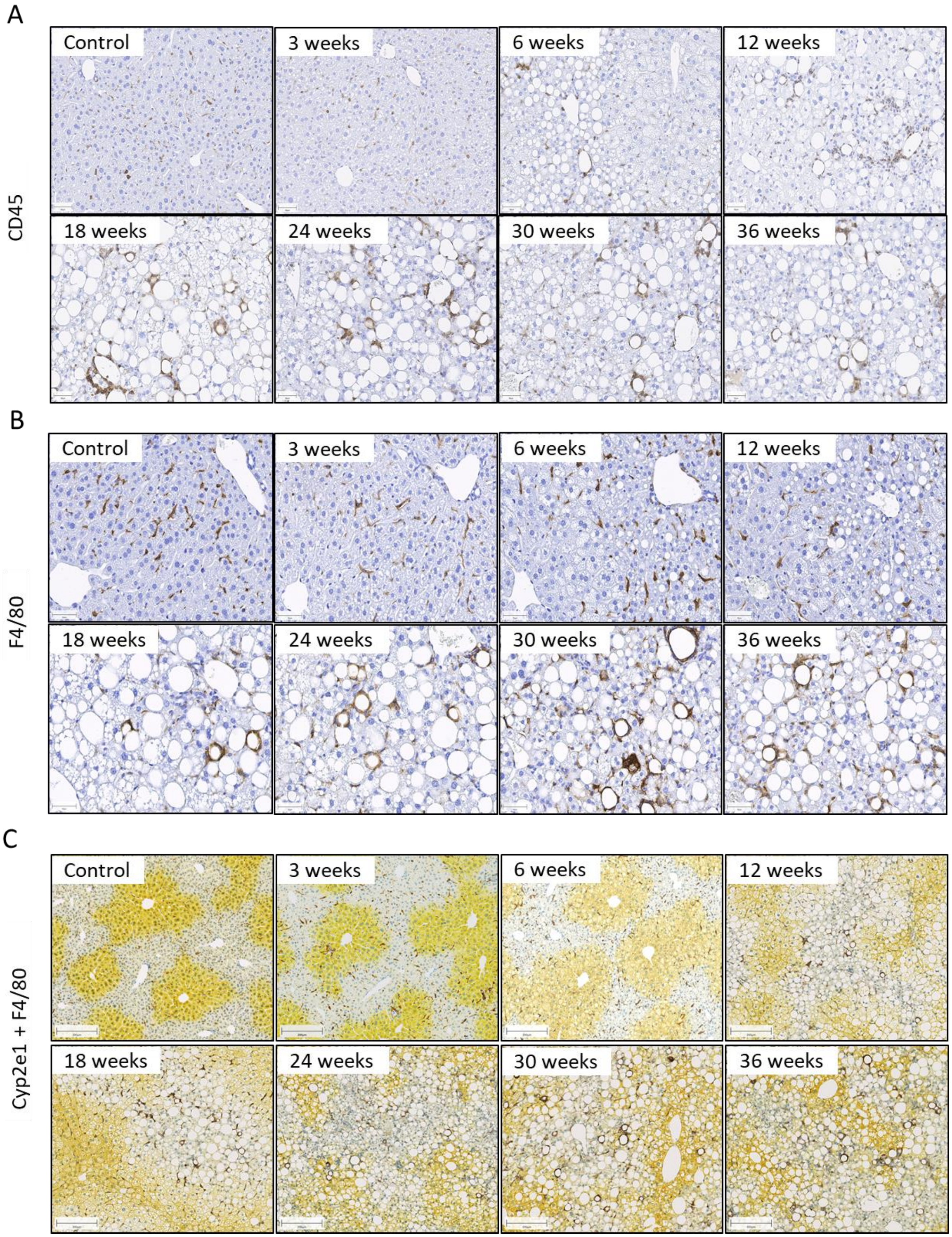

Figure 3.3. Macrophages form crown-like structures surrounding the large lipid droplets. A. CD45 staining of WD-livers showing time-dependently increasing infiltration of leukocytes in the liver tissue, which form crown-like structures around steatotic hepatocytes at week 18 and later time periods. **B**. F4/80 staining identifying the crown-like-structure forming CD45-positive cells as macrophages. **C.** Co-staining of F4/80 with Cyp2e1 showing macrophage crown-like structures mainly in the midzonal and periportal compartment of the liver lobule. Scale bars: 50 µm (A, B), 200 µm (C). Control: 3 weeks of SD feeding.

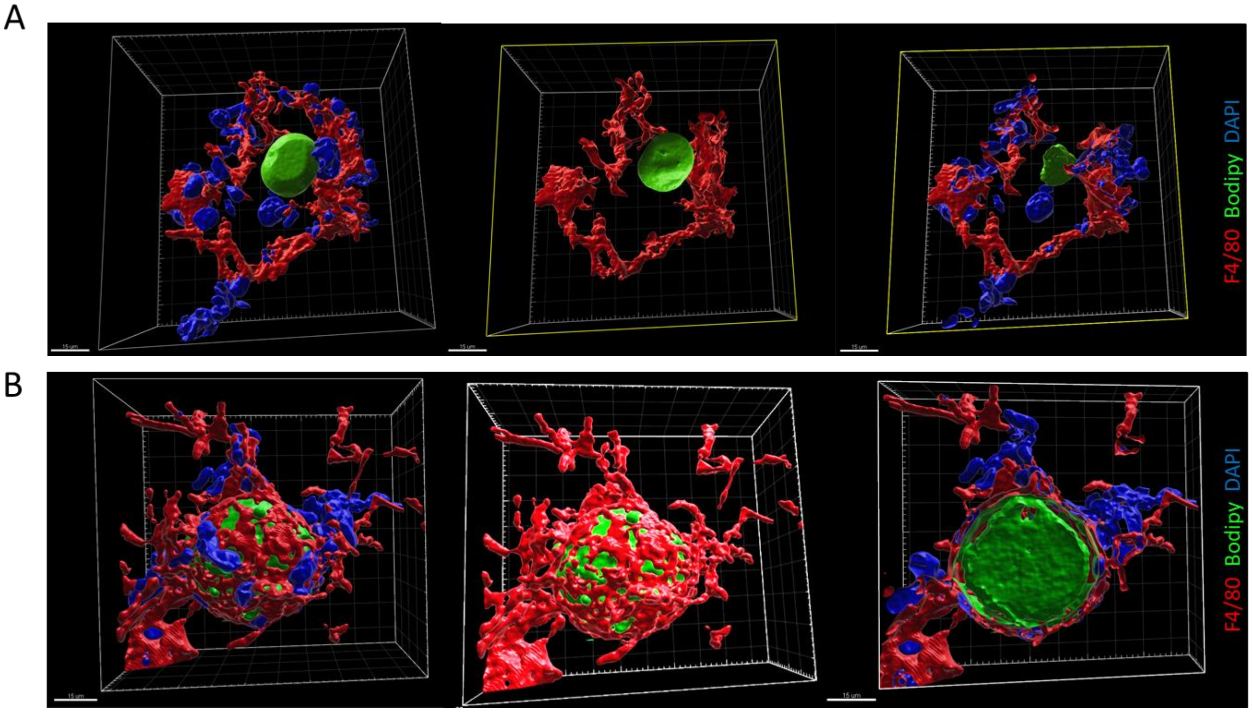

Figure 3.4. Three-dimensional reconstruction of hepatocytes and macrophages. A. Steatotic living hepatocyte become surrounded by macrophages after 30 weeks of WD feeding. **B.** Exclusive macrophage accumulation around dead, lipid-filled hepatocyte. F4/80: macrophages; Bodipy: lipid droplets; DAPI: nuclei. Scale bars: 15 µm.

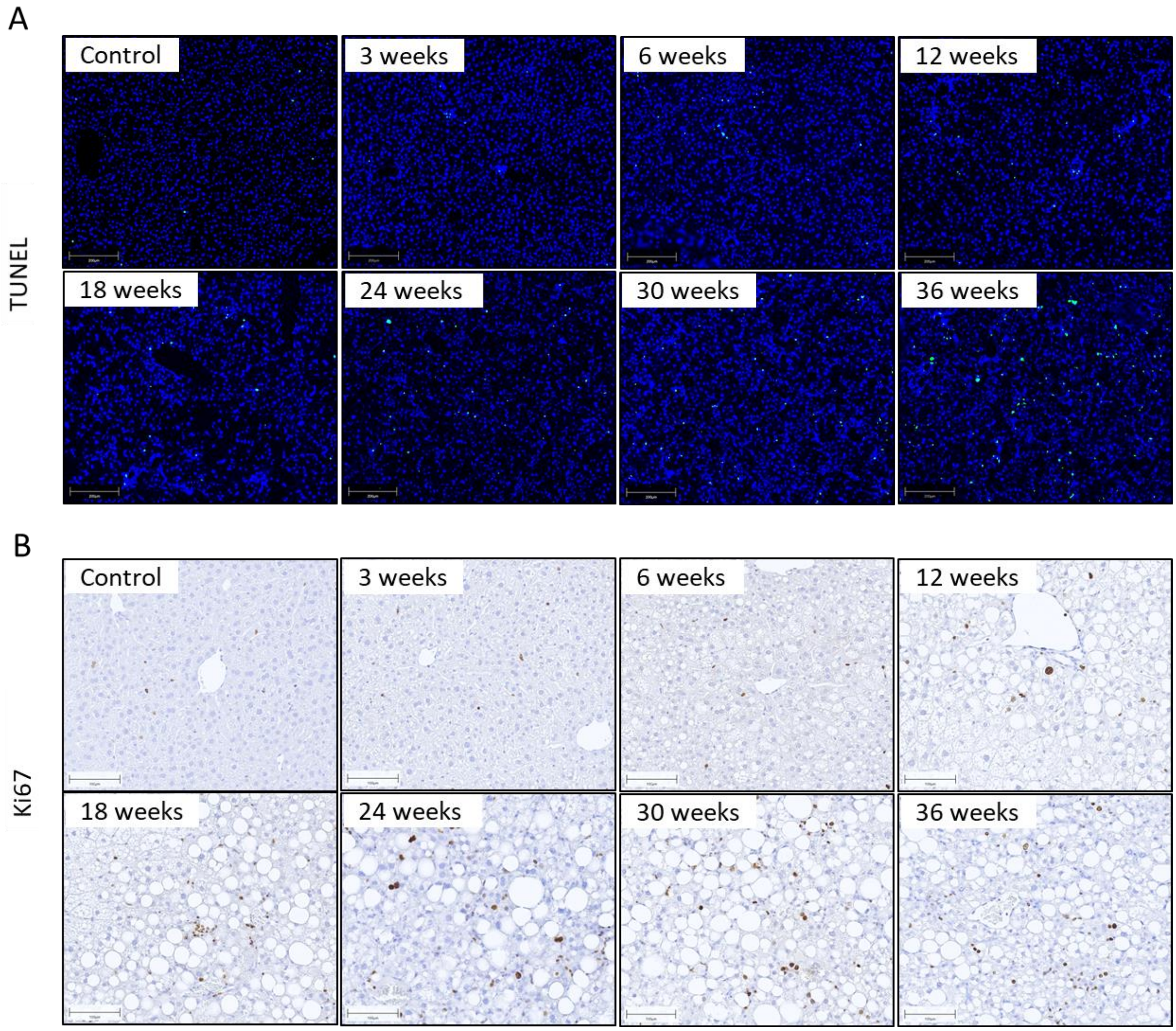

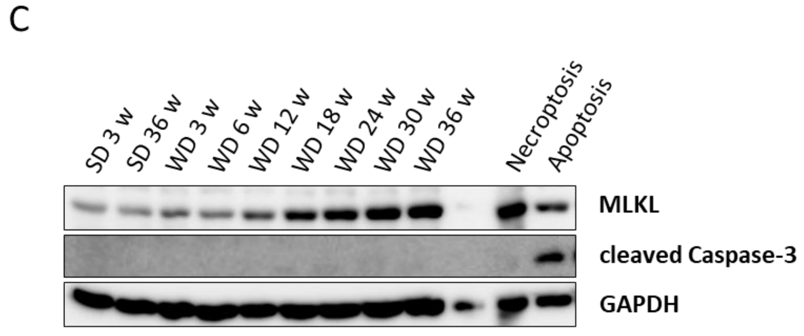

Figure 3.5. NAFLD progression to NASH leads to increased cell death by necroptosis and replacement proliferation. A. TUNEL staining shows time-dependently increasing cell death rate after feeding on WD. Scale bars: 200 µm. TUNEL: Terminal deoxynucleotidyl transferase dUTP nick end labeling; Control: 3 weeks of SD feeding. **B.** Ki67 staining of WD livers shows time-dependently increasing cell proliferation after feeding on WD. Scale bars: 100 µm. Ki67: cell proliferation marker; Control: 3 weeks of SD feeding. **C.** Western blot of liver tissue samples shows an activation of necroptotic (MLKL) but not apoptotic (cleaved Caspase-3) cell death pathway after feeding on WD. The last two loadings are positive controls for necroptosis and apoptosis. MLKL: mixed lineage domain-like pseudokinase; GAPDH: Glyceraldehyde 3-phosphate dehydrogenase, housekeeping gene; SD: standard diet; WD: western-style diet.

To further confirm the disease progression in the present NAFLD mouse model, clinical markers of liver damage were measured in plasma. The activities of alanine aminotransferase (ALT), aspartate aminotransferase (AST), glutamate dehydrogenase (GDH), and lactate dehydrogenase (LDH) increased from week 12 of WD feeding onwards, and reached their maximal levels at week 24 of WD feeding, after which they did not further increase in later time-points (Fig. 3.6).

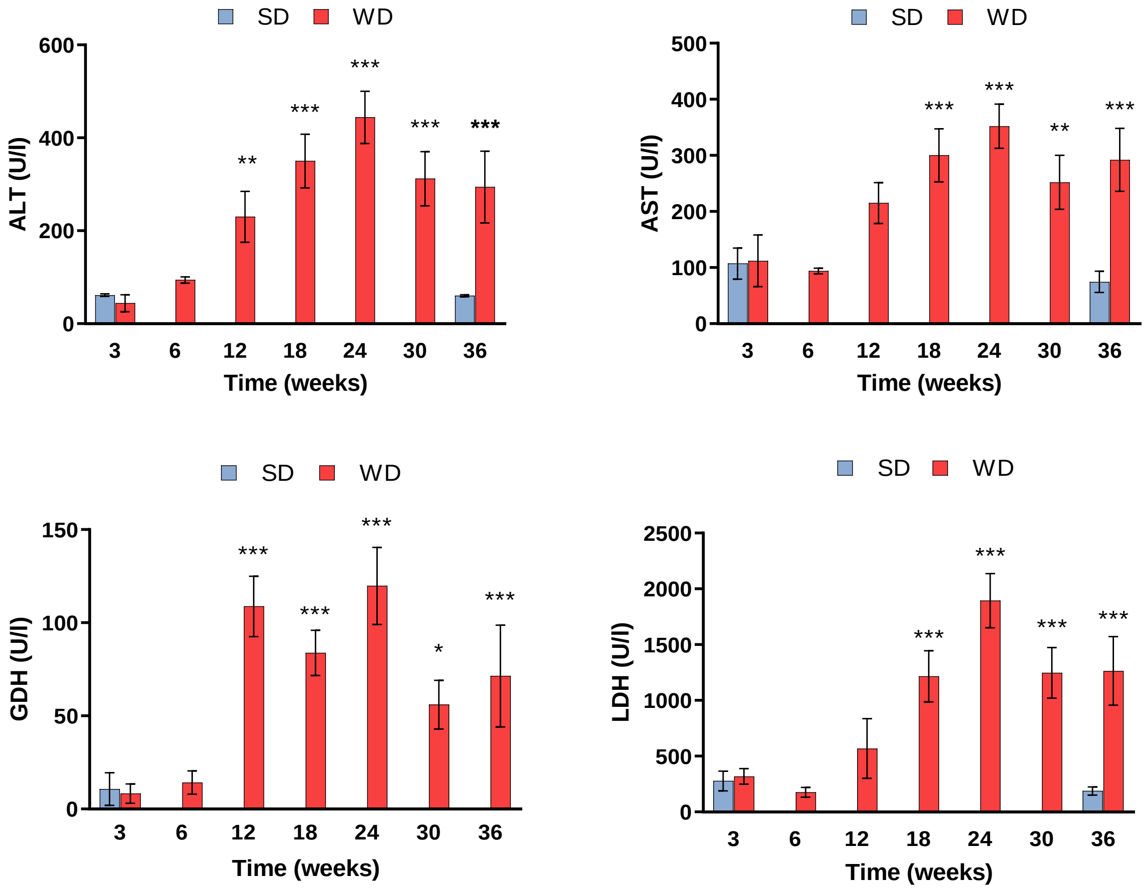

Figure 3.6. Clinical chemistry alterations during NAFLD progression. Plasma analysis showed time-dependent increase of the activities of the liver enzymes ALT, AST, GDH, and LDH after feeding on WD compared to 3 weeks of SD feeding. All of the enzyme activities reached the peak at week 24 of WD feeding. The results are presented as means ± SEM of at least 4 biological replicates. *P<0.05; **P<0.01; ***P<0.001; ALT: alanine aminotransferase; AST: aspartate aminotransferase; GDH: glutamate dehydrogenase; LDH: lactate dehydrogenase; SD: standard diet; WD: western-style diet.

Regardless of the etiology, chronic liver injury has been showed to lead to so called ductular reaction, the formation of cholangiocyte-derived progenitor-like ductular reactive cells (Stanger, 2015). To investigate if ductular reaction occurs in the present NAFLD mouse model as well, liver paraffin sections were stained against cytokeratin-19 (CK19), a marker of cholangiocytes. As expected, in healthy livers the cholangiocytes appeared only in the periportal zone. In contrast, progressive ductular reaction was observed in WD-fed mice in the periportal and midzonal compartment of the liver lobule, starting at week 18 and progressing time-dependently (Fig. 3.7.).

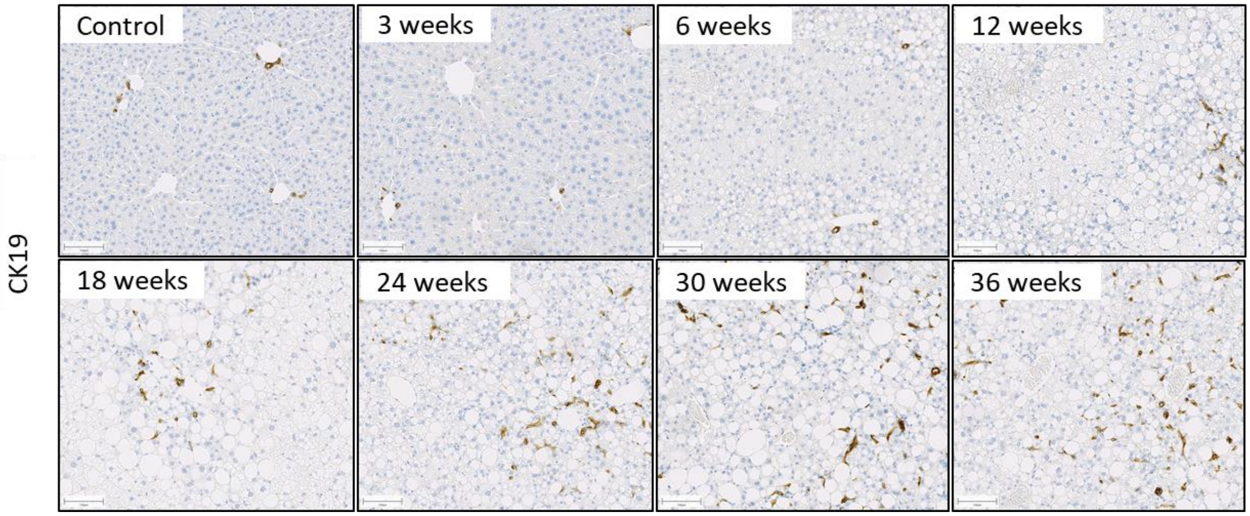

Figure 3.7. Progressive ductular reaction during NAFLD progression. CK19 immunostaining showing an increasing ductular reaction in the periportal and midzonal compartments of the liver lobule from 18 weeks of WD feeding onwards. Scale bars: 100 µm; CK19: cytokeratin-19; Control: 3 weeks of SD feeding.

NAFLD progression may lead to activation of hepatic stellate cells (HSCs) and fibrogenesis (Schuppan et al., 2018). To evaluate the progression of fibrosis in the present NAFLD mouse model, the activation state of HSCs was studied by desmin (a marker of quiescent and activated HSCs) and alpha-smooth muscle actin (α-SMA; a marker of activated HSCs) immunostaining. Desmin staining showed a time-dependent accumulation of HSCs in the periportal/midzonal compartment of the liver from week 18 of WD feeding onwards (Fig. 3.8A). The activation of HSCs was confirmed by alpha-smooth muscle actin staining (Fig. 3.8B). To investigate collagen accumulation as a consequence of HSC proliferation and activation, Sirius Red staining of liver paraffin sections was performed. In line with the HSC proliferation and activation, time-dependent accumulation of collagen was observed from week 18 onwards, leading to an intensive periportal fibrosis (Fig. 3.8C).

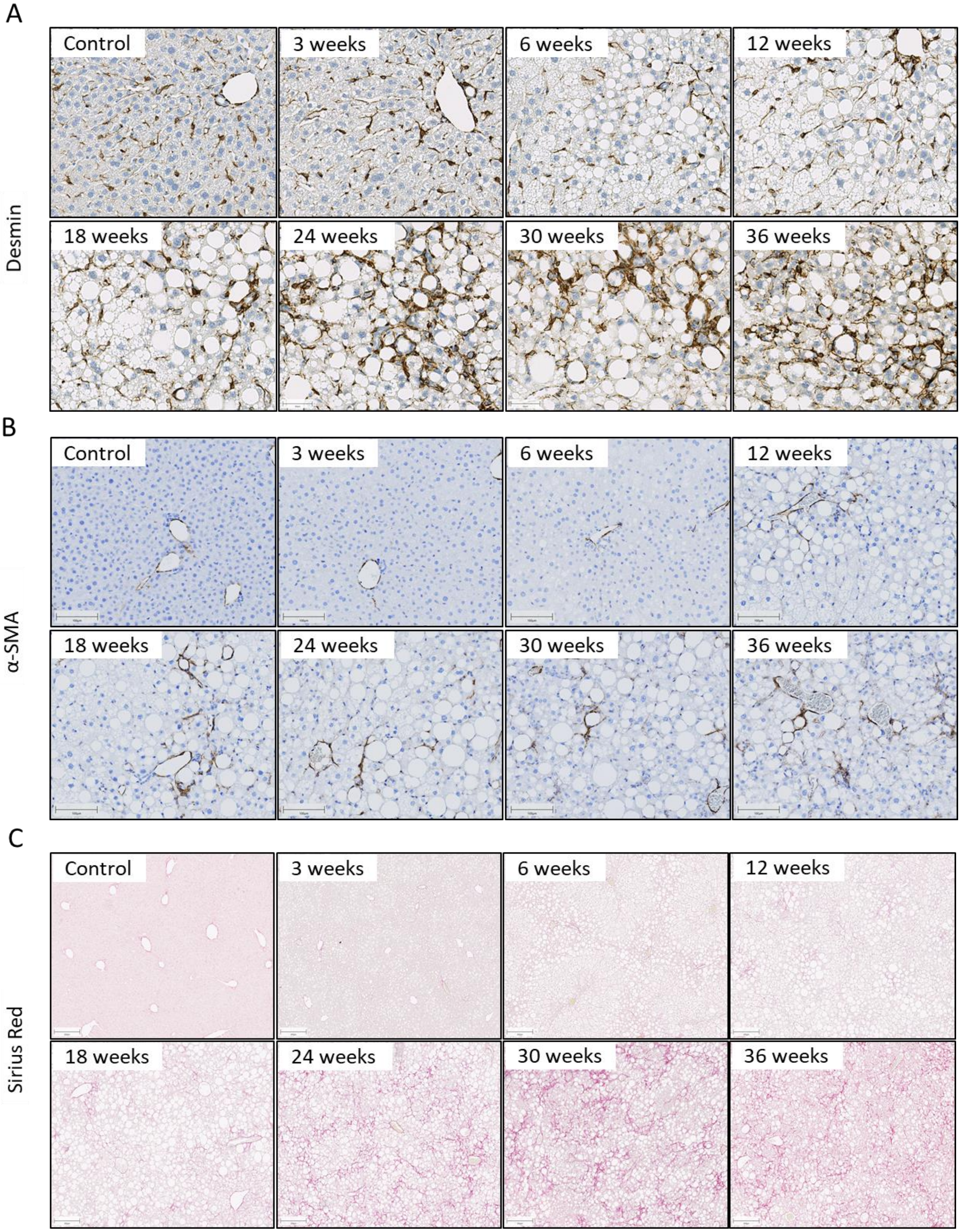

Figure 3.8. Development of periportal fibrosis during NAFLD progression. A. Desmin staining showing a time-dependent accumulation of HSC after WD feeding. **B.** α-SMA staining showing activated HSCs at week 18 and later time points. **C.** Sirius Red staining showing time-dependently increasing collagen accumulation and periportal fibrosis. Scale bars: 100 μm (A, B); 200 μm (C). α-SMA: alpha-smooth muscle actin; Control: 3 weeks of SD feeding.

In conclusion, long-term feeding of mice with WD recapitulates the stages of NAFLD progression including benign steatosis, leukocyte infiltration and macrophage crown-like structure formation, ductular reaction, fibrogenesis, and HCC development. In the next chapters, the mechanisms driving the transition from benign steatosis to the inflammation stage (NASH) will be investigated.

3.2 NAFLD represents a mild form of chronic cholestatic liver disease

In NASH patients, FXR agonists/FGF19 analogues (anti-cholestatic drugs) are surprisingly effective (Xu et al., 2014). To gain a deeper understanding of the mechanisms leading to the progression of NAFLD to NASH, and furthermore the link to cholestasis, bile acids and their transport chains were next studied in the established mouse model. First, the expression of relevant bile acid transporters and cholesterol 7 alpha-hydroxylase (Cyp7a1), a bile acid synthesis regulator, were studied both on RNA and on protein levels in liver tissue. On the RNA level, the relative expression of the sinusoidal uptake transporters Ntcp and Oatp decreased to 0.2-fold (Ntcp) and to 0.4-fold (Oatp) during the progression of NAFLD. In addition, the expression of the apical transporters Bsep and Mrp2 decreased down to 0.3 fold (Bsep) and to 0.5 fold (Mrp2). In contrast, the expression of the sinusoidal export transporters Mrp3 and Mrp4 decreased at the early weeks of WD feeding but afterwards increased into a slight upregulation up to 1.2 fold (Mrp3) and to 1.5 fold (Mrp4) (Fig. 3.9A). Interestingly, similarly as reported in the previous chapter, the most extreme changes were observed from week 18 to week 24 of WD feeding.

In addition to the bile acid transporters, the RNA expression of Cyp7a1 was measured. The Cyp7a1 level was slightly upregulated up to week 6 of WD feeding, and then strongly downregulated during the disease progression from week 12 of WD feeding onwards. Similarly as in the bile salt transporters, the most extreme Cyp7a1 level was reached at week 24 of WD feeding, where the expression was only 0.25-fold compared to 3 weeks of SD feeding (Fig. 3.9B). The RNA-level findings were confirmed on the protein level by immunostaining the liver tissue sections against NTCP and BSEP. In agreement with the RNA data, expression of NTCP decreased time-dependently in the pericentral and the midzonal hepatocytes. However, the periportal hepatocytes showed only a modest decrease of NTCP (Fig. 3.10A). In contrast to NTCP, the BSEP was not decreased after WD feeding but showed a fragmented pattern of the bile canaliculi after week 18 of WD feeding (Fig. 3.10B).

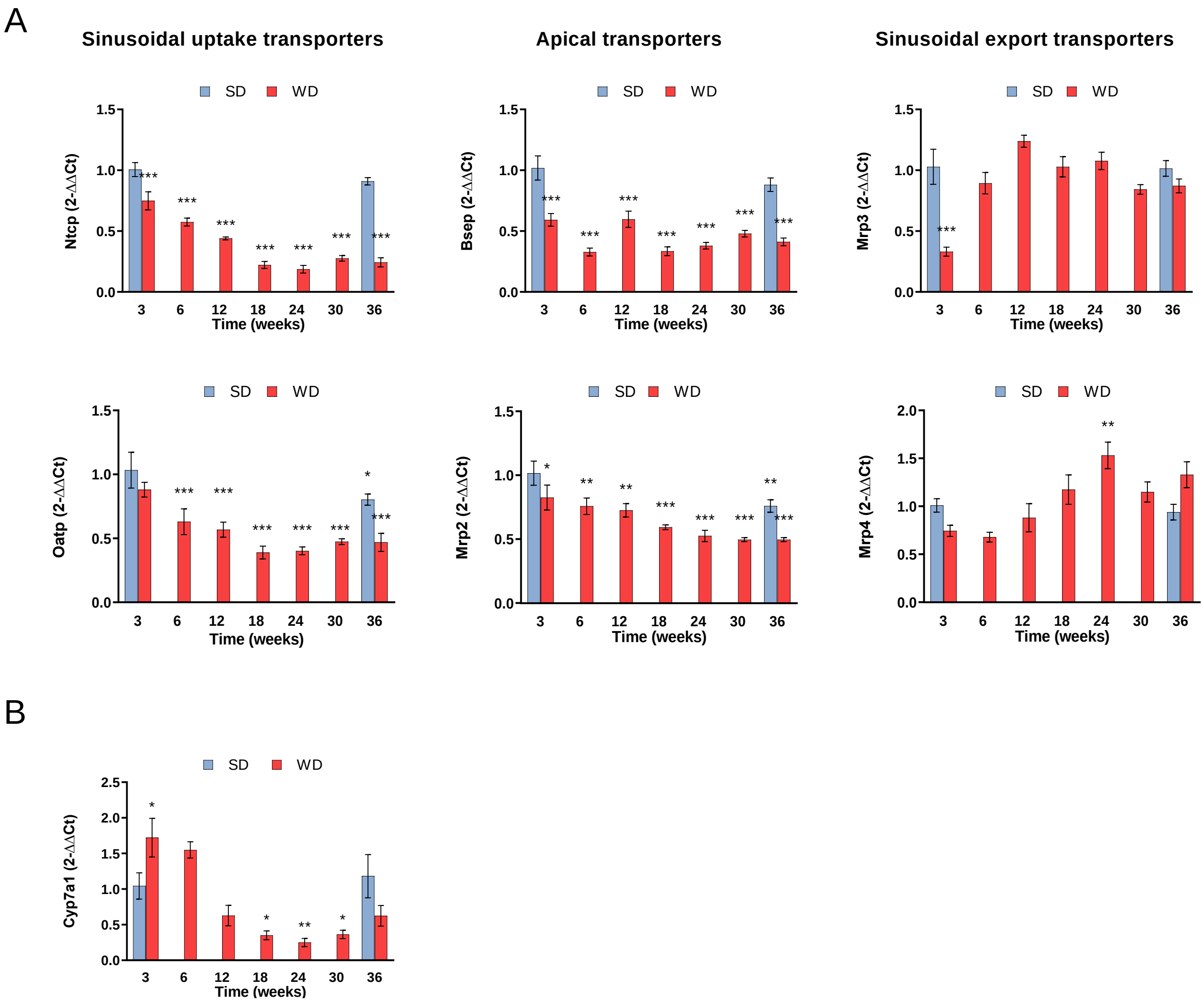

Figure 3.9. Altered expression of bile acid transporters during NAFLD progression. A. qRT-PCR analysis of liver tissue showing a time-dependent decrease in the expression of the sinusoidal uptake transporters Ntcp and Oatp, and the apical transporters Bsep and Mrp2. The sinusoidal export transporters Mrp3 and Mrp4 are first decreased in weeks 3 to 6 of WD feeding and slightly upregulated at later time points. *P<0.05; **P<0.01; ***P<0.001, compared to 3 weeks of SD. **B.** Cyp7a1 expression showing time-dependent downregulation after WD feeding. The data are presented as means ± SEM of at least four biological replicates. SD: standard diet; WD: western-style diet.

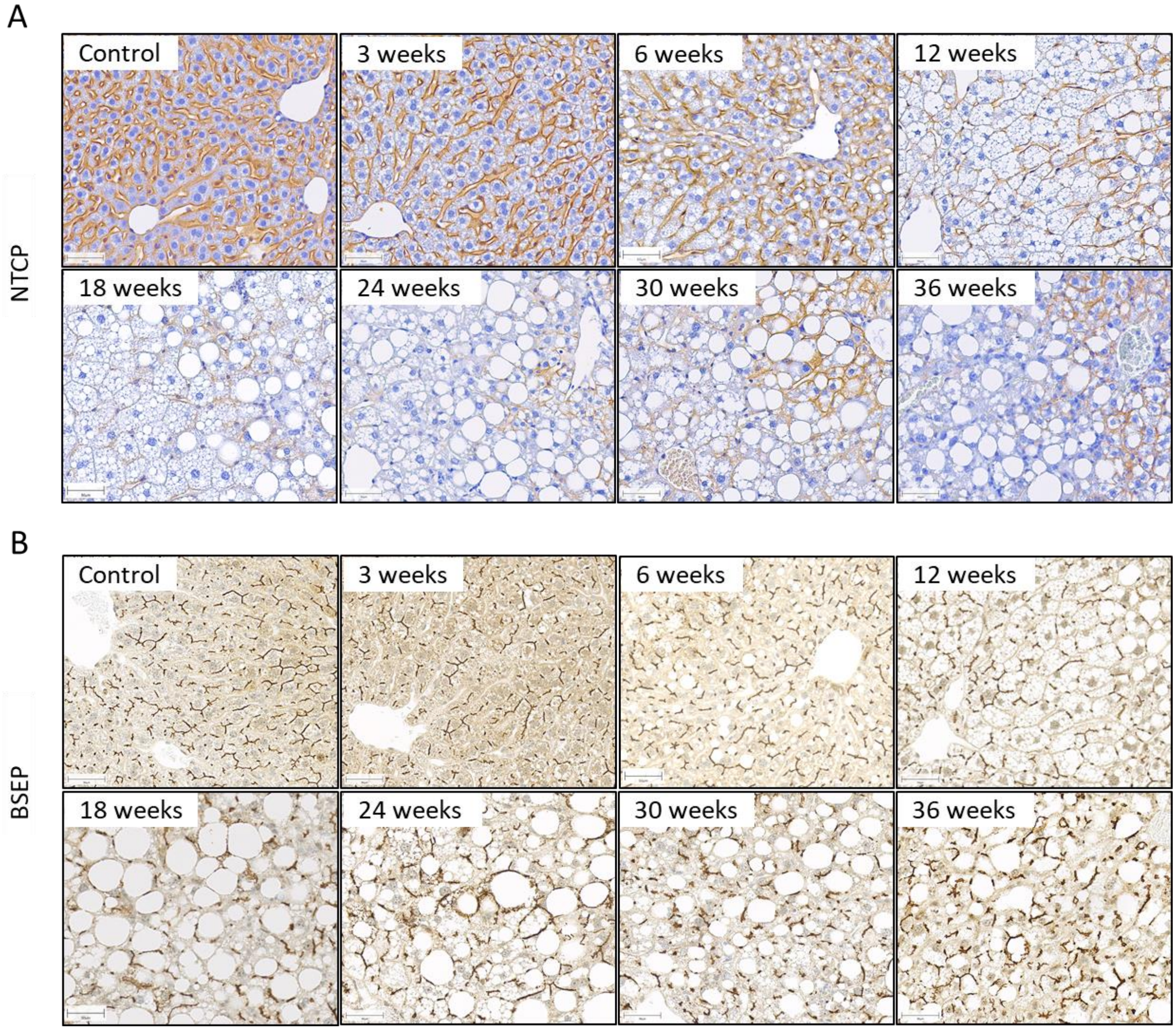

Figure 3.10. Altered protein expression of bile acid transporters during NAFLD progression. A. Representative immunohistochemistry images of the sinusoidal uptake transporter NTCP showing time-dependent reduction particularly in the pericentral and midzonal hepatocytes. **B**. BSEP immunostaining showing a fragmented pattern of bile canaliculi from week 18 onwards after feeding on WD. Scale bars: 100 µm. NTCP: Na+-taurocholate co-transporting polypeptide; BSEP: Bile Salt Export Pump; Control: 3 weeks of SD feeding.

In order to further investigate the role of bile acids in the progression of NAFLD to NASH, bile acid concentrations were measured in bile, in plasma and in liver tissue (Fig. 3.11A). The sum concentrations of all bile acids in bile was slightly decreased after the WD feeding. Nevertheless, the decrease did not follow a time-dependent manner but rather stayed on a constant level throughout the NAFLD progression. In contrast to the bile, the plasma measurement showed a significant increase in the sum of bile acids at week 24 and at later time points. A similar pattern was also shown in the liver tissue, where the sum of bile acids increased from 103 µM (3 weeks of SD feeding) up to 278 µM (24 weeks of WD feeding). In line with the previously showed results, the most drastic change in the bile acids in both plasma and in liver tissue occurred at 24 weeks of WD feeding and remained constant at the later time points. These data showed bile acid retention in the liver tissue during NAFLD progression.

Next, the spatial expression of the retained bile acids was investigated. To accomplish that, MALDI-MSI was used to image taurocholate in the mouse liver tissue at weeks 3 and 36 of WD feeding, Furthermore, the MALDI signal was superimposed onto adjacent liver tissue sections stained with arginase. As expected, after 3 weeks WD feeding a low signal of taurocholate was detected all over the entire liver tissue but primarily in the midzonal and periportal area, as revealed by arginase staining. At week 36 of WD feeding, a strong accumulation of taurocholate was detected mainly in the midzonal and periportal compartments of the liver lobule (Fig. 3.11B).

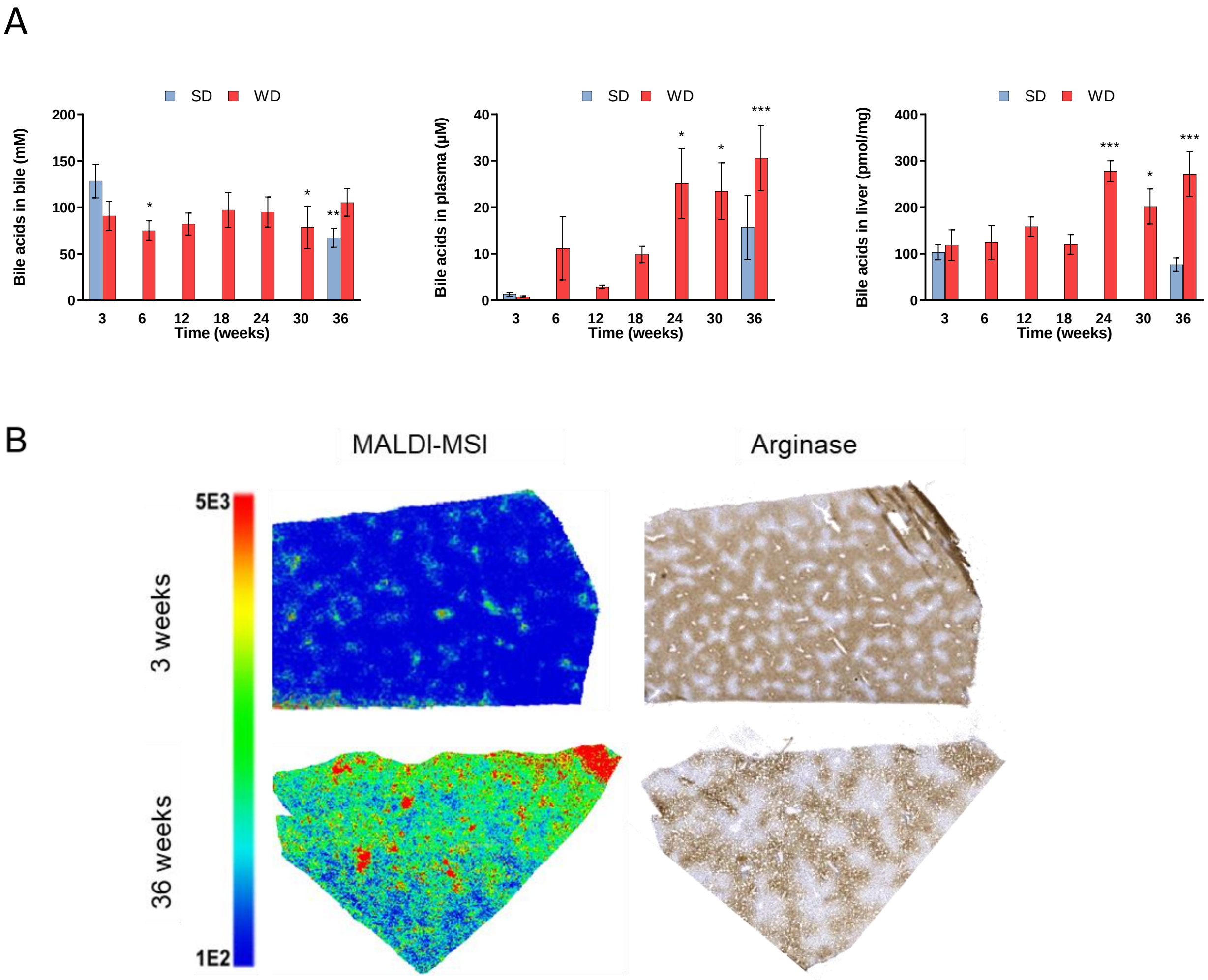

Figure 3.11. NAFLD progression coincides with development of a mild form of cholestasis. A. The sum concentrations of bile acids increases in plasma and in liver tissue but not in bile during NAFLD progression. *P<0.05; **P<0.01; ***P<0.001, compared to 3 weeks of SD. The data are presented as means ± SEM of at least four biological replicates. **B**. Representative MALDI-MSI images showing a strong accumulation of taurocholate in the liver lobule tissue after 36 weeks of WD feeding. Superimposing onto adjacent liver slices stained with arginase revealed that the accumulation mainly occurs in midzonal and periportal compartments of the liver lobule. SD: standard diet; WD: western-style diet.

3.3 Macropinocytosis of bile: a so far unrecognized mechanism of NASH progression

After revealing that the bile acids strongly accumulate in the liver tissue during NAFLD progression, the driving mechanisms of this phenomenon were further studied. To understand from which position of the bile transport chain the bile acid accumulation stems, bile acid transport was investigated intravitally in SD and WD-fed mice using two-photon imaging technique. As expected, in the healthy SD-fed mice the bile acid analogue cholyl-L-lysyl-l-fluorescein (CLF) was transported from liver sinusoids to hepatocytes and further secreted to bile canaliculi; within two hours after injection, the signal of CLF was completely cleared from the bile canaliculi (Fig. 3.12). However, the bile transport system became disrupted from 18 weeks of WD feeding onwards, resulting in vesicular regurgitation of the bile from bile canaliculi back to the hepatocytes (Fig. 3.13). Fast sequences of two-photon recording revealed that this vesicular regurgitation of bile started from invagination of the hepatocyte apical membrane that delimits the bile canaliculus. Correspondingly, approximately 0.5-2 µm CLF-filled vesicles were formed and subsequently taken back up into the hepatocytes (Fig. 3.13). Hepatocytes that undergo retrograde vesicular uptake showed a higher intracellular cytoplasmic intensity of the green-fluorescent CLF, suggesting leakiness of the vesicles into the hepatocytes.

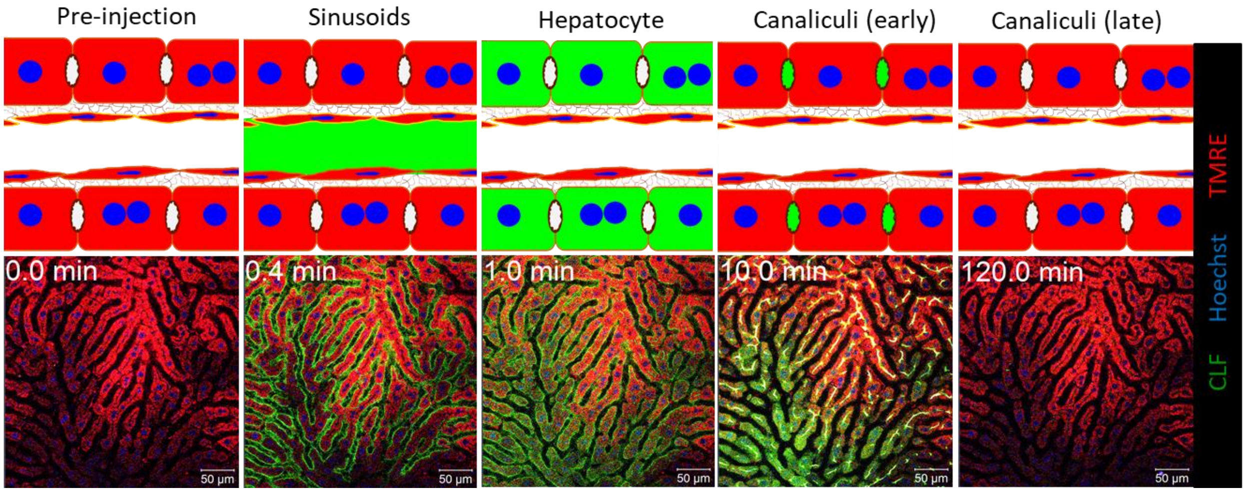

Figure 3.12. Uptake of CLF in healthy mouse liver. Intravital imaging of standard diet fed mouse showing an uptake of CLF from sinusoids to hepatocytes and a further secretion of CLF to bile canaliculi, leading to a complete clearance of CLF at 120 minutes after injection. Scale bars: 50 µm. CLF: Cholyl-L-lysyl-Fluorescein, bile acid analog; TMRE: tetramethylrhodamine ethyl ester, mitochondrial membrane potential; Hoechst: nuclei.

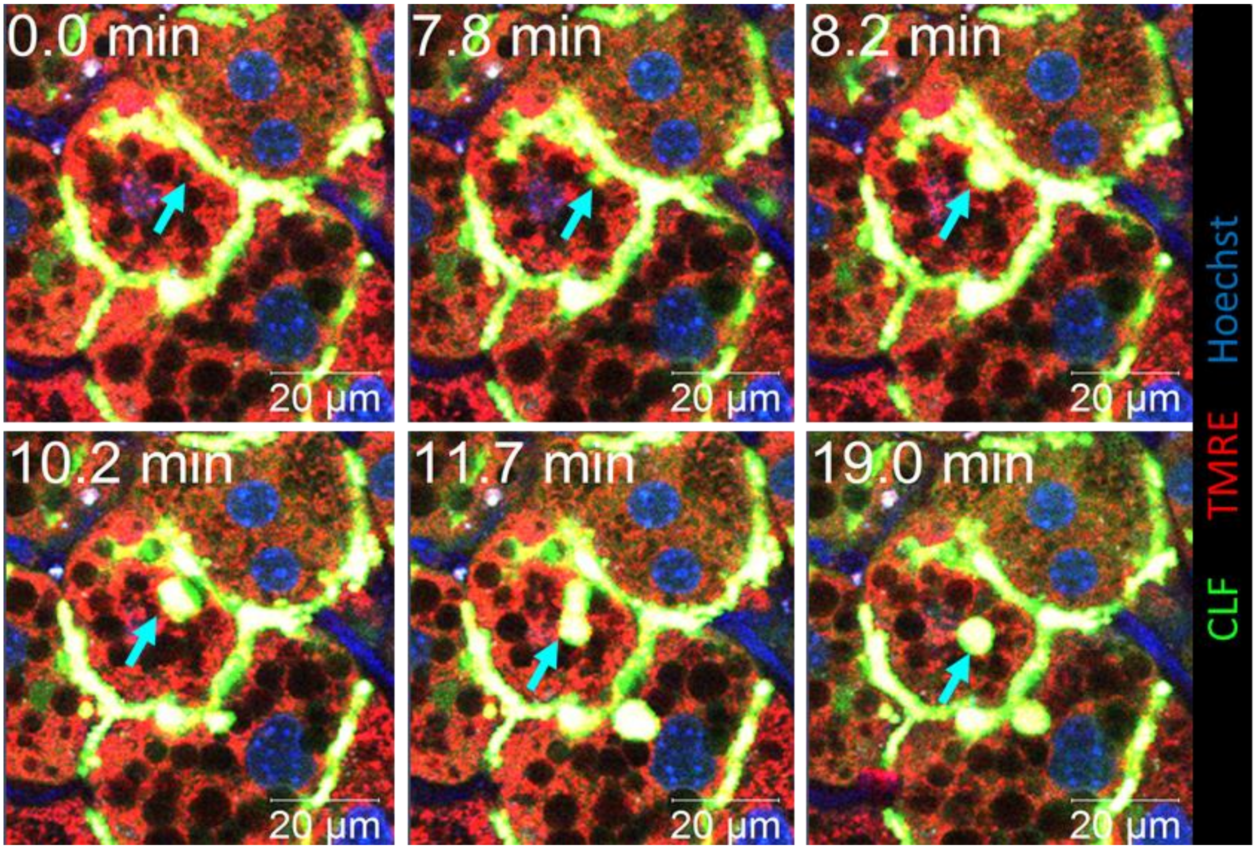

Figure 3.13. Retrograde vesicular uptake of bile back to hepatocytes coincides with NAFLD progression. Two-photon intravital imaging of the liver after 30 weeks of WD feeding shows a retrograde vesicular uptake of bile, which starts with hepatocyte apical membrane invagination (0.0–8.2 min; indicated as a turquoise arrow), resulting in bile-filled vesicle entering back to hepatocytes (10.2–19.0 min). Scale bars: 20 µm. CLF: Cholyl-L-lysyl-Fluorescein, bile acid analog; TMRE: tetramethylrhodamine ethyl ester, mitochondrial membrane potential; Hoechst: nuclei.

In order to verify that injecting CLF to the mice did not itself trigger the vesicular regurgitation of bile, Td-tomato reporter mice fed for 20 weeks with WD were imaged with intravital imaging technique. The mice are fluorescent reporters for all membranes, hence the possible vesicular regurgitation can be seen without injecting fluorescent dyes. Intravital imaging of the reporter mice revealed a similar formation of regurgitating vesicles from the bile canaliculi as was observed in the NAFLD mouse model after CLF injection (Fig.3.14).

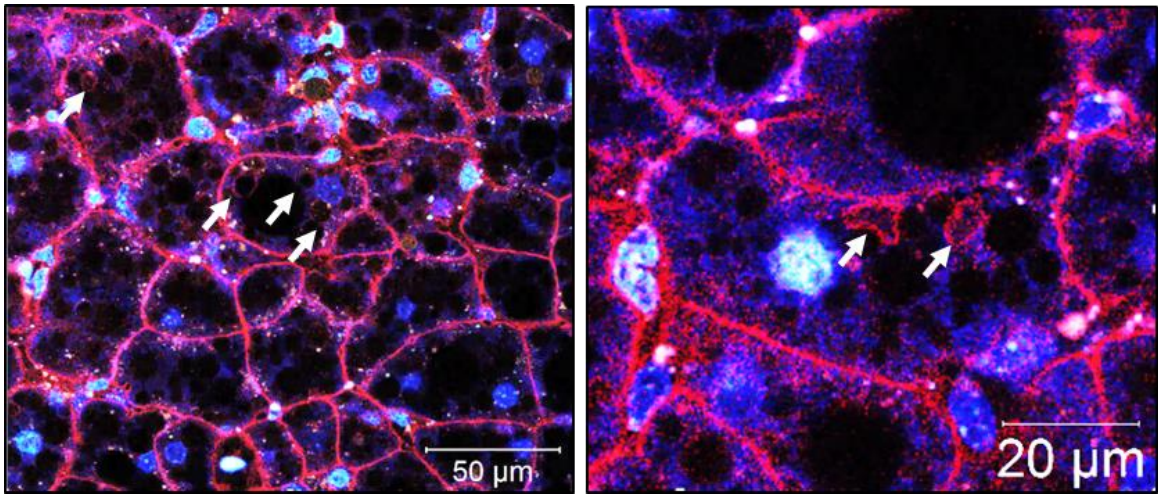

Figure 3.14. Vesicular regurgitation of bile occurs spontaneously during NAFLD progression. Td-Tomato reporter mice showing a formation of regurgitating vesicles after 20 weeks of WD feeding, indicated as white arrows. Scale bars: 50 µm and 20 µm.

To further confirm that the regurgitating vesicles were derived from bile canaliculi and remained surrounded by the apical hepatocyte membrane, livers of SD and WD-fed mice were stained against CD13, a bile canalicular marker. A 2D staining of liver sections confirmed an appearance of CD13-positive vesicles inside the hepatocytes, representing the vesicular uptake of bile back to hepatocytes (Fig. 3.15A). Moreover, a 3D reconstruction of the bile canalicular network showed an increasing number of CD13-positive disconnected segments after 24 weeks of WD feeding compared to 3 weeks of SD feeding (Fig. 3.15A). Quantification of the absolute CD13-positive canalicular network volume showed a time-dependent decrease, whereas the number of CD13-positive segments strongly increased from 24 weeks of WD feeding onwards (Fig. 3.15B).

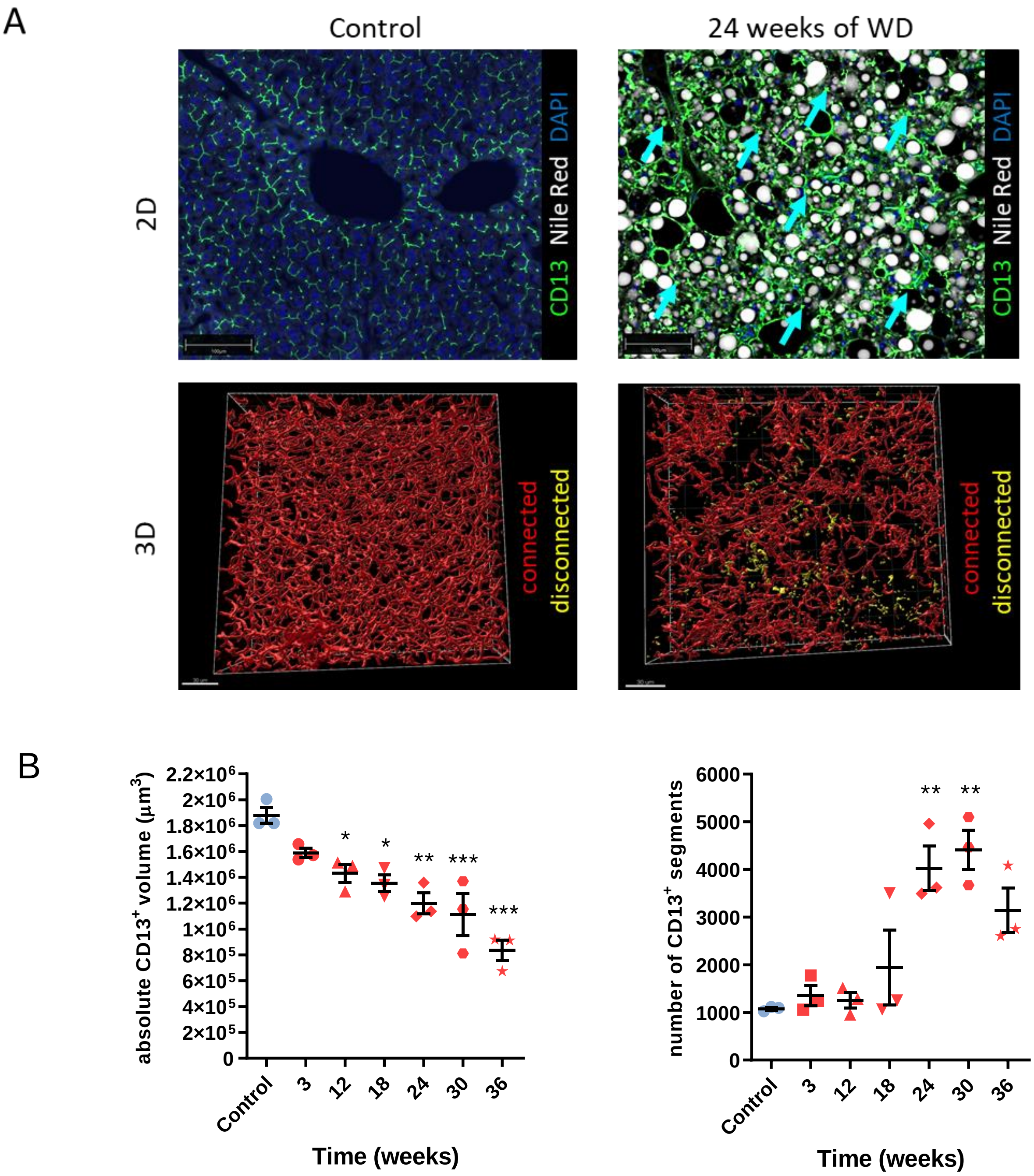

Figure 3.15. Retrograde vesicular uptake of bile during NAFLD progression gives the impression of fragmented canalicular network. A. 2D staining shows CD13-positive vesicles within hepatocytes after 24 weeks of WD, indicated as turquoise arrows. 3D reconstructions showing increasing number of disconnected CD13 positive segments after 24 weeks of WD. **B.** Quantification of CD13 reconstruction reveals time-dependent decrease in absolute CD13 positive volume, and an increase in the number of CD13 positive segments from week 24 of WD feeding on. *P<0.05; **P<0.01; ***P<0.001. The data are presented as means ± SEM from three biological replicates. Scale bars: 2D staining 100 µm; 3D staining 30 µm. CD13: bile canaliculi; Nile Red: lipid droplets; DAPI: nucleus; WD: western-style diet; Control: 3 weeks of SD feeding.

Next, it was crucial to define the exact mechanism that drives the retrograde vesicular uptake of bile acids in the NAFLD liver. In mammalian cells, the uptake mechanisms can be roughly divided into three classes: phagocytosis, receptor-mediated endocytosis, and pinocytosis (Neekhra & Padh, 2004). Since phagocytosis is a mechanism for transporting large particles, and receptor-mediated endocytosis results in a formation of a smaller vesicle than what was seen in the intravital imaging, the presumed mechanism for the observed vesicular uptake was pinocytosis, more specifically macropinocytosis. To test this hypothesis, several different links to macropinocytosis were studied. First, macropinocytosis is known to be induced by inflammatory cytokines in different cell types, such as macrophages (Wójciak-Stothard et al., 1998) and epithelial cells (Miyake et al., 2016). Thus, RNA levels of proinflammatory cytokines TNF-α, IL12b and IL6 in the liver tissue were measured. Interestingly, the relative expression of TNF-α and IL12b increased time-dependently in WD-fed mice up to 8-fold (TNF-α, 18 weeks) and 19-fold (IL12b, 24 weeks) (Fig. 3.16). In contrast, IL6 first decreased at weeks 3 and 6 of WD feeding, followed by a return to approximately control levels in later weeks of WD. In line with the results presented earlier, the cytokine levels did not remarkably further increase after week 24 of WD feeding.

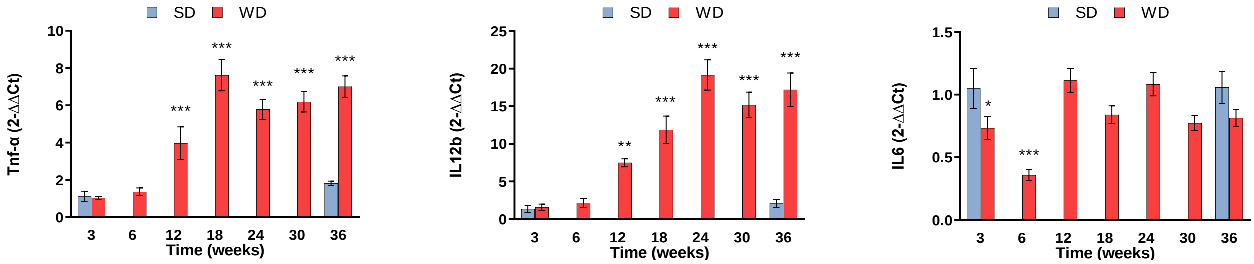

Figure 3.16. Proinflammatory cytokines increase time-dependently in NAFLD. RT-qPCR of Tnf-α and IL12b showed a time-dependent increase in the liver tissue compared to the 3 weeks of SD. IL6 levels initially dropped in the weeks 3-6 of WD feeding but returned back to control levels in later weeks of WD. **P<0.01; ***P<0.001. The data are presented as means ± SEM from at least four biological replicates. Tnf-α: tumor necrosis factor α; IL12b: interleukin 12b; IL6: interleukin 6; SD: standard diet; WD: western-style diet.

It is commonly known that one of the main proinflammatory cytokine producing cell types in chronic liver diseases is macrophages. Based on the previously presented results showing an increased macrophage accumulation and increasing cytokine expression in the liver, the next goal was to deplete macrophages in order to see if macropinocytosis can be intercepted. Therefore, mice fed for 24 weeks with WD were treated with liposome-encapsulated clodronate (L-clodronate) and afterwards imaged with two-photon intravital imaging technique. As a result, the macrophage depletion almost completely blocked macropinocytosis (Fig. 3.17), confirming that the local cytokine secretion by macrophages is triggering the observed bile macropinocytosis in WD-fed mice.

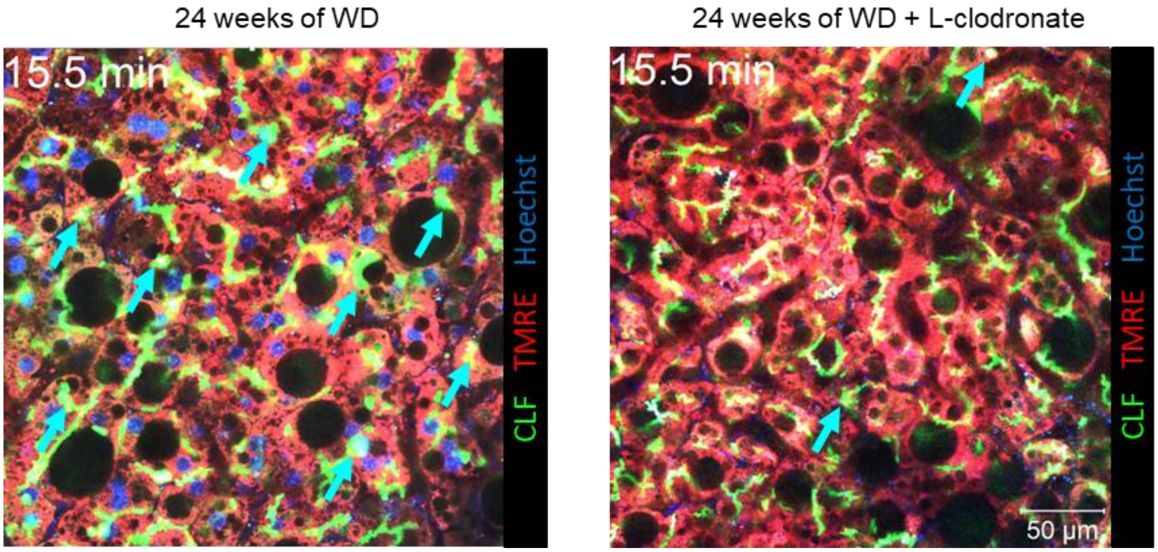

Figure 3.17. Macrophage depletion efficiently blocks macropinocytosis. Intravital two-photon imaging of control and liposome-encapsulated clodronate (L-clodronate) treated WD-fed mice showing that macrophage depletion efficiently blocks macropinocytosis. The snapshots were taken 15.5 minutes after CLF administration. Scale bars: 50 µm. CLF: Cholyl-Lysyl-Fluorescein, bile acid analog; TMRE: tetramethylrhodamine, mitochondrial membrane potential; Hoechst: nuclei; WD: western-style diet.

3.4 Macropinocytosis of bile is evident in human patients with NASH

In order to estimate if the disease progression in the NAFLD mouse model recapitulates human NAFLD stages, liver histology of different stages of NASH patients was studied. Hematoxylin & eosin staining showed a pericentral hepatocyte steatosis in all of the studied stages (Fig. 3.18). In addition, pericentral liver injury and fibrosis were present from stage F1 onwards. In stages F2–F4, bridging fibrosis became evident. Moreover, similarly as the hepatocyte steatosis, macrophage crown-like structure was observed in all stages of fibrosis but it became more prominent in the stages F2-F4. Furthermore, in order to evaluate if macropinocytosis takes place in human NAFLD, the liver samples were stained for CD13. The staining revealed that the CD13-positive segments of bile canalicular network were present already in the stage F0. However, they became more prominent in the stages F2–F4, suggesting that macropinocytosis plays a role in human NAFLD progression (Fig. 3.18).

Taken together, these data demonstrated that hepatocyte steatosis, fibrosis, macrophage crown-like structure formation, and macropinocytosis were observed in the human NASH patients similarly as in the established NAFLD mouse model.

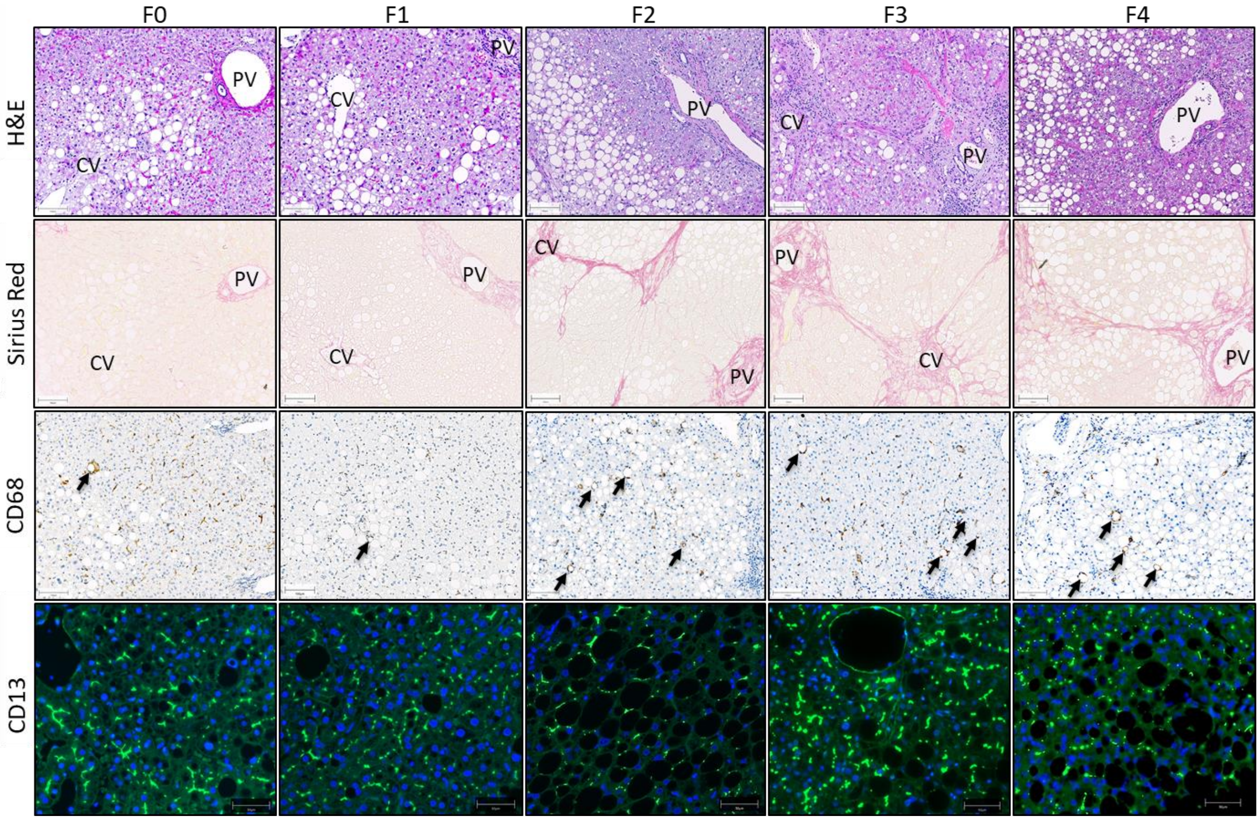

Figure 3.18. Liver histology of human NASH patients. Representative images of human NAFLD fibrosis stages 0–4 (F0–F4) showing pericentrally starting steatosis and fibrosis. CD68 staining shows macrophage crown-like structure formation indicated as black arrows, and CD13 staining shows bile canalicular network segmentation mainly in the stages F2–F4. Scale bars: H&E, Sirius Red, CD68 staining 100 µm, CD13 staining 50 µm. CV: central vein; PV: portal vein; H&E: hematoxylin & eosin, CD68: macrophages; CD13: bile canaliculi.

3.5 Targeting macropinocytosis prevents the progression of NAFLD to NASH

After revealing that macropinocytosis is the mechanism behind retrograde vesicular transport of bile and hence one of the possible reasons for NAFLD progression to NASH, macropinocytosis was specifically targeted in order to prevent the disease progression. A recently published pharmacological screen identified a compound called imipramine as an inhibitor that is specific for macropinocytosis without influencing phagocytosis or receptor-mediated endocytosis (Lin et al., 2018). Thus, imipramine was tested as a compound to intervene NAFLD progression in the next experiments.

3.5.1 Single dose of imipramine reduces macropinocytosis

In the first intervention experiment, mice were fed with WD for 24 weeks, injected with CLF and recorded by intravital imaging technique to observe the degree of macropinocytosis. After 20 minutes of imaging, the mice were administered with a single dose of imipramine in concentration of 50 mg/kg. Interestingly, a single dose of imipramine efficiently arrested macropinocytosis (Fig. 3.19). Moreover, the macropinocytosis cessation lasted up to 12 hours, after which the first signs of vesicular regurgitation started to appear. In addition to imipramine-treated mice, control mice without imipramine injection were imaged to avoid the bias originating from time-dependent CLF fading. In contrast to imipramine-treated mice, intense macropinocytosis was observed in the control mice throughout the 12 hours of imaging.

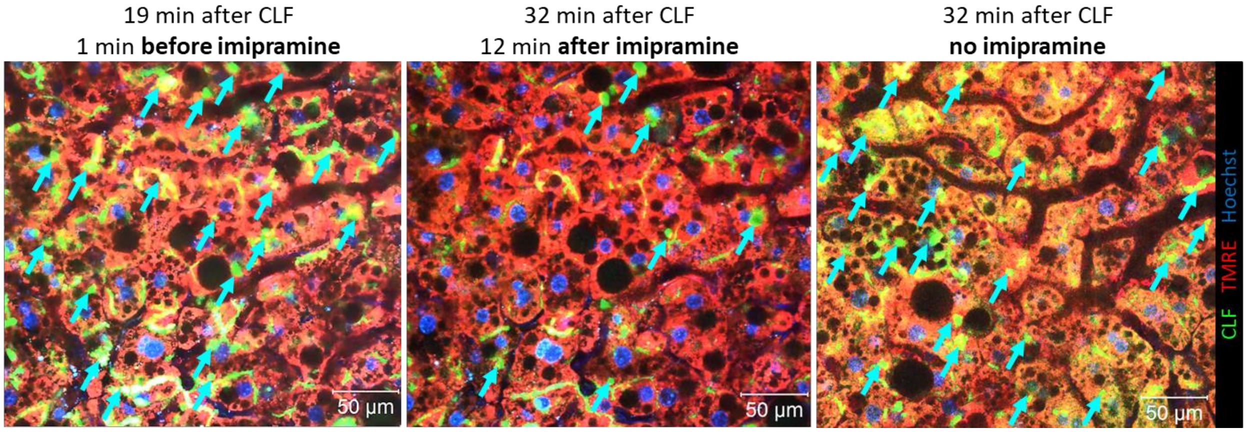

Figure 3.19. Single dose of imipramine efficiently blocks macropinocytosis in NAFLD mice. Two-photon intravital imaging showing an extensive macropinocytosis after 24 weeks of WD (left image, macropinocytosis indicated as turquoise arrows, snapshot taken 19 minutes after CLF injection). A single application of imipramine efficiently blocked macropinocytosis (image in the middle, snapshot taken 32 minutes after CLF injection and 12 minutes after imipramine application). The CLF-positive vesicles seen after imipramine administration were present in the liver tissue before the application. The rightmost image shows a control mouse 32 minutes after CLF injection without imipramine application. Scale bars: 50 µm. CLF: Cholyl-L-Lysyl-Fluorescein, bile acid analog; TMRE: tetramethylrhodamine, mitochondrial membrane potential; Hoechst: nuclei.

3.5.2 NAFLD progression can be intervened with long-term treatment with imipramine

As showed in the previous section, macropinocytosis could be blocked with a single dose of imipramine. Thus, the next step was to study if NAFLD progression can be permanently intervened by repeated administration of imipramine to WD-fed mice. In addition, three other NALFD intervention groups were added as controls: (1) vehicle treatment (2) obeticholic acid (OCA) treatment and (3) switching the WD to SD (Fig. 3.20A). Therefore, mice after 18 weeks of

WD were orally administrated either with 50 mg/kg imipramine or with vehicle every 12 hours, or with 30 mg/kg OCA every 24 hours for 8 consequent weeks. The fourth group was switched from WD to SD feeding with no additional treatment. Blood samples were collected right before starting the interventions and at the end of the intervention period (Fig. 3.20A). In order to evaluate the progression of NAFLD, the liver function biomarkers ALT, AST, and alkaline phosphatase (ALP) in plasma were first measured. Interestingly, after 8 weeks of interventions, ALT levels were lowered in imipramine as well as in SD but not in the OCA group. Moreover, the AST levels significantly increased in the vehicle group but were restrained to their original levels in all of the intervention groups. In accordance to the ALT results, ALP levels significantly decreased in both imipramine and in SD group, whereas neither OCA nor vehicle treatment affected them (Fig. 3.20B).

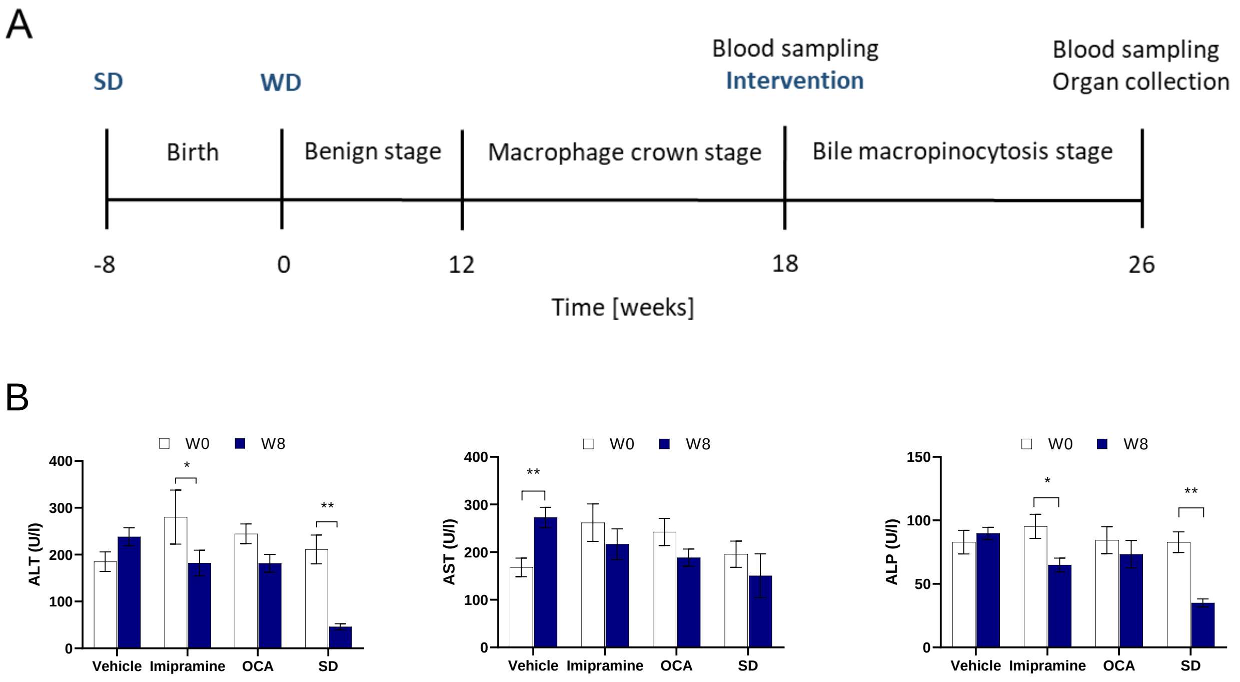

Figure 3.20. Blocking macropinocytosis prevents NAFLD progression. A. Experimental design. **B.** The graphs showing alanine aminotransferase (ALT), aspartate aminotransferase (AST) and alkaline phosphatase (ALP) levels in plasma before (white bars) and after (blue bars) interventions. *P<0.05; **P<0.01. The data are presented as means ± SEM from at least 9 biological replicates. W0: week 0, before starting the intervention; W8: week 8, at the end of the intervention; OCA: obeticholic acid; SD: standard diet.

In addition to the changes in the liver function enzymes, tissue-level modifications after the interventions were studied. Grossly, the livers of vehicle, imipramine and OCA mice appeared pale and enlarged, whereas the SD livers showed a normal, dark brown color and seemingly smaller size compared to the other groups (Fig. 3.21A). In addition, the SD group mice had decreased bodyweight and decreased liver-to-bodyweight ratio compared to the vehicle group. Nevertheless, neither imipramine nor OCA treatment decreased those parameters (Fig. 3.21B). In order to further evaluate the tissue level changes after interventions, liver tissue sections were stained with H&E staining. Livers of the vehicle-treated mice showed a heavy lipid accumulation inside the hepatocytes, occurring mainly in the midzonal and periportal compartment of the liver lobule. Similarly as in the vehicle mice, the livers of imipramine-treated mice appeared steatotic. However, OCA treatment seemingly decreased the number and size of lipid droplets accumulating inside the hepatocytes. Nevertheless, the most evident change was seen in the SD group, where the lipid accumulation had almost completely disappeared (Fig. 3.21A).

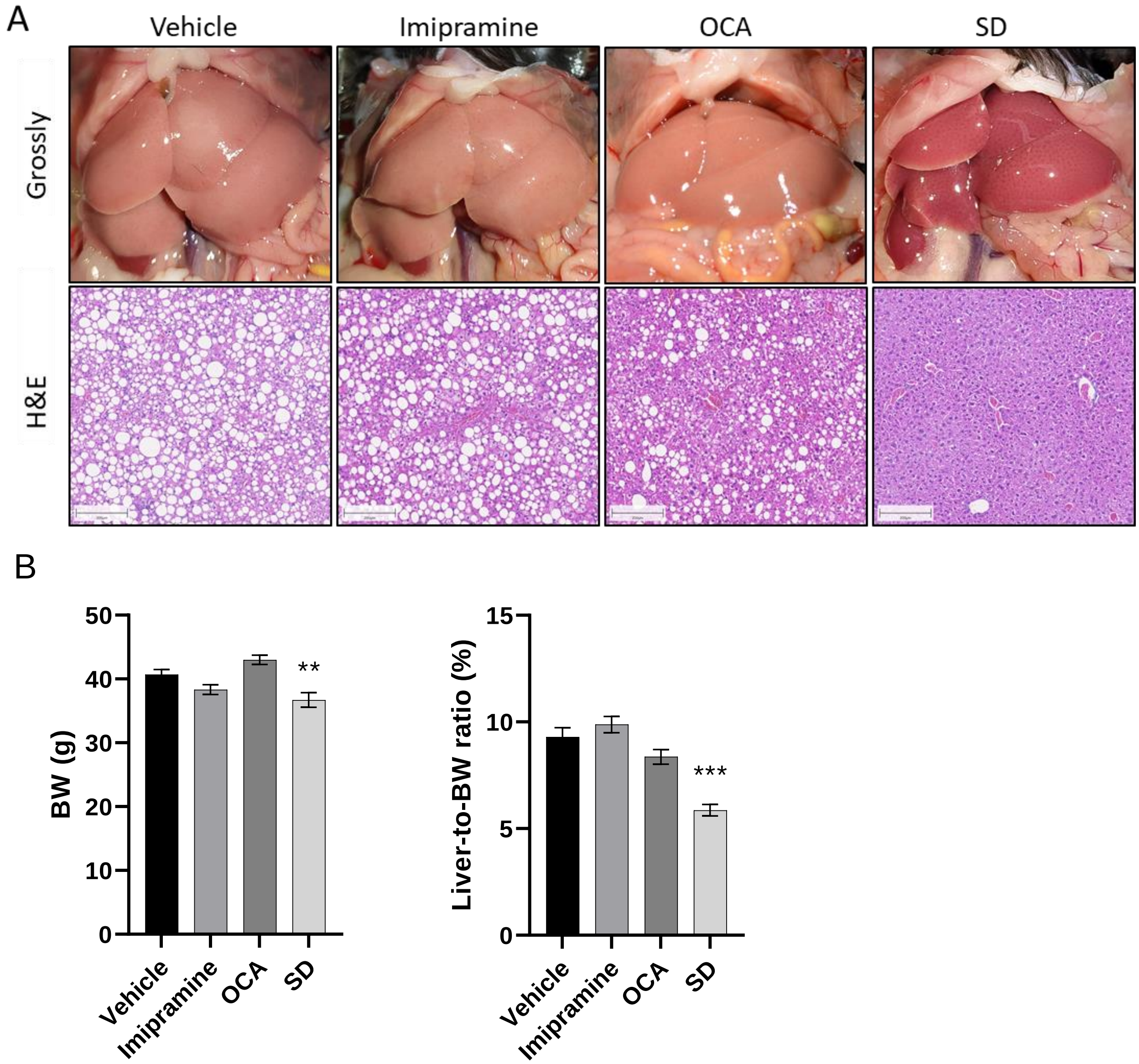

Figure 3.21. Changes in the liver lipid content and liver-to-bodyweight ratio after NAFLD interventions. A. Representative gross pathology and H&E staining images showing pale, lipid-accumulated livers after vehicle and imipramine treatment but decreased lipid accumulation after OCA treatment and SD. **B.** Mouse bodyweight and liver-to-bodyweight ratio decreased after SD intervention. $^{**}P<0.01$, $^{***}P<0.001$. The data are presented as means ± SEM from at least 9 biological replicates. OCA: obeticholic acid; SD: standard diet; H&E: hematoxylin & eosin staining; BW: bodyweight.

As shown in the previous results, progression from benign steatosis stage to NASH is characterized by infiltration of inflammatory cells. Thus, liver tissue sections were stained against the total leukocyte marker CD45 to evaluate the total number of inflammatory cells. Interestingly, all of the interventions appeared to decrease the infiltration and accumulation of CD45-positive cells (Fig. 3.22). However, the crown-like structures formed by macrophages were not altered following neither imipramine nor OCA treatment as demonstrated by F4/80 staining (Fig. 3.23A). Macrophages accumulated mainly in the midzonal and periportal compartment of the liver lobules, indicated as Cyp2e1 negative areas (Fig. 3.23A). In contrast, switching WD to SD lead to an almost total disappearance of the crown-like structures (Fig. 3. 23A). In line with these results, qRT-PCR analysis of the proinflammatory cytokines Tnf-α, IL12b, and IL6 showed no alteration following neither imipramine nor OCA treatment in comparison to the vehicle control (Fig. 3.23B). In contrast, the switch to SD lowered both Tnf-α and IL12b expression compared to the vehicle group and only IL6 levels remained unaltered (Fig. 3.23B).

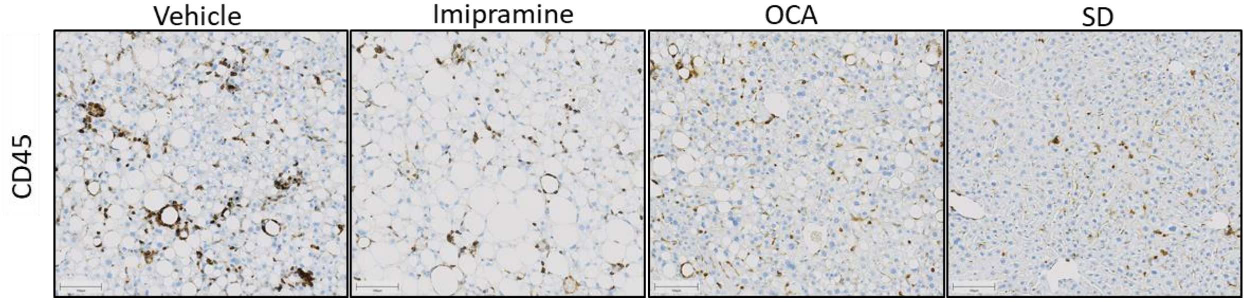

Figure 3.22. Immune cell infiltration after WD interventions. Representative images of CD45 staining showing decreased leukocyte and lymphocyte infiltration after WD interventions. Scale bars: 100 µm. OCA: obeticholic acid; SD: standard diet.

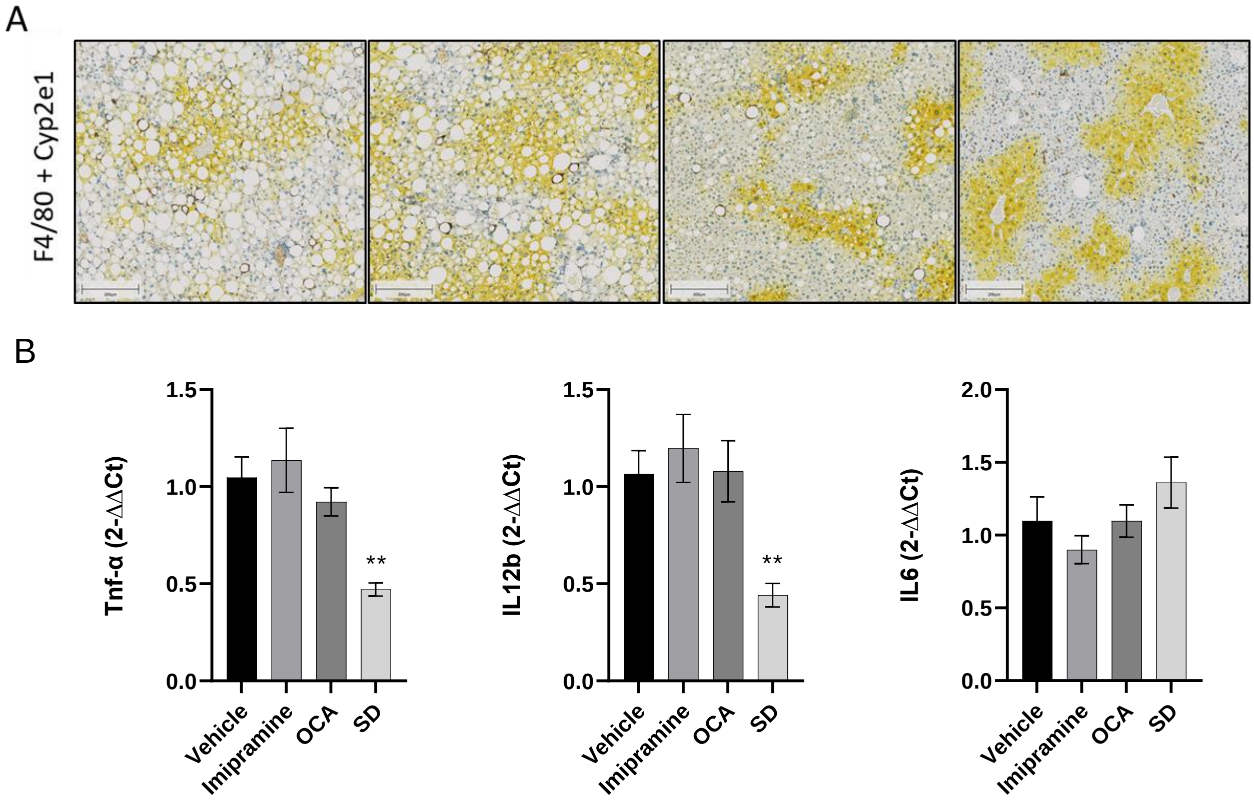

Figure 3.23. Macrophage crown-like structures and proinflammatory cytokine expression after WD interventions. A. Co-staining of F4/80 for macrophages and Cyp2e1 for pericentral hepatocytes shows macrophage localization in the midzonal/periportal liver compartment and a disappearance of crown-like structure formation after SD intervention. **B.** SD group shows decreasing relative expression of Tnf-α and IL12b compared to the vehicle group. The data are presented as means ± SEM of at least 9 biological replicates. **P<0.01. Scale bars: 200 µm. Tnf-α: tumor necrosis factor α; IL12b: interleukin 12b; IL6: interleukin 6; SD: standard diet.

In order to evaluate the level of cell death after NAFLD interventions, western blot analysis was performed using antibodies against Caspase-3 (apoptosis marker) and MLKL (necroptosis marker). As shown before in the NAFLD mouse model, necroptosis but no apoptosis was activated in the livers after WD feeding. Interestingly, all of the interventions decreased the degree of necroptosis compared to the vehicle-treated mice, shown as decreasing MLKL band sizes (Fig. 3.24).

Next, the accumulation of hepatic stellate cells after interventions was studied by desmin staining. Interestingly, the accumulation decreased after each intervention, nevertheless, the change was strongest in the SD group (Fig. 3.25). In line with this, less collagen content was seen after the interventions compared to the vehicle group (Fig. 3.25).

In order to investigate the influence of the intervention on canalicular morphology, liver sections were stained against CD13. As expected, the vehicle group showed small CD13-positive segments inside the hepatocytes, demonstrating the presence of macropinocytotic vesicles. Interestingly, segmentation of the canalicular network decreased in both imipramine and SD groups. In contrast, OCA treatment did not reduce the segmentation of the canalicular network, but led to a heavy branching of the bile canaliculi, which was not observed in the other intervention groups or in the vehicle group (Fig. 3.26).

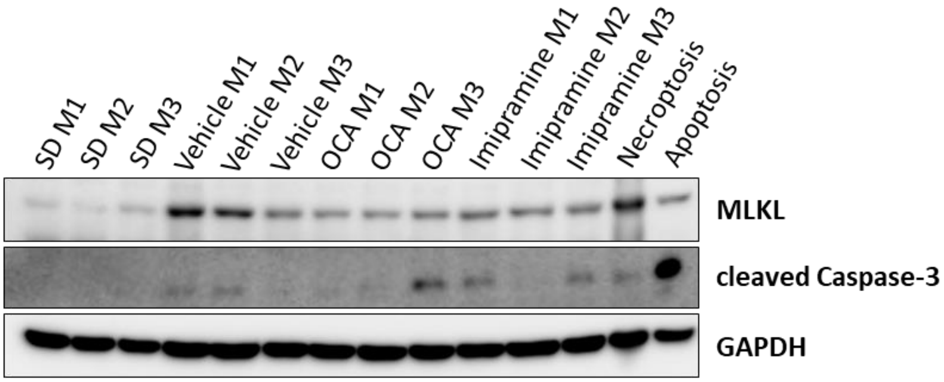

Figure 3.24. NAFLD interventions decrease liver cell death. Western blot of liver tissue samples showing an activation of necroptotic (MLKL and RIP3K) but not apoptotic (cleaved Caspase-3) cell death pathway after NAFLD interventions. The degree of necroptosis decreased after interventions. The last two loadings are positive controls for necroptosis and apoptosis. MLKL: mixed lineage kinase domain-like protein; GAPDH: Glyceraldehyde 3-phosphate dehydrogenase, housekeeping gene; SD: standard diet; OCA: obeticholic acid; M1-3: mouse number 1-3.

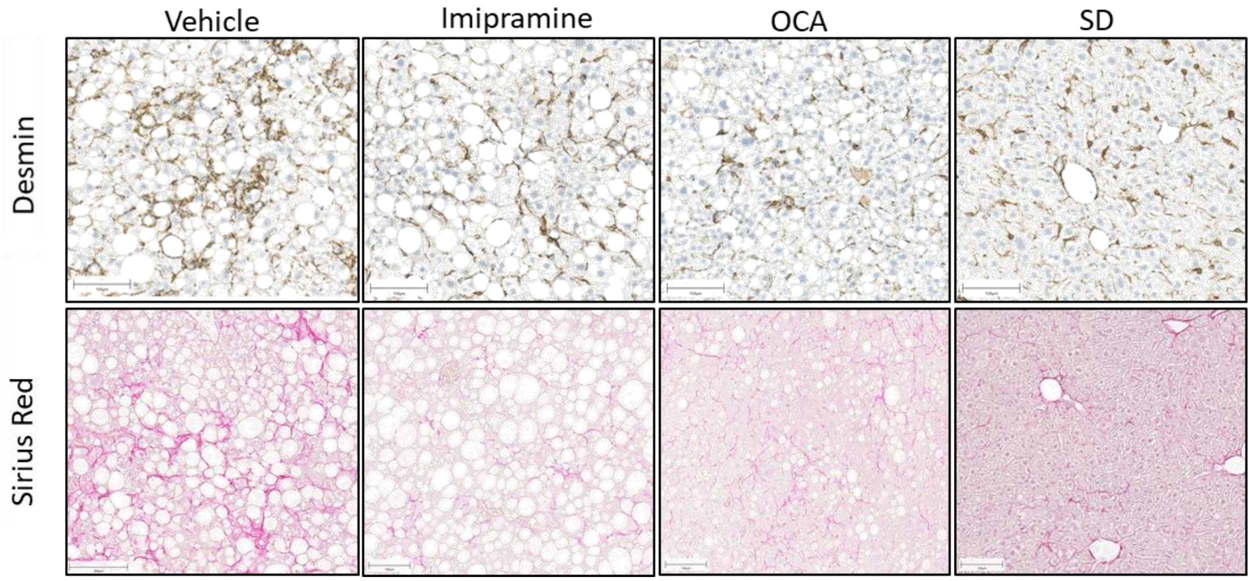

Figure 3.25. Decreasing stellate cell accumulation and fibrosis after NAFLD interventions. Representative images of desmin and Sirius Red staining showing decreased stellate cell accumulation and fibrosis after interventions compared to the vehicle treatment. Scale bars: 100 µm. OCA: obeticholic acid; SD: standard diet.

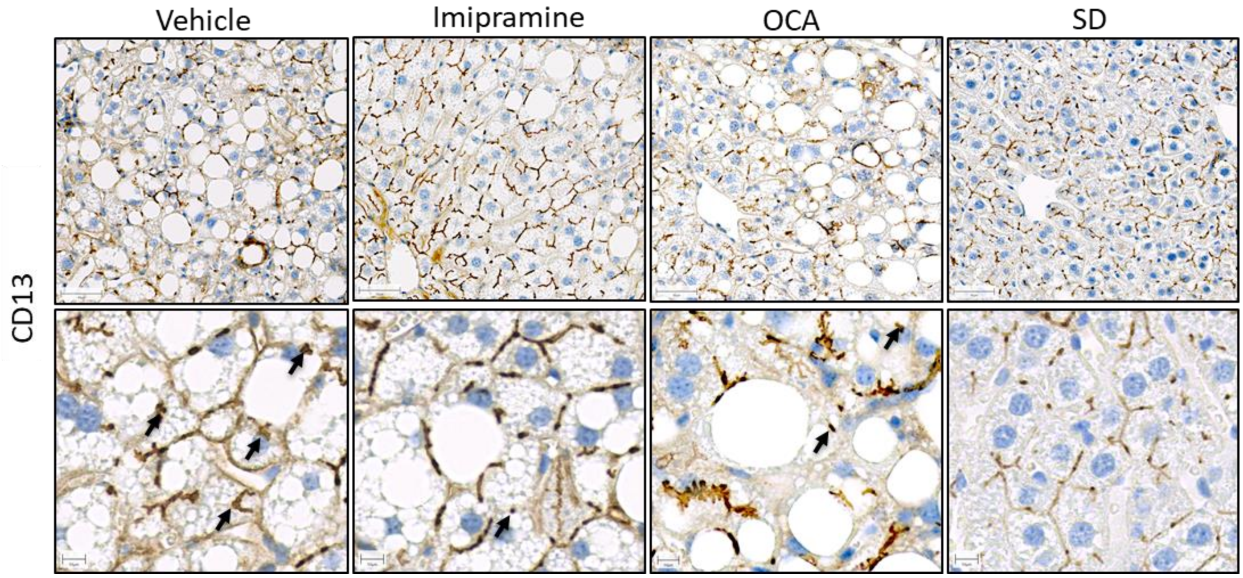

Figure 3.26. Canalicular network segmentation after NAFLD interventions. Representative images showing a decreasing number of CD13-positive segments in imipramine and SD groups, indicated as black arrows. OCA treatment did not reduce the number of the CD-13 positive segments and led to branching of bile canaliculi. Scale bars: 50 µm (upper panel) and 10 µm (lower panel, zoom-in). CD13: bile canaliculi; OCA: obeticholic acid; SD: standard diet.

To study the effect of the NAFLD interventions on bile acid synthesis and transport, RT-qPCR was run to determine the changes in bile acid transporter (Ntcp, Oatp, Bsep, Mrp2, Mrp3, Mrp4) and Cyp7a1 expressions (Fig. 3.27). Imipramine treatment increased the expression of sinusoidal uptake transporter Ntcp compared to the vehicle group but did not affect the expression of Oatp. Correspondingly, the expression of apical transporter Mrp2 increased but no change was observed in the other apical transporter Bsep. In addition, expression of both of the sinusoidal export transporters Mrp3 and Mrp4 was upregulated. The effect of OCA treatment on sinusoidal uptake transporters was comparable to the changes following imipramine treatment: upregulation of Ntcp expression but no change in Oatp expression compared to the vehicle-treated mice. Furthermore, OCA increased Bsep expression but did not significantly affect Mrp2 levels. In contrast to imipramine group, OCA decreased the expression of Mrp3, whereas there was no effect on Mrp4. In addition, several changes were seen in the SD group where the diet switch increased the expression of Ntcp, Oatp, Bsep, Mrp2, and Mrp3 compared to the vehicle-treated mice. Only Mrp4 expression stayed on the same level with the vehicle group. Furthermore, Cyp7a1 levels were measured, showing an increase in imipramine and SD group. In contrast, OCA decreased the expression of Cyp7a1 down to 0.7-fold, however remaining statistically insignificant (Fig. 3.27).

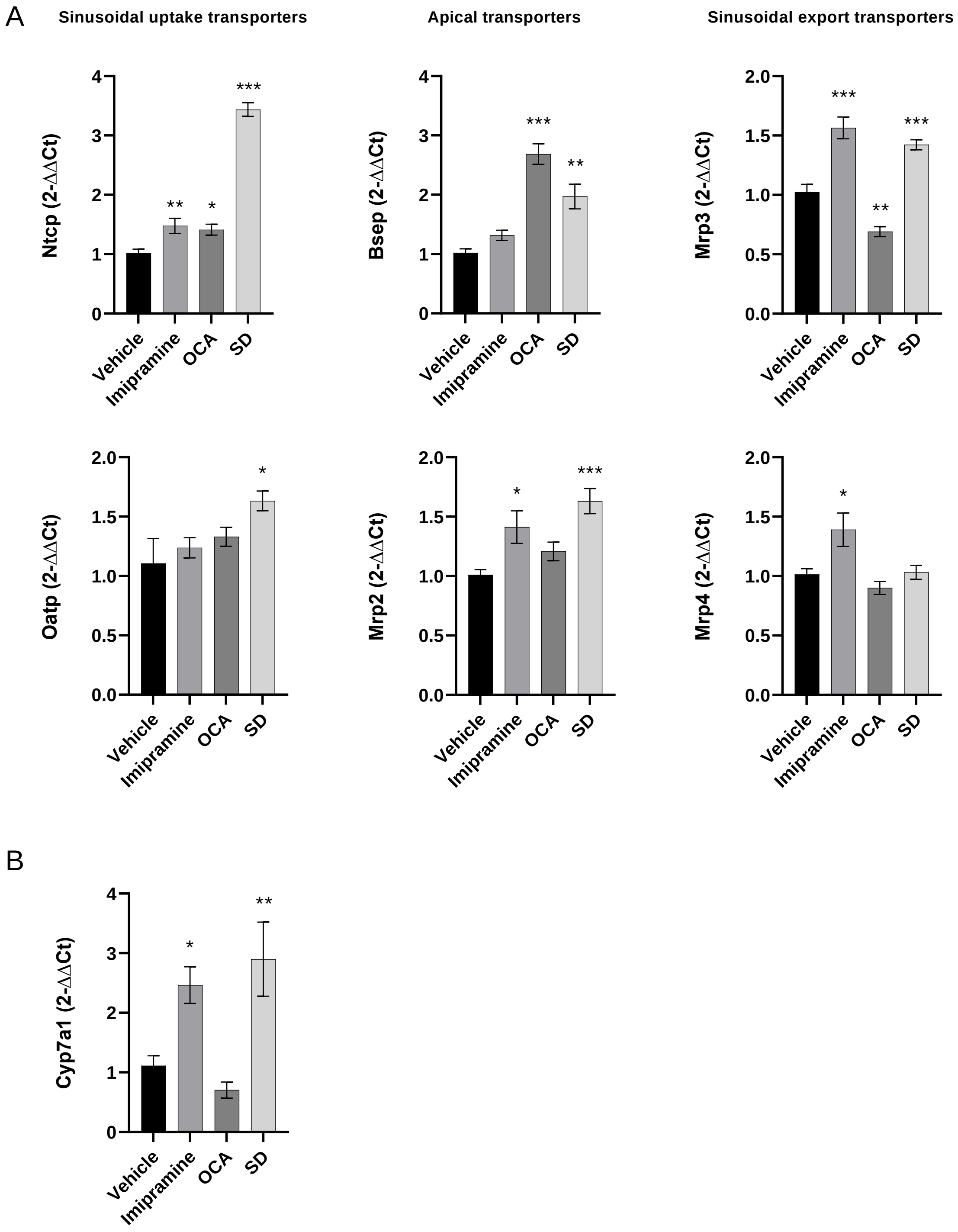

Figure 3.27. NAFLD interventions lead to altered bile acid transporter and Cyp7a1 expression. A. Imipramine, OCA, and SD interventions increased the expression of sinusoidal uptake and apical transporters, whereas the expression of sinusoidal export transporters increased after imipramine and SD but decreased after OCA treatment. **B.** Cyp7a1 expression increased both in imipramine and SD groups but did not significantly change in OCA group. *P<0.05 **P<0.01; ***P<0.001. The data are presented as means ± SEM from at least nine biological replicates. OCA: Obeticholic acid; SD: standard diet.

In order to see how the NAFLD interventions affect bile acid accumulation, bile acids were measured in bile and in liver tissue. The sum of bile acids in bile decreased after OCA treatment, whereas other interventions did not affect the levels. Interestingly, the sum concentration of bile acids in the liver tissue decreased in all of the intervention groups compared to the vehicle group (Fig. 3.28)

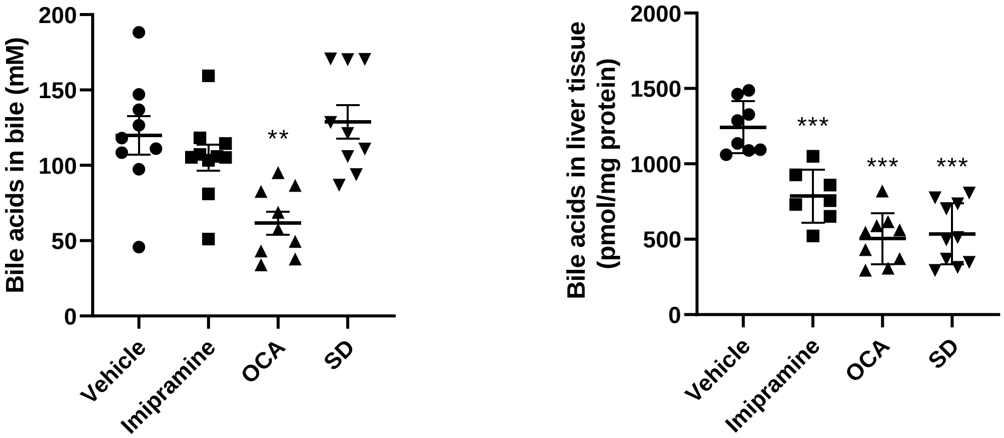

Figure 3.28. Bile acid accumulation after WD interventions. Total sum of bile acids in bile decreased after OCA treatment, whereas all of the interventions lowered the sum of bile acids in liver tissue compared to the vehicle treatment. **P<0.01; ***P<0.001. The data are presented as means ± SEM from at least seven biological replicates. OCA: obeticholic acid; SD: standard diet.

4 DISCUSSION

Non-alcoholic fatty liver disease (NAFLD) is the most common chronic liver disease in Western countries with an average worldwide prevalence of approximately 25 % (Chalasani et al., 2018; Younossi et al., 2016). An initially benign steatosis progresses in 20-30 % of cases to non-alcoholic steatohepatitis (NASH) and in some cases eventually to cirrhosis and hepatocellular carcinoma (HCC). Currently, there are no approved drugs for treatment of NASH (Friedman, Neuschwander-Tetri, et al., 2018). Therefore, NAFLD represents the second most common indicator for liver transplantation after hepatitis C (Chalasani et al., 2018). The main reason for the so far limited success in finding therapeutic targets for NASH is the poor understanding of the driving molecular mechanisms behind it. Nevertheless, a number of emerging therapies are currently evaluated in clinical trials (Chalasani et al., 2018). One drug that has advanced to phase 3 clinical trials is the FXR agonist obeticholic acid (OCA) (Ratziu et al., 2019). In a phase 2 study, OCA improved the histological features in NASH patients and reduced the levels of liver damage markers in the blood (Neuschwander-Tetri et al., 2015). However, the mechanism of how this anti-cholestatic drug is effective in NASH patients is not fully understood.

A novel and clinically relevant finding of this thesis is the identification of the link between NAFLD and cholestasis. In a mouse model of NAFLD progression, it was identified how NAFLD progresses to HCC in six stages. These stages are (1) benign steatosis, (2) macrophage crown-like structure formation, (3) macropinocytosis of bile, (4) ductular reaction, (5) dedifferentiation and functional shutdown, and (6) tumor formation (Box; 1 Fig. 1). Particularly the stage 3, namely macropinocytosis of bile, was discovered in the present thesis. In this stage, a retrograde vesicular uptake of bile from bile canaliculi to hepatocytes occur. These vesicles become leaky in the hepatocytes, thereby leading to an accumulation of the toxic bile acids which triggers inflammation, fibrogenesis, and further progression of NAFLD. Interestingly, therapeutic exploitation of this novel discovery by targeting macropinocytosis significantly ameliorated the progression of NAFLD. In the following chapters, the discovery and the clinical implications of this novel macropinocytotic mechanism will be discussed.

Box 1. NAFLD-HCC stage-transition concept

Stage 1 – benign steatosis: Lipid droplets of increasing size appear inside the hepatocytes. No major infiltration of immune cells and no significant increase in liver damage markers is observed.

Stage 2 – macrophage crown-like structure formation: Macrophages infiltrate in the liver and form crown-like structures around steatotic hepatocytes. Liver damage markers are increased.

Stage 3 – macropinocytosis of bile: Hepatocytes take up bile-filled vesicles from the bile canaliculi, followed by leakiness of the vesicles inside the hepatocytes, increase of intracellular bile acid concentrations, and hepatocyte death. Based on specific inhibitor imipramine, the uptake mechanism was identified as macropinocytosis and it was showed to be dependent on macrophage accumulation.

Stage 4 – ductular reaction: CK19-positive ductular structures infiltrate the liver lobules.

Stage 5 – dedifferentiation and functional shutdown: Hepatocytes start lose their specific functions such as changes in lobular zonation and specific enzyme expressions.

Stage 6 – tumor formation: The established NAFLD mouse model leads to formation of tumor nodules in 80 % of the mice between weeks 36 and 54 of WD feeding.

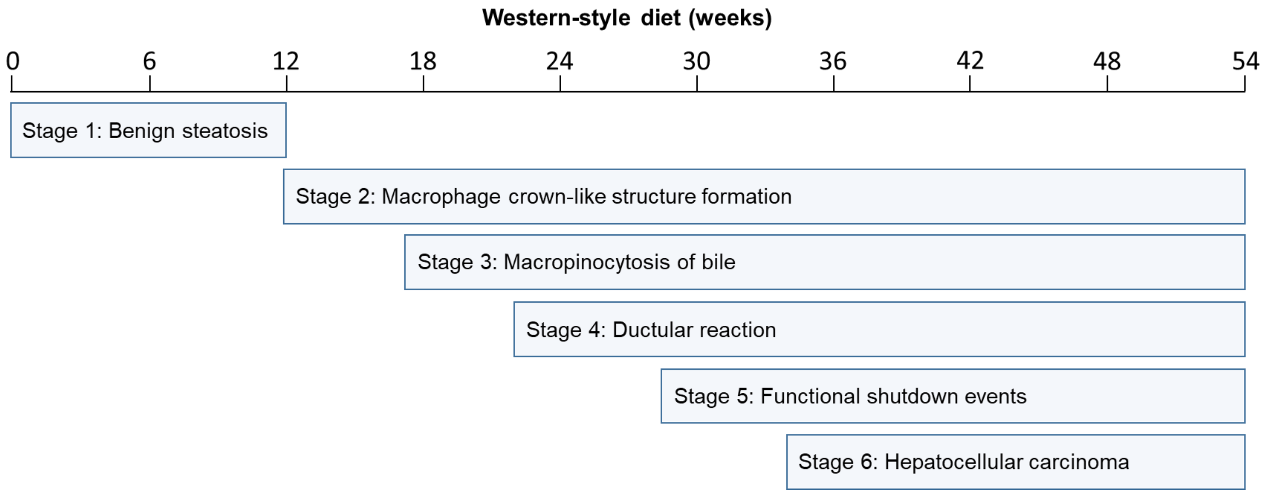

Figure 4.1. Stages of NAFLD progression in the mouse model.

4.1 Stages of NAFLD progression

Establishment of the NAFLD mouse model identified six distinguishable NAFLD progression stages that are summarized in Box 4.1 and Fig. 4.1. During the first 12 weeks of WD feeding, the mice were developing benign steatosis which has been previously characterized as an accumulation of lipid droplets inside the hepatocytes, leading to steatosis of >5 % of hepatocytes. In addition to fat accumulation, no signs of liver damage are present in benign steatosis (Chalasani et al., 2018; Mitra et al., 2020). At the second stage starting at 12 weeks of WD feeding, macrophages started to infiltrate into the liver tissue and form crown-like structures around the steatotic hepatocytes. This phenomenon has been characterized previously both in mice and humans (Ioannou et al., 2013; Itoh et al., 2013, 2017) and it is believed to increase hepatic inflammation during NAFLD progression by increasing proinflammatory cytokine production (Gadd et al., 2014; Itoh et al., 2013; Tosello-Trampont et al., 2012). Supporting this theory, elevated liver damage markers were accompanying the macrophage infiltration at stage 2 in the here established NAFLD mouse model.

A newly identified stage of NAFLD in the present thesis was stage 3, macropinocytosis of bile, which will be discussed in detail in chapter 4.2. Briefly, starting between 12 and 18 weeks of WD feeding, the bile was observed to become taken up by hepatocytes, leading to bile acid accumulation in the liver tissue and hence to increasing liver damage. This vesicular regurgitation of bile was further identified as macropinocytosis and it is a potent mechanism driving NAFLD progression. In the fourth stage of NAFLD progression, novel bile ducts were observed to infiltrate the liver. These newly formed cholangiocyte-derived bile ductules, also named ductular reaction, have been reported previously in human NAFLD and are presumed to promote portal fibrogenesis and NAFLD progression (Gadd et al., 2014; Richardson et al., 2007). All the previous liver-damage promoting stages eventually lead to stage 5, where the liver dedifferentiates and undergoes functional shutdown events. This process has been previously reported in Ghallab et al. (2019b) describing changes in zonation-specific enzyme expression in chronic liver disease. At the final stage 6 between weeks 36 and 54, tumor nodule formation was observed in the majority of mice, indicating development of hepatocellular carcinoma.

4.2 Macropinocytosis of bile: a so far unrecognized mechanism of NAFLD progression

The novel finding of the current thesis was the discovery of macropinocytosis of bile from bile canaliculi into the hepatocytes. Pinocytosis is amongst phagocytosis and receptor-mediated endocytosis one of the three main endocytic uptake mechanism of mammalian cells (Fig. 4.2). Macropinocytosis, also called ‘cell drinking’, is defined functionally as the vesicular uptake of extracellular fluids. It produces vesicles with size of ≥0.2 µm. In contrast to phagocytosis which is an uptake mechanism for large, solid particles, macropinocytosis transports extracellular fluids and small solutes into the cell. Moreover, contrary to receptor-mediated endocytosis, no ligand-receptor binding is required and macropinocytosis can non-specifically be triggered by physical concentrations of different solutes such as growth factors or inflammatory cytokines (Bloomfield & Kay, 2016; Swanson, 2008; Swanson & Watts, 1995).

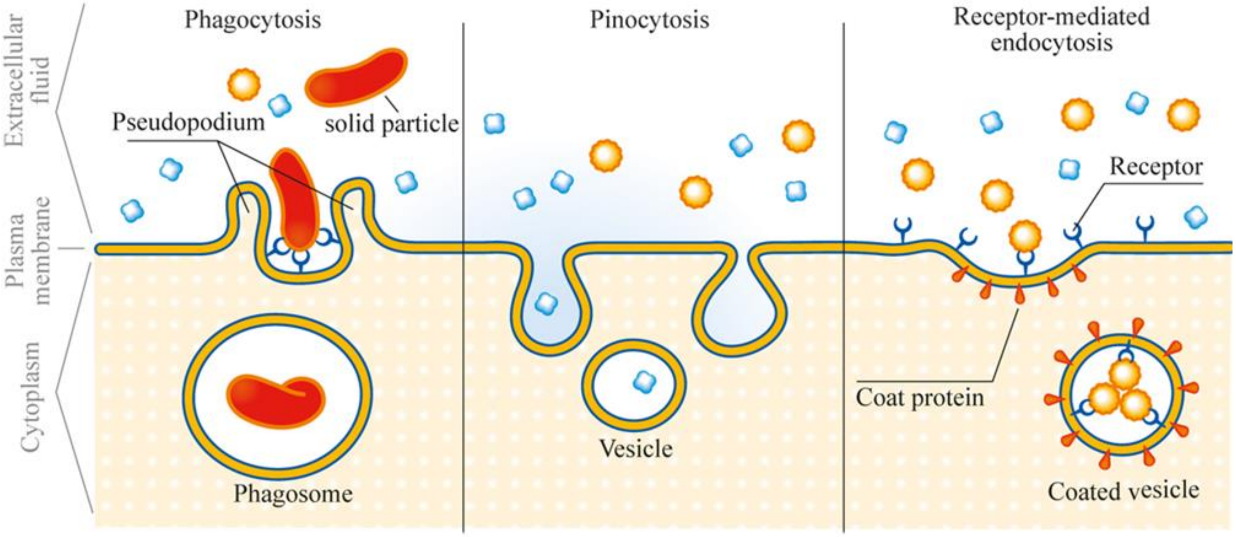

Figure 4.2. Mammalian cell uptake mechanisms. Phagocytosis is an uptake mechanism for large, solid particles, whereas pinocytosis is an uptake of extracellular fluids and small solutes. Receptor-mediated endocytosis is a specific mechanism requiring ligand-receptor binding. Figure from https://eng.thesaurus.rusnano.com/wiki/article2025.

Macropinocytosis has been shown to occur in several different cell types, such as macrophages (Wójciak-Stothard et al., 1998) and epithelial cells (Miyake et al., 2016). It serves multiple roles, for instance antigen presentation (Liu & Roche, 2015) and nutrient transport especially into cancer cells (Commisso et al., 2013). Macropinocytosis can be divided into induced and constitutive macropinocytosis, of which the more common form is induced macropinocytosis occurring in various cell types, where the cell responds to concentration changes of external stimulus. In contrast, constitutive macropinocytosis is involved in physiological processes such as antigen presentation. Unlike induced macropinocytosis, constitutive macropinocytosis is calcium-dependent and restricted to dendritic cells and macrophages (Canton et al., 2016). Based on the observations in the present mouse model, increasing bile acid concentration as well as inflammatory cytokines in NAFLD is presumed to trigger an actin-dependent process called membrane ruffling. The ruffles extend by actin filament assembly, leading to a formation of crater-like cups of the cell membrane. Eventually, the cup formation is followed by membrane fusion and fission, which results in formation of vesicle called macropinosome and its detachment from the cell membrane into the cytoplasm (Fig. 4.3) (Swanson, 2008).

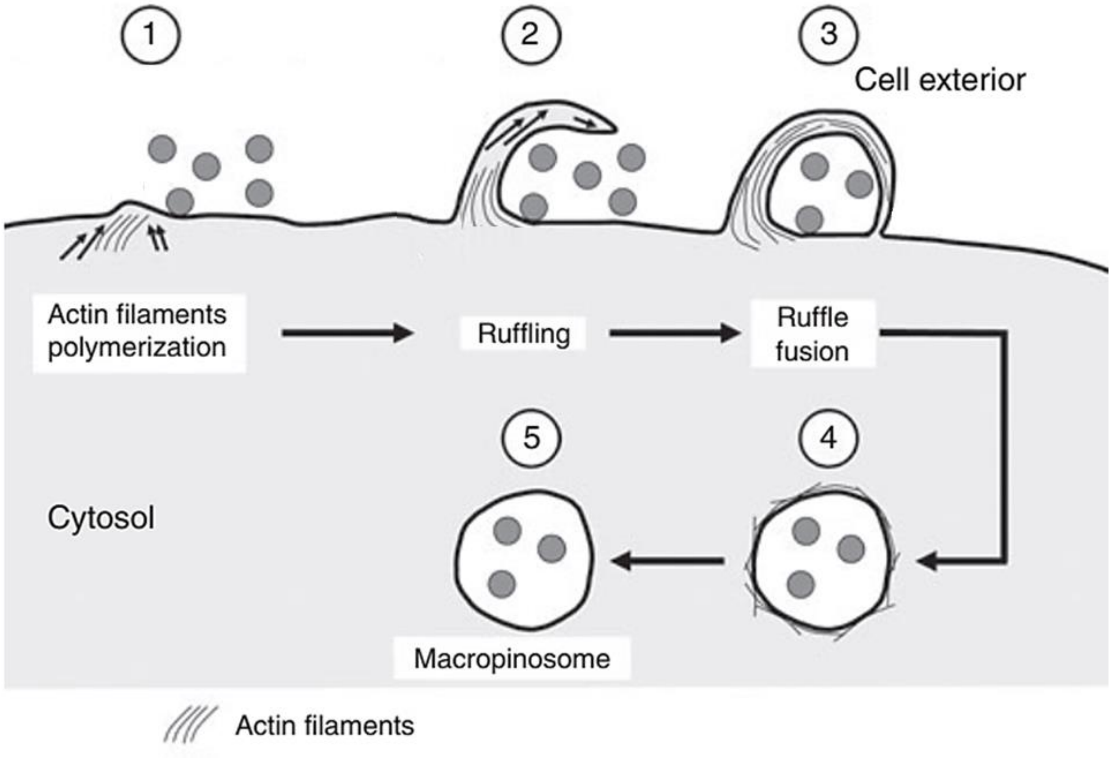

Figure 4.3. Schematic illustration of the stages of macropinocytosis. Membrane ruffling starts as actin filaments start to polymerize, forming a cup-like structure. The ruffles fuse with the plasma membrane, resulting in macropinosome formation and internalization into the cytosol. Figure modified from El-Sayed & Harashima, 2013.

Discovery of this novel macropinocytosis stage during NAFLD progression in the present was possible because of using functional intravital imaging. In this technique, intact mouse livers were imaged with two-photon microscopy using either appropriate fluorophores or reporter mice. Resolution is close to the theoretically possible 200 nm, and therefore allows imaging at subcellular level (Reif et al. 2017; Ghallab et al. 2019a; Jansen et al. 2017). In the current thesis, applying this technology to image transport of the bile acid analogue cholyl-lysyl-fluorescein (CLF) in the WD-fed mice allowed to discover the macropinocytosis stage.

In order to confirm the observed bile uptake mechanism as macropinocytosis and to distinguish it from other endocytic mechanisms, a macropinocytosis-specific inhibitor imipramine, as reported in Lin et al., (2018), was used. A single dose of imipramine efficiently blocked the vesicular regurgitation of bile in the WD-fed mice, confirming that the observed endocytic uptake mechanism was macropinocytosis. Bile macropinocytosis into the hepatocytes has several consequences in the NAFLD progression. At physiological concentrations lower than 25 µM, bile acids are beneficial and act as signal molecules (Wenling Chen et al., 2001). However, at concentrations higher than 50 µM, bile acids might trigger apoptosis (Schoemaker et al., 2004), and at concentrations above 200 µM they can promote inflammation (Allen et al., 2011) and necrosis (Schoemaker et al., 2004). Ultimately, bile acids act as detergents at concentrations above 2000 µM (Schoemaker et al., 2004). In a healthy liver, bile acid concentrations are kept at less than 50 µM in hepatocytes, ensuring that no liver damage occurs (Fickert & Wagner, 2017; Hassan et al., 2018) However, as shown in this thesis, macropinocytosis of bile led to elevated concentrations of bile acids in the liver tissue, causing increasing liver damage as shown by elevated liver enzymes, accumulation of inflammatory cells, activation of necroptosis, and increasing fibrosis. Importantly, these results form a link between bile acid accumulation and NAFLD progression, and may explain why anti-cholestatic drugs such as OCA are efficient in NAFLD treatment. Based on these observations, this novel mechanism of bile macropinocytosis is likely to be an important driving force of NAFLD progression.

4.3 Targeting macropinocytosis prevents NAFLD progression

In order to further study the role of bile acid macropinocytosis in the NAFLD progression, an intervention experiment with imipramine, OCA, or with switching WD to SD was performed. As a result, imipramine decreased the levels of liver enzymes ALT and ALP and prevented the increase of AST. In addition, it decreased the accumulation of bile acids in the liver tissue and restored Cyp7a1 as well as several bile acid transporter expressions, indicating improvement in bile acid synthesis and transport. Importantly, liver steatosis of imipramine-treated mice did not decrease compared to the vehicle-treated mice. It is well known that bile acids are important in emulsification and catabolism of lipids (Staels & Fonseca, 2009). Thus, as the bile acid uptake from bile canaliculi into the steatotic hepatocytes was blocked by imipramine, the lipid catabolism of the cells might have become disrupted, leading to lipid preservation within the hepatocytes.

In contrast to imipramine, OCA treatment efficiently decreased the liver steatosis, which is in line with previous reports (Neuschwander-Tetri et al., 2015). Moreover, it decreased bile acid accumulation both in bile and in liver tissue, and recovered Bsep and Ntcp expression. The systemic effect of OCA is based on its FXR agonism. Binding of OCA to FXR results in suppression of Cyp7a1 and hence decreasing bile acid synthesis (Manne & Kowdley, 2019). However, OCA did not influence the bile macropinocytosis as shown in the liver histology, where CD13 positive segments were still present. In this case, bile acids are presumably taken back from bile canaliculi into the hepatocytes, which may explain the decrease in lipid accumulation in the liver tissue, whereas the liver enzyme levels remain unchanged. Notably, OCA caused heavy pruritus in some of the mice, leading to excessive scratching and wound formation. This side effect of OCA has been reported previously in human patients and it is known to be dose-dependent (Hirschfield et al., 2015; Manne & Kowdley, 2019; Nevens et al., 2016).

Switching WD to SD resulted led to significant improvement in the NAFLD stage. The diet switch decreased ALT and ALP levels, remarkably improved the liver steatosis, and decreased the infiltration of inflammatory cells as well as TNF-α and IL12b expression. Moreover, no CD13 positive vesicles were observed in the liver tissue histology, indicating restrain in bile macropinocytosis. Consequently, bile acid accumulation in liver tissue decreased and bile acid transporters and Cyp7a1 levels were restored.

Currently, there are no approved drugs for NAFLD treatment. Nevertheless, several pharmacological compounds are in clinical trials, including OCA, an FXR agonist; Elafibranor, an activator of peroxisome proliferator-activated receptors (PPARs); and Cenicriviroc, a dual antagonist of C–C chemokine receptors (Friedman et al., 2018; Neuschwander-Tetri et al., 2015; Pydyn et al., 2020). In the future, identification of different NAFLD stages may allow a stage-dependent therapy (Table 4.1). At stage 1, the benign steatosis with no significant liver inflammation or damage is likely to improve by reaching an optimal diet and physical training. However at stage 2, anti-inflammatory strategies may be beneficial in order to decrease the liver inflammation derived from accumulation of macrophages and production of proinflammatory cytokines. At stage 3, bile acid synthesis and accumulation should be targeted. As shown in the present work, blocking of bile macropinocytosis with pharmacological compounds such as imipramine may be beneficial in preventing the progression of NAFLD. In addition, FXR agonists such as OCA may be valuable at stage 3 in order to reduce bile acid synthesis and hence bile acid accumulation in the liver tissue. At stage 4, choleretic compounds such as nor-Ursodeoxycholic acid (nor-UDCA) may help by diluting the bile, increasing the bile duct flushing, and protecting cholangiocytes from toxic bile acids (Halilbasic et al., 2017). At stage 5, similar bile-acid limiting strategies may apply. However, the relevance of these treatments is yet to be tested.

Table 4.1. Stage-dependent treatment strategy of NAFLD

Stage of NAFLD to HCC transition	**Possible preventive measures**				
	Diet	Anti-inflammatories	Inhibition of macropinocytosis	FXR agonists	Choleresis (e.g. nor-UDCA)
(1) Benign steatosis	**X**				
(2) Macrophage crowns	**X**	**X**			
(3) Macropinocytosis of bile	**X**	**X**	**X**	**X**	
(4) Ductular reaction	**X**	**X**	**X**	**X**	**X**
(5) Functional shutdown	**X**	**?**	**?**	**?**	**?**

In the present work, only one bile macropinocytosis blocking drug was tested. The tested compound, imipramine, was previously reported to inhibit induced but not constitutive macropinocytosis without affecting other endocytic mechanisms or inducing cytotoxic effects (Lin et al., 2018). As another advantage of imipramine, blocking of only induced macropinocytosis allows physiological macropinocytotic processes such as antigen presentation to occur. In the study of Lin et al. (2018), imipramine was found to inhibit the membrane ruffling in response to stimulus, hence preventing the macropinosome formation. In the future, testing other macropinocytosis-blocking drugs in intervention of NAFLD progression may be beneficial. Lin et al. (2018) reported several other macropinocytosis-blocking agents (Table 4.2), of which phenoxybenzamine and vinblastine in addition to imipramine potently inhibited macropinocytosis without cytotoxic effects or affecting other endocytic pathways. Testing the clinical relevance of these drugs may provide a broad overview of the role of macropinocytosis in NAFLD and contribute to NAFLD recovery.

Table 4.2. Identified macropinocytosis-blocking agents. Table modified from Lin et al., 2018.

Drug	Class	IC_{50}	IC_{100}
Imipramine	Tricyclic antidepressant	131 ± 26.3 nM	5 µM
Flubendazole	Anthelmintic	240 ± 33.8 nM	9 µM
Terfenadine	Histamine H_1 receptor antagonist	267 ± 49.1 nM	5 µM
Itraconazole	Antifungal medicine	106 ± 10.3 nM	1 µM
Phenoxybenzamine	α-Adrenergic antagonist	43.8 ± 10.5 nM	5 µM
Vinblastine	Microtubule formation inhibitor	2.2 ± 0.7 pM	2 nM
Auranofin	Anti-rheumatoid arthritis agent	733 ± 191 nM	5 µM

As presented in the current work, both imipramine and OCA inhibited the progression of NAFLD but the observed cellular level mechanisms and consequences differed from each other. Thus, the future aim is to use a combination of imipramine and OCA in NAFLD treatment to achieve the beneficial effects of both drugs and minimize the unwanted side effects. As shown in the present study, imipramine decreased the level of liver damage indicated by decreased liver enzymes levels and cell death. However, no changes in liver steatosis were observed. The benefit of combining imipramine with OCA could theoretically be a decrease in liver damage level as well as in liver steatosis, which was reached after OCA treatment. In addition, combining imipramine and OCA may enable lowering the dosage of OCA in order to reduce the pruritus side effect. Furthermore, in the future it is essential to determine the specific time window when macropinocytosis targeting is effective in preventing NAFLD progression. In the current study, the treatment was started at the early stage of bile macropinocytosis. However, it is important to test the later time windows as well to understand the relevance of macropinocytosis and the efficacy of its treatment later during NAFLD progression.

4.4 Clinical translation

In the current thesis, a mouse model of NAFLD progression was successfully established. The mouse model recapitulates features of human NAFLD including hepatocyte steatosis, liver inflammation and damage, ductular reaction, fibrosis, and eventually tumor nodule formation. Despite the remarkable similarities with human NAFLD, an interesting feature of the NAFLD mouse model is the observed zonation of lipid droplets. In the benign steatosis of the mouse model, the lipids started to accumulate mainly in the periportal and midzonal compartments of the liver lobule. In the later stages of NAFLD progression, lipid droplets became scattered throughout the liver lobule, nevertheless, the largest lipid droplets were found in the periportal and midzonal area, whereas the pericentral steatosis consisted of mainly smaller lipid droplets, i.e. microvesicular steatosis. This predominantly midzonal and periportal steatosis has been previously reported in C57Bl/6N mice (Schwen et al., 2016). In contrast, in adult human NAFLD patients liver steatosis mainly occurs in the pericentral compartment of the liver lobule (Chalasani et al., 2008; Kleiner & Makhlouf, 2016; Zhuang et al., 2020). However, lipid distribution in pediatric NAFLD features the pattern observed in the mouse model, occurring mainly in the periportal area. Moreover, unlike in adult NAFLD, microvesicular steatosis can be present in the pericentral compartment of the liver lobule (Fitzpatrick & Dhawan, 2019; Kleiner & Makhlouf, 2016; Nobili et al., 2016), similarly as observed in the NAFLD mouse model.

The reasons for the differentiating steatosis pattern between adults and children is rather unclear, nevertheless, it is possible that the activity of Hedgehog and Wnt/β-catenin signaling pathways are playing a role in determining the pattern. The Hedgehog pathway is the most active in the periportal compartment of the liver lobule (Swiderska-Syn et al., 2013). It is connected to the development of portal fibrosis in the pediatric NAFLD, and its activity decreases in the adulthood (Africa et al., 2018; Swiderska-Syn et al., 2013). In contrast, Wnt/β-catenin signaling pathway is the most active in the pericentral area and its activity increases in the adulthood (Africa et al., 2018). Interestingly, β-catenin knockout mice have been reported to suffer from periportal steatosis after feeding with high-fat diet, whereas hepatocyte-specific β-catenin transgenic mice developed pericentral steatosis (Behari et al., 2014). Moreover, genetic background of the mice has been shown to affect β-catenin activation. The study from Kararigas et al. (2014) showed that C57BL/6N mice had an attenuated activation of β-catenin in the cardiomyocytes compared to C57BL/6J mice. These findings suggest that the differences in the lipid droplet accumulation pattern in the NAFLD mouse model and in adult NADFLD patients may stem from differential activation of Hedgehog and Wnt/β-catenin signaling pathways.

In the current work, macropinocytosis of bile was observed in the NAFLD mouse model by intravital imaging and it was connected to the elevated levels of bile acids in the liver tissue. In humans, the bile macropinocytosis has not been reported previously. However, bile acids have shown to increase in human NAFLD both in serum (Ferslew et al., 2015; N. Jiao et al., 2018) and in the liver tissue (Aranha et al., 2008), suggesting a disturbance in the bile acid production and transport. An interesting finding in the current thesis was the presence of CD13-positive vesicles in the liver tissue of human NAFLD patients. Similar CD13-positive segments were found in the mouse model, representing the macropinocytotic vesicles. These data suggest that bile macropinocytosis may be a key mechanism in NAFLD progression, promoting the chronic liver injury. In the future, the presence of macropinocytotic vesicles and their connection to bile acid accumulation and liver injury should be carefully studied in NAFLD patients. Targeting macropinocytosis may provide an attractive therapeutic target to intervene the NAFLD progression in human patients.

REFERENCES

Abenavoli, L., Falalyeyeva, T., Boccuto, L., Tsyryuk, O., & Kobyliak, N. (2018). Obeticholic acid: A new era in the treatment of nonalcoholic fatty liver disease. *Pharmaceuticals*, *11*(4). https://doi.org/10.3390/ph11040104

Africa, J., Behling, C. A., Brunt, E. M., Zhang, N., Luo, Y., Wells, A., Hou, J., Belt, P. H., Kohil, R., Lavine, J. E., Molleston, J. P., Newton, K., Whitington, P. F., Schwimmer, J. B., Abrams, S. H., Barlow, S., Himes, R., Krisnamurthy, R., Maldonado, L., … Fowler, K. (2018). In Children With Nonalcoholic Fatty Liver Disease, Zone 1 Steatosis Is Associated With Advanced Fibrosis. *Clinical Gastroenterology and Hepatology*, *16*(3), 438-446.e1. https://doi.org/10.1016/j.cgh.2017.02.030

Allen, K., Jaeschke, H., & Copple, B. L. (2011). Bile acids induce inflammatory genes in hepatocytes: A novel mechanism of inflammation during obstructive cholestasis. *American Journal of Pathology*, *178*(1), 175–186. https://doi.org/10.1016/j.ajpath.2010.11.026

Alves-Bezerra, M., & Cohen, D. E. (2018). Triglyceride metabolism in the liver. *Comprehensive Physiology*, *8*(1), 1–22. https://doi.org/10.1002/cphy.c170012

Aranha, M. M., Cortez-Pinto, H., Costa, A., Da Silva, I. B. M., Camilo, M. E., De Moura, M. C., & Rodrigues, C. M. P. (2008). Bile acid levels are increased in the liver of patients with steatohepatitis. *European Journal of Gastroenterology and Hepatology*, *20*(6), 519–525. https://doi.org/10.1097/MEG.0b013e3282f4710a

Asrani, S. K., Devarbhavi, H., Eaton, J., & Kamath, P. S. (2019). Burden of liver diseases in the world. *Journal of Hepatology*, *70*(1), 151–171. https://doi.org/10.1016/j.jhep.2018.09.014

Barrows, B. R., & Parks, E. J. (2006). Contributions of Different Fatty Acid Sources to Very Low-Density Lipoprotein-Triacylglycerol in the Fasted and Fed States. *The Journal of Clinical Endocrinology & Metabolism*, *91*(4), 1446–1452. https://doi.org/10.1210/jc.2005-1709

Bedossa, P., & Paradis, V. (2003). Liver extracellular matrix in health and disease. *The Journal of Pathology*, *200*(4), 504–515. https://doi.org/10.1002/path.1397

Behari, J., Li, H., Liu, S., Stefanovic-Racic, M., Alonso, L., O’Donnell, C. P., Shiva, S., Singamsetty, S., Watanabe, Y., Singh, V. P., & Liu, Q. (2014). β-catenin links hepatic metabolic zonation with lipid metabolism and diet-induced obesity in mice. *American Journal of Pathology*, *184*(12), 3284–3298. https://doi.org/10.1016/j.ajpath.2014.08.022

Birchmeier, W. (2016). Orchestrating Wnt signalling for metabolic liver zonation. *Nature Cell Biology*, *18*(5), 463–465. https://doi.org/10.1038/ncb3349

Bittencourt, P. L., Farias, A. Q., & Terra, C. (2015). Renal failure in cirrhosis: Emerging concepts. *World Journal of Hepatology*, *7*(21), 2336–2343. https://doi.org/10.4254/wjh.v7.i21.2336

Bloomfield, G., & Kay, R. R. (2016). Uses and abuses of macropinocytosis. *Journal of Cell Science*, *129*(14), 2697–2705. https://doi.org/10.1242/jcs.176149

Bouwens, L., Baekeland, M., De, R., & Wisse, E. (1986). Quantitation, Tissue Distribution and Proliferation Kinetics of Kupffer Cells in Normal Rat Liver. *Hepatolo*, *6*(4), 718–722.

Boyer, J. L. (2013). Bile formation and secretion. *Comprehensive Physiology*, *3*(3), 1035–1078. https://doi.org/10.1002/cphy.c120027

Boyer, J. L., Trauner, M., Mennone, A., Soroka, C. J., Cai, S. Y., Moustafa, T., Zollner, G., Lee, J. Y., & Ballatori, N. (2006). Upregulation of a basolateral FXR-dependent bile acid efflux transporter OSTα-OSTβ in cholestasis in humans and rodents. *American Journal of Physiology - Gastrointestinal and Liver Physiology*, *290*(6). https://doi.org/10.1152/ajpgi.00539.2005

Brackhagen, L. (2020). *Bile acids as mediators of acetaminophen-induced hepatotoxicity*. Hochschule Hamm-Lippstadt.

Brunt, E. M., Janney, C. G., Di Bisceglie, A. M., Neuschwander-Tetri, B. A., & Bacon, B. R. (1999). Nonalcoholic steatohepatitis: A proposal for grading and staging the histological lesions. *American Journal of Gastroenterology*, *94*(9), 2467–2474. https://doi.org/10.1111/j.1572-0241.1999.01377.x

Canbay, A., Taimr, P., Torok, N., Higuchi, H., Friedman, S., & Gores, G. J. (2003). Apoptotic body engulfment by a human stellate cell line is profibrogenic. *Laboratory Investigation*, *83*(5), 655–663. https://doi.org/10.1097/01.LAB.0000069036.63405.5C

Canton, J., Schlam, D., Breuer, C., Gütschow, M., Glogauer, M., & Grinstein, S. (2016). Calcium-sensing receptors signal constitutive macropinocytosis and facilitate the uptake of NOD2 ligands in macrophages. *Nature Communications*, *7*. https://doi.org/10.1038/ncomms11284

Cassidy, W. M., & Reynolds, T. B. (1994). Serum lactic dehydrogenase in the differential diagnosis of acute hepatocellular injury. *Journal of Clinical Gastroenterology*, *19*(2), 118–121. https://doi.org/10.1097/00004836-199409000-00008

Cattley, R., & Popp, J. (2002). Liver. In *Handbook of Toxicologic Pathology* (pp. 187–225). Elsevier. https://doi.org/10.1016/B978-012330215-1/50032-6

Centis, E., Marzocchi, R., Di Domizio, S., Ciaravella, M. F., & Marchesini, G. (2010). The Effect of Lifestyle Changes in Non-Alcoholic Fatty Liver Disease. *Digestive Diseases*, *28*(1), 267–273. https://doi.org/10.1159/000282101

Chalasani, N., Wilson, L., Kleiner, D. E., Cummings, O. W., Brunt, E. M., & Ünalp, A. (2008). Relationship of steatosis grade and zonal location to histological features of steatohepatitis in adult patients with non-alcoholic fatty liver disease. *Journal of Hepatology*, *48*(5), 829–834. https://doi.org/10.1016/j.jhep.2008.01.016

Chalasani, N., Younossi, Z., Lavine, J. E., Charlton, M., Cusi, K., Rinella, M., Harrison, S. A., Brunt, E. M., & Sanyal, A. J. (2018). The diagnosis and management of nonalcoholic fatty liver disease: Practice guidance from the American Association for the Study of Liver Diseases. *Hepatology*, *67*(1), 328–357. https://doi.org/10.1002/hep.29367

Chen, Wei, Rock, J. B., Yearsley, M. M., Ferrell, L. D., & Frankel, W. L. (2014). Different collagen types show distinct rates of increase from early to late stages of hepatitis C-related liver fibrosis. *Human Pathology*, *45*(1), 160–165. https://doi.org/10.1016/j.humpath.2013.08.015

Chen, Wenling, Owsley, E., Yizeng, Y., Stroup, D., & Chiang, J. Y. L. (2001). Nuclear receptor-mediated repression of human cholesterol 7α-hydroxylase gene transcription by bile acids. *The Journal of Lipid Research*, *42*(9), 1402–1412.

Chen, X. M., O'Hara, S. P., & LaRusso, N. F. (2008). The immunobiology of cholangiocytes. *Immunology and Cell Biology*, *86*(6), 497–505. https://doi.org/10.1038/icb.2008.37

Cho, Y. S., Challa, S., Moquin, D., Genga, R., Ray, T. D., Guildford, M., & Chan, F. K. M. (2009). Phosphorylation-Driven Assembly of the RIP1-RIP3 Complex Regulates Programmed Necrosis and Virus-Induced Inflammation. *Cell*, *137*(6), 1112–1123. https://doi.org/10.1016/j.cell.2009.05.037

Commisso, C., Davidson, S. M., Soydaner-Azeloglu, R. G., Parker, S. J., Kamphorst, J. J., Hackett, S., Grabocka, E., Nofal, M., Drebin, J. A., Thompson, C. B., Rabinowitz, J. D., Metallo, C. M., Vander Heiden, M. G., & Bar-Sagi, D. (2013). Macropinocytosis of protein is an amino acid supply route in Ras-transformed cells. *Nature*, *497*(7451), 633–637. https://doi.org/10.1038/nature12138

Crosignani, A., Del Puppo, M., Longo, M., De Fabiani, E., Caruso, D., Zuin, M., Podda, M., Javitt, N. B., & Kienle, M. G. (2007). Changes in classic and alternative pathways of bile acid synthesis in chronic liver disease. *Clinica Chimica Acta*, *382*(1–2), 82–88. https://doi.org/10.1016/j.cca.2007.03.025

Dawson, P. A., Lan, T., & Rao, A. (2009). Thematic review series: Bile acids. Bile acid transporters. *Journal of Lipid Research*, *50*(12), 2340–2357. https://doi.org/10.1194/jlr.R900012-JLR200

Dixon, J. B., Bhathal, P. S., Hughes, N. R., & O'Brien, P. E. (2004). Nonalcoholic fatty liver disease: Improvement in liver histological analysis with weight loss. *Hepatology*, *39*(6), 1647–1654. https://doi.org/10.1002/hep.20251

Ebrahimkhani, M. R., Mohar, I., & Crispe, I. N. (2011). Cross-presentation of antigen by diverse subsets of murine liver cells. *Hepatology*, *54*(4), 1379–1387. https://doi.org/10.1002/hep.24508

El-Sayed, A., & Harashima, H. (2013). Endocytosis of gene delivery vectors: From clathrin-dependent to lipid raft-mediated endocytosis. *Molecular Therapy*, *21*(6), 1118–1130. https://doi.org/10.1038/mt.2013.54

Fang, S. (2017). Bile Acid Receptor Farnesoid X Receptor: A Novel Therapeutic Target for Metabolic Diseases. *Journal of Lipid and Atherosclerosis*, *6*(1), 1. https://doi.org/10.12997/jla.2017.6.1.1

Ferslew, B. C., Xie, G., Johnston, C. K., Su, M., Stewart, P. W., Jia, W., Brouwer, K. L. R., & Sidney Barritt, A. (2015). Altered Bile Acid Metabolome in Patients with Nonalcoholic Steatohepatitis. *Digestive Diseases and Sciences*, *60*(11), 3318–3328. https://doi.org/10.1007/s10620-015-3776-8

Fickert, P., & Wagner, M. (2017). Biliary bile acids in hepatobiliary injury – What is the link? *Journal of Hepatology*, *67*(3), 619–631. https://doi.org/10.1016/j.jhep.2017.04.026

Fitzpatrick, E., & Dhawan, A. (2019). Childhood and Adolescent Nonalcoholic Fatty Liver Disease: Is It Different from Adults? *Journal of Clinical and Experimental Hepatology*, *9*(6), 716–722. https://doi.org/10.1016/j.jceh.2019.05.005

Friedman, S. L., Neuschwander-Tetri, B. A., Rinella, M., & Sanyal, A. J. (2018). Mechanisms of NAFLD development and therapeutic strategies. *Nature Medicine*, *24*(7), 908–922. https://doi.org/10.1038/s41591-018-0104-9

Friedman, S. L., Ratziu, V., Harrison, S. A., Abdelmalek, M. F., Aithal, G. P., Caballeria, J., Francque, S., Farrell, G., Kowdley, K. V., Craxi, A., Simon, K., Fischer, L., Melchor-Khan, L., Vest, J., Wiens, B. L., Vig, P., Seyedkazemi, S., Goodman, Z., Wong, V. W. S., …

Lefebvre, E. (2018). A randomized, placebo-controlled trial of cenicriviroc for treatment of nonalcoholic steatohepatitis with fibrosis. *Hepatology*, *67*(5), 1754–1767. https://doi.org/10.1002/hep.29477

Gadd, V. L., Skoien, R., Powell, E. E., Fagan, K. J., Winterford, C., Horsfall, L., Irvine, K., & Clouston, A. D. (2014). The portal inflammatory infiltrate and ductular reaction in human nonalcoholic fatty liver disease. *Hepatology*, *59*(4), 1393–1405. https://doi.org/10.1002/hep.26937

Ghallab, A., Cellière, G., Henkel, S. G., Driesch, D., Hoehme, S., Hofmann, U., Zellmer, S., Godoy, P., Sachinidis, A., Blaszkewicz, M., Reif, R., Marchan, R., Kuepfer, L., Häussinger, D., Drasdo, D., Gebhardt, R., & Hengstler, J. G. (2016). Model-guided identification of a therapeutic strategy to reduce hyperammonemia in liver diseases. *Journal of Hepatology*, *64*(4), 860–871. https://doi.org/10.1016/j.jhep.2015.11.018

Ghallab, A., Hofmann, U., Sezgin, S., Vartak, N., Hassan, R., Zaza, A., Godoy, P., Schneider, K. M., Guenther, G., Ahmed, Y. A., Abbas, A. A., Keitel, V., Kuepfer, L., Dooley, S., Lammert, F., Trautwein, C., Spiteller, M., Drasdo, D., Hofmann, A. F., … Reif, R. (2019a). Bile Microinfarcts in Cholestasis Are Initiated by Rupture of the Apical Hepatocyte Membrane and Cause Shunting of Bile to Sinusoidal Blood. *Hepatology*, *69*(2), 666–683. https://doi.org/10.1002/hep.30213

Ghallab, A., Myllys, M., H. Holland, C., Zaza, A., Murad, W., Hassan, R., A. Ahmed, Y., Abbas, T., A. Abdelrahim, E., Schneider, K. M., Matz-Soja, M., Reinders, J., Gebhardt, R., Berres, M.-L., Hatting, M., Drasdo, D., Saez-Rodriguez, J., Trautwein, C., & G. Hengstler, J. (2019b). Influence of Liver Fibrosis on Lobular Zonation. *Cells*, *8*(12), 1556. https://doi.org/10.3390/cells8121556

Gordillo, M., Evans, T., & Gouon-Evans, V. (2015). Orchestrating liver development. *Development (Cambridge)*, *142*, 2094–2108. https://doi.org/10.1242/dev.114215

Grant, S. M., & Demorrow, S. (2020). Molecular Sciences Bile Acid Signaling in Neurodegenerative and Neurological Disorders. *International Journal of Molecular Sciences*, *21*(17). https://doi.org/10.3390/ijms21175982

Guzman, M., & Castro, J. (1989). Zonation of fatty acid metabolism in rat liver. *Biochemical Journal*, *264*(1), 107–113. https://doi.org/10.1042/bj2640107

Halilbasic, E., Steinacher, D., & Trauner, M. (2017). Nor-Ursodeoxycholic Acid as a Novel Therapeutic Approach for Cholestatic and Metabolic Liver Diseases. *Digestive Diseases*, *35*(3), 288–292. https://doi.org/10.1159/000454904

Hassan, R., Seddek, A.-L., & Ghallab, A. (2018). Pathophysiology of Cholestatic Liver Diseases: New Insights into the Mechanisms of Bile Infarct Formation. *SVU-International Journal of Veterinary Sciences*, *1*(2), 95–105.

Hernandez-Gea, V., & Friedman, S. L. (2011). Pathogenesis of Liver Fibrosis. *Review in Advance on Annu. Rev. Pathol. Mech. Dis*, *6*, 425–456. https://doi.org/10.1146/annurev-pathol-011110-130246

Hirschfield, G. M., Mason, A., Luketic, V., Lindor, K., Gordon, S. C., Mayo, M., Kowdley, K. V., Vincent, C., Bodhenheimer, H. C., Parés, A., Trauner, M., Marschall, H. U., Adorini, L., Sciacca, C., Beecher-Jones, T., Castelloe, E., Böhm, O., & Shapiro, D. (2015). Efficacy of obeticholic acid in patients with primary biliary cirrhosis and inadequate response to ursodeoxycholic acid. *Gastroenterology*, *148*(4), 751-761.e8. https://doi.org/10.1053/j.gastro.2014.12.005

Huang, C., & Freter, C. (2015). Lipid metabolism, apoptosis and cancer therapy. *International Journal of Molecular Sciences*, *16*(1), 924–949. https://doi.org/10.3390/ijms16010924

Ioannou, G. N., Haigh, W. G., Thorning, D., & Savard, C. (2013). Hepatic cholesterol crystals and crown-like structures distinguish NASH from simple steatosis. *Journal of Lipid Research*, *54*(5), 1326–1334. https://doi.org/10.1194/jlr.M034876

Iorga, A., Dara, L., & Kaplowitz, N. (2017). Molecular Sciences Drug-Induced Liver Injury: Cascade of Events Leading to Cell Death, Apoptosis or Necrosis. *International Journal of Molecular Sciences*, *18*(1018). https://doi.org/10.3390/ijms18051018

Itoh, M., Kato, H., Suganami, T., Konuma, K., Marumoto, Y., Terai, S., Sakugawa, H., Kanai, S., Hamaguchi, M., Fukaishi, T., Aoe, S., Akiyoshi, K., Komohara, Y., Takeya, M., Sakaida, I., & Ogawa, Y. (2013). Hepatic crown-like structure: A unique histological feature in non-alcoholic steatohepatitis in mice and humans. *PLoS ONE*, *8*(12). https://doi.org/10.1371/journal.pone.0082163

Itoh, M., Suganami, T., Kato, H., Kanai, S., Shirakawa, I., Sakai, T., Goto, T., Asakawa, M., Hidaka, I., Sakugawa, H., Ohnishi, K., Komohara, Y., Asano, K., Sakaida, I., Tanaka, M., & Ogawa, Y. (2017). CD11c+ resident macrophages drive hepatocyte death-triggered liver fibrosis in a murine model of nonalcoholic steatohepatitis. *JCI Insight*, *2*(22). https://doi.org/10.1172/jci.insight.92902

Jansen, P. L. M., Ghallab, A., Vartak, N., Reif, R., Schaap, F. G., Hampe, J., & Hengstler, J. G. (2017). The ascending pathophysiology of cholestatic liver disease. *Hepatology*, *65*(2), 722–738. https://doi.org/10.1002/hep.28965

Jiao, N., Baker, S. S., Chapa-Rodriguez, A., Liu, W., Nugent, C. A., Tsompana, M., Mastrandrea, L., Buck, M. J., Baker, R. D., Genco, R. J., Zhu, R., & Zhu, L. (2018). Suppressed hepatic bile acid signalling despite elevated production of primary and secondary bile acids in NAFLD. *Gut*, *67*(10), 1881–1891. https://doi.org/10.1136/gutjnl-2017-314307

Jiao, Y., Lu, Y., & Li, X. Y. (2015). Farnesoid X receptor: A master regulator of hepatic triglyceride and glucose homeostasis. *Acta Pharmacologica Sinica*, *36*(1), 44–50. https://doi.org/10.1038/aps.2014.116

Kalra, A., & Tuma, F. (2018). Physiology, Liver. In *StatPearls*. StatPearls Publishing. http://www.ncbi.nlm.nih.gov/pubmed/30571059

Kanda, T., Matsuoka, S., Yamazaki, M., Shibata, T., Nirei, K., Takahashi, H., Kaneko, T., Fujisawa, M., Higuchi, T., Nakamura, H., Matsumoto, N., Yamagami, H., Ogawa, M., Imazu, H., Kuroda, K., & Moriyama, M. (2018). Apoptosis and non-alcoholic fatty liver diseases. *World Journal of Gastroenterology*, *24*(25), 2661–2672. https://doi.org/10.3748/wjg.v24.i25.2661

Kararigas, G., Nguyen, B. T., Zelarayan, L. C., Hassenpflug, M., Toischer, K., Sanchez-Ruderisch, H., Hasenfuss, G., Bergmann, M. W., Jarry, H., & Regitz-Zagrosek, V. (2014). Genetic Background Defines the Regulation of Postnatal Cardiac Growth by 17β-Estradiol Through a β-Catenin Mechanism. *Endocrinology*, *155*(7), 2667–2676. https://doi.org/10.1210/en.2013-2180

Katz, N., Teutsch, H. F., Jungermann, K., & Sasse, D. (1977). Heterogeneous reciprocal localization of fructose-1,6-bis-phosphatase and of glucokinase in microdissected periportal and perivenous rat liver tissue. *FEBS Letters*, *83*(2), 272–276. https://doi.org/10.1016/0014-5793(77)81021-1

Kawano, Y., & Cohen, D. E. (2013). Mechanisms of hepatic triglyceride accumulation in non-alcoholic fatty liver disease. *Journal of Gastroenterology*, *48*(4), 434–441. https://doi.org/10.1007/s00535-013-0758-5

Kietzmann, T. (2017). Metabolic zonation of the liver: The oxygen gradient revisited. *Redox Biology*, *11*, 622–630. https://doi.org/10.1016/j.redox.2017.01.012

Kiriyama, Y., & Nochi, H. (2019). The biosynthesis, signaling, and neurological functions of bile acids. *Biomolecules*, *9*(6). https://doi.org/10.3390/biom9060232

Kleiner, D. E., & Makhlouf, H. R. (2016). Histology of Nonalcoholic Fatty Liver Disease and Nonalcoholic Steatohepatitis in Adults and Children. *Clinics in Liver Disease*, *20*(2), 293–312. https://doi.org/10.1016/j.cld.2015.10.011

Knebel, B., Haas, J., Hartwig, S., Jacob, S., & Kö Llmer, C. (2012). Liver-Specific Expression of Transcriptionally Active SREBP-1c Is Associated with Fatty Liver and Increased Visceral Fat Mass. *PLoS ONE*, *7*(2), 31812. https://doi.org/10.1371/journal.pone.0031812

Kong, B., Wang, L., Chiang, J. Y. L., Zhang, Y., Klaassen, C. D., & Guo, G. L. (2012). Mechanism of tissue-specific farnesoid X receptor in suppressing the expression of genes in bile-acid synthesis in mice. *Hepatology*, *56*(3), 1034–1043. https://doi.org/10.1002/hep.25740

Kordes, C., & Häussinger, D. (2013). Hepatic stem cell niches. *Journal of Clinical Investigation*, *123*(5), 1874–1880. https://doi.org/10.1172/JCI66027

Kruger, N. J. (2009). The Bradford Method For Protein Quantitation. In *The Protein Protocols Handbook* (pp. 17–24). Humana Press, Totowa, NJ. https://doi.org/10.1007/978-1-59745-198-7_4

Krumschnabel, G., Ebner, H. L., Hess, M. W., & Villunger, A. (2010). Apoptosis and necroptosis are induced in rainbow trout cell lines exposed to cadmium. *Aquatic Toxicology*, *99*(1), 73–85. https://doi.org/10.1016/j.aquatox.2010.04.005

Lin, H.-P., Singla, B., Ghoshal, P., Faulkner, J. L., Cherian-Shaw, M., O, P. M., She, J.-X., Belin de Chantemele, E. J., & Csányi, G. (2018). Identification of novel macropinocytosis inhibitors using a rational screen of Food and Drug Administration-approved drugs. *British Journal of Pharmacology*, *175*, 3640–3655. https://doi.org/10.1111/bph.14429

Liu, Z., & Roche, P. A. (2015). Macropinocytosis in phagocytes: Regulation of MHC class-II-restricted antigen presentation in dendritic cells. *Frontiers in Physiology*, *6*(JAN). https://doi.org/10.3389/fphys.2015.00001

Livak, K. J., & Schmittgen, T. D. (2001). Analysis of relative gene expression data using real-time quantitative PCR and the 2-ΔΔCT method. *Methods*, *25*(4), 402–408. https://doi.org/10.1006/meth.2001.1262

Lopez Amador, N., Hipolito, C. N., Rojas Jimeno, M. de J., & Zarrabal, O. C. (2017). Liver enzymes in patients diagnosed with non-alcoholic fatty liver disease (NAFLD) in Veracruz: a comparative analysis with the literature. *Clinical Investigation*, *07*(01), 11–016.

https://doi.org/10.4172/clinical-investigation.1000107

Luedde, T., Kaplowitz, N., & Schwabe, R. F. (2014). Cell death and cell death responses in liver disease: Mechanisms and clinical relevance. *Gastroenterology*, *147*(4), 765-783.e4. https://doi.org/10.1053/j.gastro.2014.07.018

Malhi, H., & Gores, G. J. (2008). Cellular and Molecular Mechanisms of Liver Injury. *Gastroenterology*, *134*(6), 1641–1654. https://doi.org/10.1053/j.gastro.2008.03.002

Malik, R., Selden, C., & Hodgson, H. (2002). The role of non-parenchymal cells in liver growth. *Seminars in Cell and Developmental Biology*, *13*(6), 425–431. https://doi.org/10.1016/S1084952102001301

Manghisi, G., Elba, S., Mossa, A., Giorgio, A., Aloisio, V., Perrotta, A., Tardio, B., Del Naja, C., Caturelli, E., Calandra, M., Castellano, L., De Sio, I., Capuano, G., Pomponi, D., Castiglione, F., Cocchia, P., Farinati, F., Rinaldi, M., Adinolfi, L. E., … Pignata, S. (1998). A new prognostic system for hepatocellular carcinoma: A retrospective study of 435 patients. *Hepatology*, *28*(3), 751–755. https://doi.org/10.1002/hep.510280322

Manne, V., & Kowdley, K. V. (2019). Obeticholic acid in primary biliary cholangitis: where we stand. *Current Opinion in Gastroenterology*, *35*(3), 191–196. https://doi.org/10.1097/MOG.0000000000000525

Martinez-Hernandez, A. (1984). The hepatic extracellular matrix. I. Electron immunohistochemical studies in normal rat liver. *Laboratory Investigation*, *51*(1), 57–74.

Masyuk, A. I., Masyuk, T. V., & LaRusso, N. F. (2012). Physiology of Cholangiocytes. In *Physiology of the Gastrointestinal Tract* (Vol. 2, pp. 1531–1557). Elsevier Inc. https://doi.org/10.1016/B978-0-12-382026-6.00056-7

McGlone, E. R., & Bloom, S. R. (2019). Bile acids and the metabolic syndrome. *Annals of Clinical Biochemistry*, *56*(3), 326–337. https://doi.org/10.1177/0004563218817798

Meier, P. J., & Stieger, B. (2002). Bile salt transporters. *Annual Review of Physiology*. https://doi.org/10.1146/annurev.physiol.64.082201.100300

Mitra, S., De, A., & Chowdhury, A. (2020). Epidemiology of non-alcoholic and alcoholic fatty liver diseases. *Translational Gastroenterology and Hepatology*, *5*. https://doi.org/10.21037/TGH.2019.09.08

Miyake, M., Ragnarsson, E., Nakai, D., & Artursson, P. (2016). The Pro-inflammatory Cytokine Interleukin-6 Regulates Nanoparticle Transport Across Model Follicle-Associated Epithelium Cells. *Journal of Pharmaceutical Sciences*, *105*(7), 2099–2104. https://doi.org/10.1016/j.xphs.2016.03.043

Mudaliar, S., Henry, R. R., Sanyal, A. J., Morrow, L., Marschall, H. U., Kipnes, M., Adorini, L., Sciacca, C. I., Clopton, P., Castelloe, E., Dillon, P., Pruzanski, M., & Shapiro, D. (2013). Efficacy and safety of the farnesoid x receptor agonist Obeticholic acid in patients with type 2 diabetes and nonalcoholic fatty liver disease. *Gastroenterology*, *145*(3), 574-582.e1. https://doi.org/10.1053/j.gastro.2013.05.042

Muzumdar, M. D., Tasic, B., Miyamichi, K., Li, L., & Luo, L. (2007). A global double-fluorescent Cre reporter mouse. *Genesis*, *45*(9), 593–605. https://doi.org/10.1002/dvg.20335

Neekhra, N., & Padh, H. (2004). An insight into molecular mechanism of endocytosis. *Indian Journal of Biochemistry & Biophysics*, 69–80. https://pubmed.ncbi.nlm.nih.gov/22900333/

Neumann, K., Rudolph, C., Neumann, C., Janke, M., Amsen, D., & Scheffold, A. (2015). Liver sinusoidal endothelial cells induce immunosuppressive IL-10-producing Th1 cells via the Notch pathway. *European Journal of Immunology*, *45*(7), 2008–2016. https://doi.org/10.1002/eji.201445346

Neuschwander-Tetri, B. A., Loomba, R., Sanyal, A. J., Lavine, J. E., Van Natta, M. L., Abdelmalek, M. F., Chalasani, N., Dasarathy, S., Diehl, A. M., Hameed, B., Kowdley, K. V., McCullough, A., Terrault, N., Clark, J. M., Tonascia, J., Brunt, E. M., Kleiner, D. E., & Doo, E. (2015). Farnesoid X nuclear receptor ligand obeticholic acid for non-cirrhotic, non-alcoholic steatohepatitis (FLINT): A multicentre, randomised, placebo-controlled trial. *The Lancet*, *385*(9972), 956–965. https://doi.org/10.1016/S0140-6736(14)61933-4

Nevens, F., Andreone, P., Mazzella, G., Strasser, S. I., Bowlus, C., Invernizzi, P., Drenth, J. P. H., Pockros, P. J., Regula, J., Beuers, U., Trauner, M., Jones, D. E., Floreani, A., Hohenester, S., Luketic, V., Shiffman, M., van Erpecum, K. J., Vargas, V., Vincent, C., … Shapiro, D. (2016). A Placebo-Controlled Trial of Obeticholic Acid in Primary Biliary Cholangitis. *New England Journal of Medicine*, *375*(7), 631–643. https://doi.org/10.1056/nejmoa1509840

Nguyen, P., Leray, V., Diez, M., Serisier, S., Le Bloc'H, J., Siliart, B., & Dumon, H. (2008). Liver lipid metabolism. *Journal of Animal Physiology and Animal Nutrition*, *92*(3), 272–283. https://doi.org/10.1111/j.1439-0396.2007.00752.x

Nobili, V., Alisi, A., Newton, K. P., & Schwimmer, J. B. (2016). Comparison of the Phenotype and Approach to Pediatric vs Adult Patients With Nonalcoholic Fatty Liver Disease. *Gastroenterology*, *150*, 1798–1810. https://doi.org/10.1053/j.gastro.2016.03.009

Olaso, E., Ikeda, K., Eng, F. J., Xu, L., Wang, L.-H., Lin, H. C., & Friedman, S. L. (2001). DDR2 receptor promotes MMP-2–mediated proliferation and invasion by hepatic stellate cells. *Journal of Clinical Investigation*, *108*(9), 1369–1378. https://doi.org/10.1172/jci12373

Ortega-Ribera, M., Yeste, J., Villa, R., & Gracia-Sancho, J. (2018). Nanoengineered biomaterials for the treatment of liver diseases. In *Nanoengineered Biomaterials for Regenerative Medicine* (pp. 417–441). Elsevier. https://doi.org/10.1016/B978-0-12-813355-2.00018-1

Pandak, W. M., & Kakiyama, G. (2019). The acidic pathway of bile acid synthesis: Not just an alternative pathway. *Liver Research*, *3*(2), 88–98. https://doi.org/10.1016/j.livres.2019.05.001

Parker, G. A., & Picut, C. A. (2012). Immune Functioning in Non lymphoid Organs: The Liver. *Toxicologic Pathology*, *40*(2), 237–247. https://doi.org/10.1177/0192623311428475

Perry, R. J., Samuel, V. T., Petersen, K. F., & Shulman, G. I. (2014). The role of hepatic lipids in hepatic insulin resistance and type 2 diabetes. *Nature*, *510*(7503), 84–91. https://doi.org/10.1038/nature13478

Perumpail, B., Li, A., John, N., Sallam, S., Shah, N., Kwong, W., Cholankeril, G., Kim, D., & Ahmed, A. (2018). The Role of Vitamin E in the Treatment of NAFLD. *Diseases*, *6*(4), 86. https://doi.org/10.3390/diseases6040086

Petrasek, J., Csak, T., & Szabo, G. (2013). Toll-Like Receptors in Liver Disease. In *Advances in Clinical Chemistry* (Vol. 59, pp. 155–201). Academic Press Inc. https://doi.org/10.1016/B978-0-12-405211-6.00006-1

Potter, B. J. (2019). Components of the Hepatic System. In *Reference Module in Biomedical Sciences*. Elsevier. https://doi.org/10.1016/b978-0-12-801238-3.04935-7

Poupon, R. (2015). Liver alkaline phosphatase: A missing link between choleresis and biliary inflammation. *Hepatology*, *61*(6), 2080–2090. https://doi.org/10.1002/hep.27715

Promrat, K., Kleiner, D. E., Niemeier, H. M., Jackvony, E., Kearns, M., Wands, J. R., Fava, J. L., & Wing, R. R. (2010). Randomized controlled trial testing the effects of weight loss on nonalcoholic steatohepatitis. *Hepatology*, *51*(1), 121–129. https://doi.org/10.1002/hep.23276

Pydyn, N., Miękus, K., Jura, J., & Kotlinowski, J. (2020). New therapeutic strategies in nonalcoholic fatty liver disease: a focus on promising drugs for nonalcoholic steatohepatitis. *Pharmacological Reports*, *72*(1), 1–12. https://doi.org/10.1007/s43440-019-00020-1

Ramachandran, P., Pellicoro, A., Vernon, M. A., Boulter, L., Aucott, R. L., Ali, A., Hartland, S. N., Snowdon, V. K., Cappon, A., Gordon-Walker, T. T., Williams, M. J., Dunbar, D. R., Manning, J. R., Van Rooijen, N., Fallowfield, J. A., Forbes, S. J., & Iredale, J. P. (2012). Differential Ly-6C expression identifies the recruited macrophage phenotype, which orchestrates the regression of murine liver fibrosis. *Proceedings of the National Academy of Sciences of the United States of America*, *109*(46), E3186–E3195. https://doi.org/10.1073/pnas.1119964109

Rappaport, A. M., Borowy, Z. J., Lougheed, W. M., & Lotto, W. N. (1954). Subdivision of hexagonal liver lobules into a structural and functional unit. Role in hepatic physiology and pathology. *The Anatomical Record*, *119*(1), 11–33. https://doi.org/10.1002/ar.1091190103

Ratziu, V., Sanyal, A. J., Loomba, R., Rinella, M., Harrison, S., Anstee, Q. M., Goodman, Z., Bedossa, P., MacConell, L., Shringarpure, R., Shah, A., & Younossi, Z. (2019). REGENERATE: Design of a pivotal, randomised, phase 3 study evaluating the safety and efficacy of obeticholic acid in patients with fibrosis due to nonalcoholic steatohepatitis. *Contemporary Clinical Trials*, *84*, 105803. https://doi.org/10.1016/j.cct.2019.06.017

Reif, R., Ghallab, A., Beattie, L., Günther, G., Kuepfer, L., Kaye, P. M., & Hengstler, J. G. (2017). In vivo imaging of systemic transport and elimination of xenobiotics and endogenous molecules in mice. *Archives of Toxicology*, *91*(3), 1335–1352. https://doi.org/10.1007/s00204-016-1906-5

Richardson, M. M., Jonsson, J. R., Powell, E. E., Brunt, E. M., Neuschwander-Tetri, B. A., Bhathal, P. S., Dixon, J. B., Weltman, M. D., Tilg, H., Moschen, A. R., Purdie, D. M., Demetris, A. J., & Clouston, A. D. (2007). Progressive Fibrosis in Nonalcoholic Steatohepatitis: Association With Altered Regeneration and a Ductular Reaction. *Gastroenterology*, *133*(1), 80–90. https://doi.org/10.1053/j.gastro.2007.05.012

Ridlon, J. M., Kang, D. J., & Hylemon, P. B. (2006). Bile salt biotransformations by human intestinal bacteria. *Journal of Lipid Research*, *47*(2), 241–259. https://doi.org/10.1194/jlr.R500013-JLR200

Rinella, M. E., Tacke, F., Sanyal, A. J., & Anstee, Q. M. (2019). Report on the AASLD/EASL Joint Workshop on Clinical Trial Endpoints in NAFLD. *Hepatology*, *70*(4), 1424–1436. https://doi.org/10.1002/hep.30782

Rock, K. L., & Kono, H. (2008). The inflammatory response to cell death. *Annual Review of*

Pathology: Mechanisms of Disease, *3*, 99–126. https://doi.org/10.1146/annurev.pathmechdis.3.121806.151456

Rosenbaum, D. M., Degterev, A., David, J., Rosenbaum, P. S., Roth, S., Grotta, J. C., Cuny, G. D., Yuan, J., & Savitz, S. I. (2009). Necroptosis, a novel form of caspase-independent cell death, contributes to neuronal damage in a retinal ischemia-reperfusion injury model. *Journal of Neuroscience Research*, *88*(7), NA-NA. https://doi.org/10.1002/jnr.22314

Roychowdhury, S., Chiang, D. J., Mandal, P., McMullen, M. R., Liu, X., Cohen, J. I., Pollard, J., Feldstein, A. E., & Nagy, L. E. (2012). Inhibition of Apoptosis Protects Mice from Ethanol-Mediated Acceleration of Early Markers of CCl4-Induced Fibrosis but not Steatosis or Inflammation. *Alcoholism: Clinical and Experimental Research*, *36*(7), 1139–1147. https://doi.org/10.1111/j.1530-0277.2011.01720.x

Russell, D. W. (2003). The enzymes, regulation, and genetics of bile acid synthesis. *Annual Review of Biochemistry*, *72*, 137–174. https://doi.org/10.1146/annurev.biochem.72.121801.161712

Sarveazad, A., Agah, S., Babahajian, A., Amini, N., & Bahardoust, M. (2019). Predictors of 5 year survival rate in hepatocellular carcinoma patients. *Journal of Research in Medical Sciences*, *24*(1). https://doi.org/10.4103/jrms.JRMS_1017_18

Sato, K., Kennedy, L., Liangpunsakul, S., Kusumanchi, P., Yang, Z., Meng, F., Glaser, S., Francis, H., & Alpini, G. (2019). Intercellular Communication between Hepatic Cells in Liver Diseases. *International Journal of Molecular Sciences*, *20*(9), 2180. https://doi.org/10.3390/ijms20092180

Schlaeger, R., Haux, P., & Kattermann, R. (1982). Studies on the mechanism of the increase in serum alkaline phosphatase activity in cholestasis: Significance of the hepatic bile acid concentration for the leakage of alkaline phosphatase from rat liver. *Enzyme*, *28*(1), 3–13. https://doi.org/10.1159/000459078

Schoemaker, M. H., Conde De La Rosa, L., Buist-Homan, M., Vrenken, T. E., Havinga, R., Poelstra, K., Haisma, H. J., Jansen, P. L. M., & Moshage, H. (2004). Tauroursodeoxycholic acid protects rat hepatocytes from bile acid-induced apoptosis via activation of survival pathways. *Hepatology*, *39*(6), 1563–1573. https://doi.org/10.1002/hep.20246

Schuppan, D., Surabattula, R., & Wang, X. Y. (2018). Determinants of fibrosis progression and regression in NASH. *Journal of Hepatology*, *68*(2), 238–250. https://doi.org/10.1016/j.jhep.2017.11.012

Schwabe, R. F., Wiley, J. W., Marra, F., & Tacke, F. (2014). REVIEWS IN BASIC AND CLINICAL GASTROENTEROLOGY AND HEPATOLOGY Roles for Chemokines in Liver Disease. *Gastroenterology*, *147*, 577-594.e1. https://doi.org/10.1053/j.gastro.2014.06.043

Schwen, L. O., Homeyer, A., Schwier, M., Dahmen, U., Dirsch, O., Schenk, A., Kuepfer, L., Preusser, T., & Schenk, A. (2016). Zonated Quantification of Steatosis in an Entire Mouse Liver. *Computers in Biology and Medicine*, *73*, 108–118. https://doi.org/10.1016/j.compbiomed.2016.04.004

Sezgin, S., Hassan, R., Zühlke, S., Kuepfer, L., Hengstler, J. G., Spiteller, M., & Ghallab, A. (2018). Spatio-temporal visualization of the distribution of acetaminophen as well as its metabolites and adducts in mouse livers by MALDI MSI. *Archives of Toxicology*, *92*(9), 2963–2977. https://doi.org/10.1007/s00204-018-2271-3

Sheka, A. C., Adeyi, O., Thompson, J., Hameed, B., Crawford, P. A., & Ikramuddin, S. (2020). Nonalcoholic Steatohepatitis: A Review. *JAMA - Journal of the American Medical Association*, *323*(12), 1175–1183. https://doi.org/10.1001/jama.2020.2298

Sinal, C. J., Tohkin, M., Miyata, M., Ward, J. M., Lambert, G., & Gonzalez, F. J. (2000). Targeted disruption of the nuclear receptor FXR/BAR impairs bile acid and lipid homeostasis. *Cell*, *102*(6), 731–744. https://doi.org/10.1016/S0092-8674(00)00062-3

Sookoian, S., & Pirola, C. J. (2015). Liver enzymes, metabolomics and genome-wide association studies: From systems biology to the personalized medicine. *World Journal of Gastroenterology*, *21*(3), 711–725. https://doi.org/10.3748/wjg.v21.i3.711

Staels, B., & Fonseca, V. A. (2009). Bile acids and metabolic regulation: mechanisms and clinical responses to bile acid sequestration. *Diabetes Care*, *32 Suppl 2*(Suppl 2), S237. https://doi.org/10.2337/dc09-s355

Stanger, B. Z. (2015). The Annual Review of Physiology is online at. *Annu. Rev. Physiol*, *77*, 179–200. https://doi.org/10.1146/annurev-physiol-021113-170255

Swanson, J. A. (2008). Shaping cups into phagosomes and macropinosomes. *Nature Reviews Molecular Cell Biology*, *9*(8), 639–649. https://doi.org/10.1038/nrm2447

Swanson, J. A., & Watts, C. (1995). Macropinocytosis. *Trends in Cell Biology*, *5*(11), 424–428. https://doi.org/10.1016/S0962-8924(00)89101-1

Swiderska-Syn, M., Suzuki, A., Guy, C. D., Schwimmer, J. B., Abdelmalek, M. F., Lavine, J. E., & Diehl, A. M. (2013). Hedgehog pathway and pediatric nonalcoholic fatty liver disease. *Hepatology*, *57*(5), 1814–1825. https://doi.org/10.1002/hep.26230

Szabo, G., Mandrekar, P., & Dolganiuc, A. (2007). Innate Immune Response and Hepatic Inflammation. *Seminars in Liver Disease*, *27*(4), 339–350. https://doi.org/10.1055/s-2007-991511

Tacke, F., & Trautwein, C. (2015). Mechanisms of liver fibrosis resolution. *Journal of Hepatology*, *63*, 1038–1039. https://doi.org/10.1016/j.jhep.2015.03.039

Tosello-Trampont, A. C., Landes, S. G., Nguyen, V., Novobrantseva, T. I., & Hahn, Y. S. (2012). Kuppfer cells trigger nonalcoholic steatohepatitis development in diet-induced mouse model through tumor necrosis factor-α production. *Journal of Biological Chemistry*, *287*(48), 40161–40172. https://doi.org/10.1074/jbc.M112.417014

Treyer, A., & Müsch, A. (2013). Hepatocyte polarity. *Comprehensive Physiology*, *3*(1), 243–287. https://doi.org/10.1002/cphy.c120009

Tsochatzis, E. A., Bosch, J., & Burroughs, A. K. (2014). Liver cirrhosis. *The Lancet*, *383*(9930), 1749–1761. https://doi.org/10.1016/S0140-6736(14)60121-5

Twisk, J., Hoekman, M. F. M., Mager, W. H., Moorman, A. F. M., De Boer, P. A. J., Scheja, L., Princen, H. M. G., & Gebhardt, R. (1995). Heterogeneous expression of cholesterol 7α-hydroxylase and sterol 27- hydroxylase genes in the rat liver lobulus. *Journal of Clinical Investigation*, *95*(3), 1235–1243. https://doi.org/10.1172/JCI117773

Van Waes, L., & Lieber, C. S. (1977). Glutamate dehydrogenase: a reliable marker of liver cell necrosis in the alcoholic. *British Medical Journal*, *2*, 1508–1510.

Vernon, H., & Kasi, A. (2019). Anatomy, Abdomen and Pelvis, Liver. In *StatPearls*. StatPearls

Publishing. http://www.ncbi.nlm.nih.gov/pubmed/29763190

Vilar-Gomez, E., Martinez-Perez, Y., Calzadilla-Bertot, L., Torres-Gonzalez, A., Gra-Oramas, B., Gonzalez-Fabian, L., Friedman, S. L., Diago, M., & Romero-Gomez, M. (2015). Weight loss through lifestyle modification significantly reduces features of nonalcoholic steatohepatitis. *Gastroenterology*, *149*(2), 367-378.e5. https://doi.org/10.1053/j.gastro.2015.04.005

Vucur, M., Reisinger, F., Gautheron, J., Janssen, J., Roderburg, C., Cardenas, D. V., Kreggenwinkel, K., Koppe, C., Hammerich, L., Hakem, R., Unger, K., Weber, A., Gassler, N., Luedde, M., Frey, N., Neumann, U. P., Tacke, F., Trautwein, C., Heikenwalder, M., & Luedde, T. (2013). RIP3 inhibits inflammatory hepatocarcinogenesis but promotes cholestasis by controlling caspase-8- and JNK-dependent compensatory cell proliferation. *Cell Reports*, *4*(4), 776–790. https://doi.org/10.1016/j.celrep.2013.07.035

Wang, H., Peters, T., Sindrilaru, A., & Scharffetter-Kochanek, K. (2009). Key role of macrophages in the pathogenesis of CD18 hypomorphic murine model of psoriasis. *Journal of Investigative Dermatology*, *129*(5), 1100–1114. https://doi.org/10.1038/jid.2009.43

Wójciak-Stothard, B., Entwistle, A., Garg, R., & Ridley, A. J. (1998). Regulation of TNF-α-induced reorganization of the actin cytoskeleton and cell-cell junctions by Rho, Rac, and Cdc42 in human endothelial cells. *Journal of Cellular Physiology*, *176*(1), 150–165. https://doi.org/10.1002/(SICI)1097-4652(199807)176:1<150::AID-JCP17>3.0.CO;2-B

Wong, V. W. S., Wong, G. L. H., Choi, P. C. L., Chan, A. W. H., Li, M. K. P., Chan, H. Y., Chim, A. M. L., Yu, J., Sung, J. J. Y., & Chan, H. L. Y. (2010). Disease progression of non-alcoholic fatty liver disease: A prospective study with paired liver biopsies at 3 years. *Gut*, *59*(7), 969–974. https://doi.org/10.1136/gut.2009.205088

Xu, J. Y., Li, Z. P., Zhang, L., & Ji, G. (2014). Recent insights into farnesoid X receptor in non-alcoholic fatty liver disease. *World Journal of Gastroenterology*, *20*(37), 13493–13500. https://doi.org/10.3748/wjg.v20.i37.13493

Younossi, Z. M., Koenig, A. B., Abdelatif, D., Fazel, Y., Henry, L., & Wymer, M. (2016). Global epidemiology of nonalcoholic fatty liver disease—Meta-analytic assessment of prevalence, incidence, and outcomes. *Hepatology*, *64*(1), 73–84. https://doi.org/10.1002/hep.28431

Zhuang, Z., Qu, H., Yang, W., Liu, J., Wang, F., Liu, Y., Ding, J., & Shi, J. (2020). Comparing hepatic steatosis distribution patterns between non-alcoholic fatty liver disease and fatty liver disease with chronic hepatitis B by second-harmonic generation/two-photon excited fluorescence method. *Annals of Hepatology*, *19*(3), 313–319. https://doi.org/10.1016/j.aohep.2019.11.003

Zollner, G., Wagner, M., Fickert, P., Silbert, D., Gumhold, J., Zatloukal, K., Denk, H., & Trauner, M. (2007). Expression of bile acid synthesis and detoxification enzymes and the alternative bile acid efflux pump MRP4 in patients with primary biliary cirrhosis. *Liver International*, *27*(7), 920–929. https://doi.org/10.1111/j.1478-3231.2007.01506.x

ACKNOWLEDGEMENTS

Completion of my PhD degree would not have been possible without the support of several important people in my life.

First, I want to thank **Prof. Dr. med. Jan G. Hengstler** for providing me an opportunity to do my PhD at IfADo. I am grateful for your supervision and your guidance in every possible situation.

My most sincere gratitude goes to my co-supervisor **Dr. Ahmed Ghallab**. First of all, thank you for adopting me into your junior group and saving my PhD. As if that was not already enough, you have definitely challenged me but also provided me the support I needed to do my best throughout these years. Thank you from the bottom of my heart for always being there when I needed help or advice, no matter how small or stupid my problem was.

I want to thank the whole junior group for being always supportive and extremely helpful: Thank you **Dr. Reham Hassan, Lisa Brackhagen,** and special thanks to **Zaynab Hobloss,** whose technical support was brilliant and more than I could have ever asked for. In addition, thank you for being not only a great colleague but also a great friend during these years.

I am grateful for all the technical support I have got. Thank you **Brigitte Begher-Tibbe** for all your shared knowledge and help especially with MALDI-MSI and 3D reconstructions. Thank you **Elmar Kriek** for taking good care of the mice and for all the early morning talks to make my day start a bit better. Moreover, I want to thank **Dr. Ute Hofmann** from IKP Stuttgart for the bile acid analysis, **Dr. Michael Trauner** from Medical University of Vienna for providing the human samples, **Dr. Fabian Geisler** and **Dr. Simon Jörs** from Technical University of Munich for bile fragment analysis, and **Dr. Mihael Vucur** from Uniklinik RWTH Aachen for cell death pathway analysis. I also want to thank **Monika Turajski** for all the help with German bureaucracy.

Who would have thought when I moved to Germany alone and scared that I am going to find the best possible people around me. **Katharina Belgasmi**, **Daniela González and Sarah Metzler**, you fast switched from colleagues to my German family and I cannot ever tell you how much that means to me. Thank you for all the moments when the laugh just does not end, and thank you also for all the tears I could share with you. You have been there for me in good times and in bad as an endless support system but also mocked me enough to make me stay in touch with reality. Furthermore, I want to thank another IfADo gem **Adelina Jashari** for being a great friend and sharing the good experiences and frustrations both at work and outside of it. Lastly, this journey would have been very different without the LivTox guys **David Feuerborn** and **Patrick Nell.**

Although things have not always gone so smoothly, I got a lot of great memories and never had a boring day with you.

Getting to know and work with my IfADo colleagues has been truly a privilege. Thank you Dr. Rosemarie Marchan, Dr. Cristina Cadenas, Dr. Karolina Edlund, Dr. Wolfram Föllmann, Wiebke Albrecht, Philipp Gabrys, Annika Glotzbach, Georgia Günther, Gregor Leonhardt, Adrian Rieck, and many others.

My PhD would have never happened without my family. You have provided me everything I ever needed, especially your continuous love, support and faith in me in the moments when I did not believe in myself. Thank you for always letting me choose my own path, even if it means a physical distance between us. Kiitos kaikesta, rakkaat.

My Finnish friends, thank you for proving that distance means nothing. I appreciate every single message, phone call, post card, and package you have remembered me with. Thank you for reminding me about the life outside my German bubble and making me laugh in a daily basis.

Last but definitely not least, thank you Hans for getting me out for walks during the long working days and especially for protecting the office from intruders, no matter what.